IDENTIFICATION AND DISCRIMINATION OF BACTERIA IN A NOBLE GAS ENVIRONMENT USING LASER-INDUCED BREAKDOWN SPECTROSCOPY (LIBS)

by

NARMATHA JEYASINGHAM

THESIS

Submitted to the Graduate School

of Wayne State University,

Detroit, Michigan

in partial fulfillment of the requirements

for the degree of

MASTER OF SCIENCE

2007

MAJOR: PHYSICS

Approved by:

_____

Advisor Date

_____

_____

_____

Table of Contents

List of Figures

List of Tables

Chapter 1

Introduction

1.1 Bacteria physiology

Biological and bacteriological threats have become subjects of intensified study from September 11, 2001 in the United States. Biological hazards comprise primarily bacteria, viruses, biotoxins, fungi and low concentrations of whatever can create large-scale contamination. Bacteria are unicellular microorganisms, typically a few micrometers long and have many shapes including rods (bacillus), spheres (coccus), and spirals (spirillum).[1] Although the vast majority of bacteria are rendered harmless or beneficial by the protective effects of the immune system, a few pathogenic bacteria cause infectious diseases, including cholera, syphilis, anthrax and plague. On the other hand, in industry, bacteria are important in processes such as waste water treatment, the production of cheese and yoghurt, and the manufacture of antibiotics and other chemicals. [2]

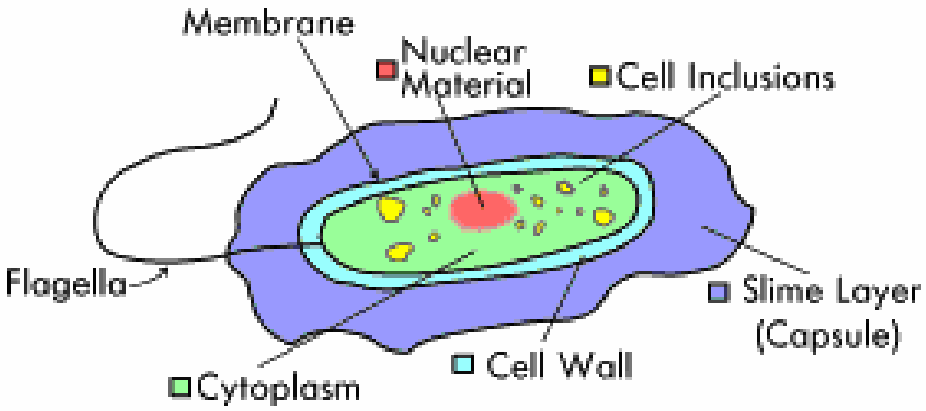

Figure 1.1 The generic cell structure of bacteria. Adapted from www.alken murray.com/ CELLANA.gif

Bacteria are prokaryotes. Unlike animals and other eukaryotes, bacterial cells do not contain a nucleus or other membrane-bound organelles.[1] The generic cell structure of a bacteria is shown in Figure 1.1. In general, bacteria can be divided into two major groups, called Gram-positive and Gram-negative. The original distinction between Gram-positive and Gram-negative was based on a special staining procedure, the Gram stain, but differences in cell wall structure are at the base of these differences in the Gram staining reaction.[3]

Table 1.1 Comparision of Gram-positive and Gram-negative cell walls

Characteristics	**Gram-positive**	**Gram-negative**
Number of major layers	1	2
Chemical composition	Peptidoglycan Teichoic acid Lipoteichoic acid	Lipopolysaccharide Lipoprotein Peptidoglycan
Overall thickness	Thicker (20-80 nm)	Thinner (8-11 nm)
Outer membrane	No	Yes
Porin proteins	No	Yes
Permeability	More penetrable	Less penetrable

The Gram-negative cell wall is multilayered structure and quite complex, whereas the Gram-positive cell wall consists of primarily a single type of molecule and is often much thicker.[6] All of the work described in this thesis were performed with Gram-negative bacteria. Unlike most types of cells, Gram-negative surround themselves with a double membrane.[4] The cell wall component common to all eubacteria is the peptidoglycan, which contributes mechanical rigidity. The additional outer membrane layer in Gram-negative bacteria is made out of lipopolysaccharide (LPS), which contains

polysaccharide and protein. [1,4,6] A schematic of the outer membrane of a Gram negative bacteria is shown in Figure 1.2.

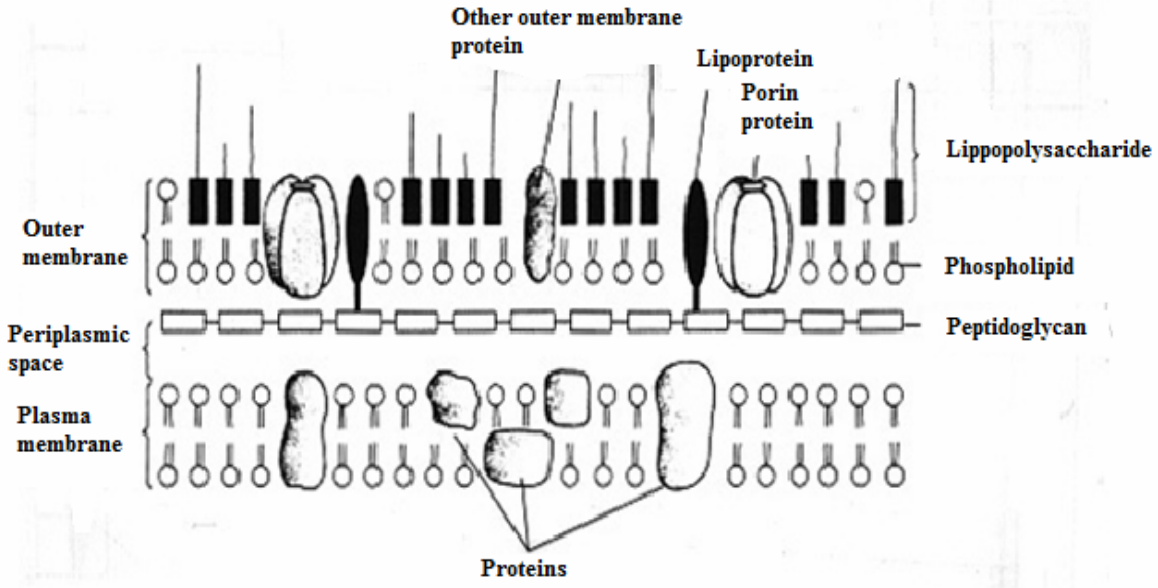

Figure 1.2 The schematic drawing of the outer membrane of the Gram-negative bacterium. Adopted from http://textbookofbacteriology.net/BSRP.html

The polysaccharide consists of two portions, the core polysaccharide and O-polysaccharide. The core polysaccharide consists of ketodeoxyoctonate (KDO), seven-carbon sugars (heptose), glucose, galactose and N-acetylglucosamine.[1] Connected to the core is O-polysaccharide, which usually contains galactose, glucose and six-carbon sugars (mannose). The lipid portion of LPS is called Lipid A.[1,6] A schematic of the LPS layer is shown in Figure 1.3.

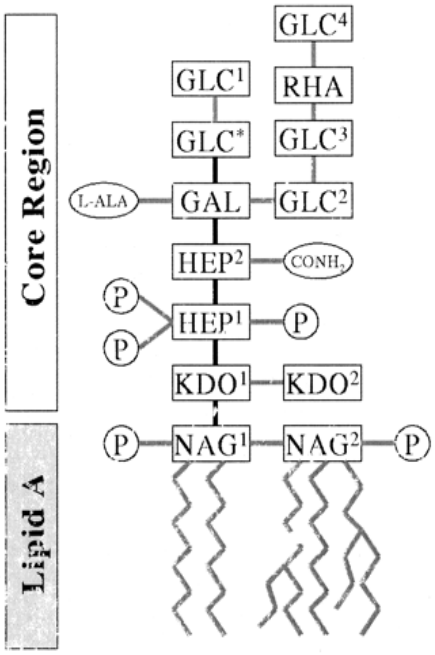

Figure 1.3 A schematic of the LPS structure. Adapted from http://www.biophysj.org/content/vol81/issue2/images/large/bj0815039001.jpeg

In the outer membrane, the LPS is associated with various proteins. A lipoprotein complex is found on the inner side of the outer membrane. This lipoprotein is a small protein that functions as an anchor between the outer membrane and peptidoglycan.[1] Porins function as channel for the entrance and exit of hydrophilic low-molecular-weight substances.[6] LPS was also found to bind divalent cations quite strongly. Divalent cations are atoms with two additional electrons when compared to their elemental state. The specific cation and the location of cation binding have an intense influence on the physical structure of LPS aggregates. It has been found that the LPS layer contains inorganic elements such as calcium, magnesium, potassium, carbon and sodium (in the form of divalent cations) in the KDO core region and P in phosphate groups.[5,7,8] Figure 1.4 shows a computer simulation (from Reference 5) of the LPS molecule with divalent Ca^{2+} bound in the KDO region.

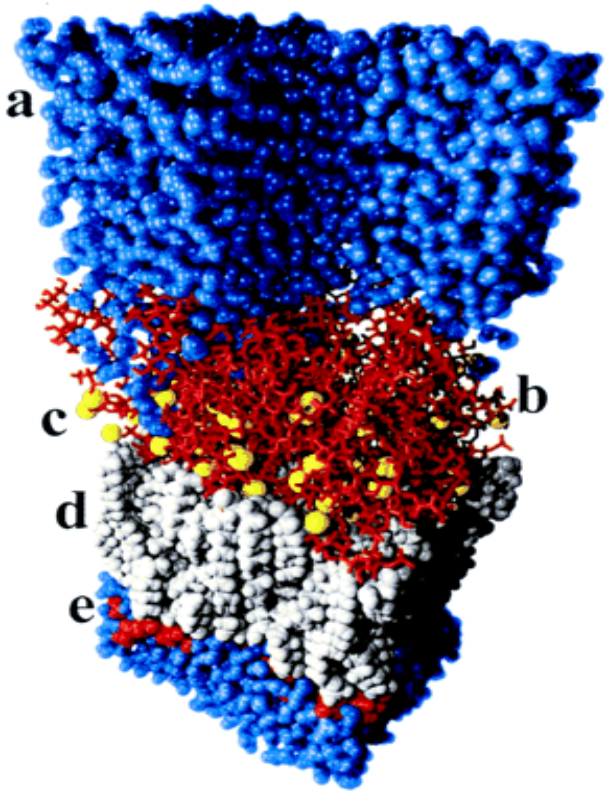

Figure 1.4 Molecular model of the rough LPS membrane of *Pseudomonas aeruginosa*, showing (a) the water layer of which a cross-section cut was made to display (b) the top of the sugars (c) the yellow spheres represent Ca^{2+} ions (d) the phospholipid layer (e) polar head groups immersed in water

The outer membrane makes the bacteria resistant to host defense factors such as lysozyme, commonly referred to as the "body's own antibiotic" since it kills bacteria and leukocyte proteins. Also the outer membrane develops a very effective barrier, giving protection to cells from the detergent action of bile salts and degradation by digestive enzymes. [4]

At the same time the outer membrane acts as a strong permeability barrier to many antibiotics that are effective against other bacteria.[6] Even though the diffusion of antibiotics is slowed down by the outer membrane, the bacteria can inactivate the amount of antibiotics present in the medium. As a result, a very strong resistance is established in

Gram-negative bacteria. Another important function of the outer membrane is to provide the bacterial surface with strong hydrophilicity, which is important in the capacity to avoid a specific immune attack by altering the surface antigen formation.[6]

1.2 Bacteria identification

The methods that microbiologists use to identify bacteria to the level of genus and species fall into the main categories of morphology, biochemistry, serological analysis and genetic techniques. The useful and most common procedure, the Gram stain, separates bacteria into two classifications according to the composition of their cell walls. The method is named after its inventor, Hans Christian Gram (1853-1938). His technique consisted of timed, sequential applications of crystal violet (the primary dye), Gram's Iodine (the mordant), an alcohol rinse (decolorizer) and a contrasting counter stain, safranin. Table 1.2 explains the procedure of Gram staining in brief.

In the first step, crystal violet is attracted to the cells, in a smear and stains them all the same purple color. The second and key differentiating step is the addition of the mordant, Gram's Iodine. The mordant is a stabilizer that causes the dye to form large crystals in the peptidoglycan of the cell wall. Because the peptidoglycan layer in Gram-positive cells is thicker, the entrapment of the dye is far more extensive in them than in Gram-negative cells. Application of alcohol in the third step dissolves lipids in the outer membrane and removes the dye from the peptidolycan layer and the Gram-negative cells. By contrast, the crystals of dye tightly embedded in the peptidoglycan of Gram-positive bacteria are relatively inaccessible and resistant to removal. Because Gram-negative bacteria are colorless after decolorization, their presence is demonstrated by applying the counter stain safranin in the final step. [9]

Table 1.2 Gram stain technique and theory

	Microscopic appearance of Cell	
Step	**Gram positive**	**Gram negative**
1. Crystal Violet		
	Both cell walls affix the dye	
2. Gram's Iodine		
	Dye crystals trapped in wall	No effect on Iodine
3. Alcohol		
	Crystals remain in cell wall	Cell wall partially dissolved, loses dye
4. Safranin (red dye)		
	Red dye has no effect	Red dye stains the colorless cell

Another interesting technique to identify bacteria is *serotyping*. Bacteria have surface and other molecules called antigens that are recognized by the immune system. One immune response to antigens is the production of molecules called antibodies that are designed to bind tightly to the antigens. This response is so specific that antibodies can be used as a means of identifying bacteria in specimens and cultures. For example, Vibrio cholera, which causes cholera, has 139 serotypes, based on cell antigens. This technique was discovered by the American microbiologist Rebecca Lancefield in 1933.[9]

The other techniques are known as *genotyping* and *phenotyping*. A mutant by definition differs from its parental strain in genotype, a precise description of the genes an organism has. But in addition, the observable properties of the mutant, its phenotype, may also be altered relative to the parental strain. The terms genotype and phenotype are

distinct for at least two reasons. First to distinguish the source of an observer's knowledge, i.e. one can know about genotype by observing DNA; one can know about phenotype by just observing outward appearance of an organism. The other fact is genotype and phenotype are not always directly correlated. Some genes only express a given phenotype in certain environmental conditions. Conversely, some phenotypes could be the result of multiple genotypes. The genotype is commonly mixed up with the phenotype, which describes the end result of both the genetic and the environmental factors giving the observed expression.[1]

1.3 Laser-induced breakdown spectroscopy

In the past few years, large efforts have been committed to identify a reliable, fast and standoff detection and identification technique for microbiological samples, like bacteria. A spectral-chemical technique, which is sensitive to the membrane composition, may tell a lot about the bacteria functionality, and then it becomes kind of serotyping, which is also membrane/antigen specific. Laser-induced breakdown spectroscopy (LIBS) fulfills the desired attributes listed above. LIBS is a spark spectrochemical sensor technology in which a laser beam is directed at sample surface to create a high temperature microplasma (> 10,000 K) and a detector is used to collect the spectrum of light emission and record its intensity at specific wavelengths.[10]

In 1960, the laser operation was first reported in a ruby crystal. Following this in 1963 came the development of a Q-switched laser.[10] This laser had the capability of producing high focused power densities from a single pulse of short duration sufficient to initiate breakdown and to produce an analytically useful laser plasma. This was the "birth" of the LIBS technique and in subsequent years significant milestones were made

in the development of the method. A typical LIBS set-up is shown in Figure 1.5. The necessary components are a powerful enough pulsed laser, an optic to focus the laser light, some means of collecting the light given off by the plasma, a spectrometer to disperse, or analyze the light, and a computer to record the observed spectrum.

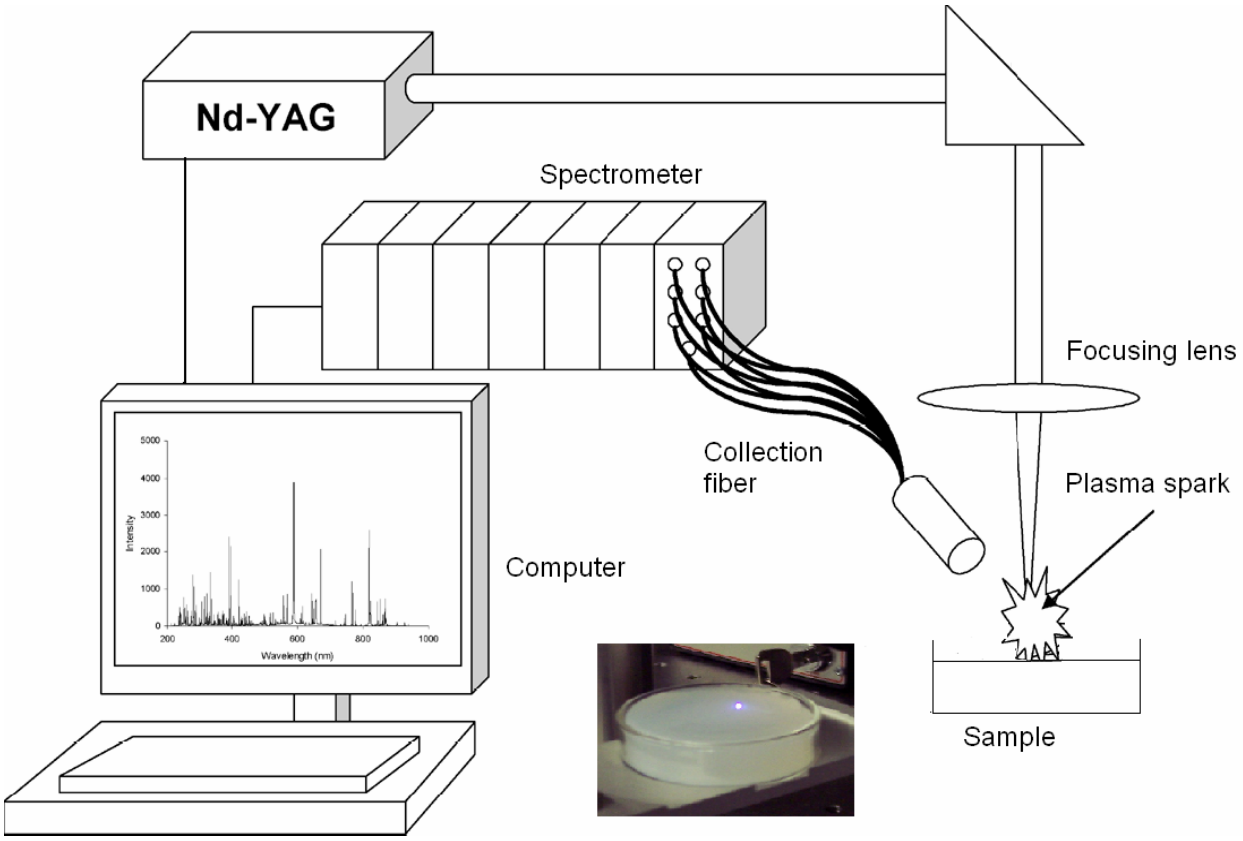

Figure 1.5 A schematic of a simple apparatus for LIBS illustrating the principle.

Since a very small amount of sample is consumed during LIBS process, the technique is considered essentially minimally destructive. Due to the nature of this technique sample preparation is often unnecessary where a specimen is known to be sufficiently homogenous, this reduces the possibility of contamination during chemical preparation steps and the sample can be solid, liquid or gas.[11] One of the major advantages of LIBS is its ability of real-time response. LIBS is an optical technique,

therefore, it requires only optical access to the specimen. This is a major significance as fiber optics may be employed for remote analysis.[10,11] These attributes in combination have importance for use in areas from hazardous environments to space exploration.

It is also subject to variation in the spark and resultant plasma, which often limits reproducibility. The accuracy of LIBS measurements is typically better than 10% and precision is often better than 5%. Limit of detection (LOD) or detection limit, is the lowest concentration level that can be determined statistically different from a blank (99% confidence). The detection limits for LIBS vary from one element to the next depending on the specimen type and the experimental apparatus used.

The vast majority of LIBS applications deal with solid samples. Typical limits of detection for the analysis of solids by LIBS are in the low-ppm range with typical uncertainty 5-10%.[12] Chaleard *et al.* quantified optical emission signals and corrected for matrix effects assuming emission lines to be a function of two parameters: the vaporized mass and the plasma excitation temperature. It was demonstrated that normalization of the net emission intensity by both the acoustic signal and the temperature allowed for a multimatrix calibration curve with about 5% precision for Cu and Mn in various alloy matrices.[13] One member of our team used LIBS as a tool for trace elemental analysis and studied it as a method of detecting small amounts of aluminum in tissues. The limit of detection of aluminum in human tissue surrogates, extrapolated from a calibration curve, was found to be less than 1 ppm.[14]

1.4 LIBS on bacteria

In only the last four years, several papers have appeared in the literature investigating the use of LIBS as a suitable technique for the detection and identification

of bio-agents. Dixon and Hahn give a very detailed outline of highlights and conclusions of the most important papers about the role of LIBS in detection and identification of individual bioaerosols.[24] It must be noted that the experimental approaches used by the very small number of groups performing these experiments is no way standardized yet at this time.

In 2003, Morel *et al.* investigated the detection of six bacteria and two pollens.[21] To test the ability of LIBS to differentiate among biological materials they prepared the samples in the form of dry pellets, guaranteeing a strong signal to noise ratio (SNR) in LIBS. They detected mineral elements such as magnesium, sodium, iron, potassium, and calcium, organic elements like carbon, nitrogen, phosphorus and hydrogen and finally CN molecular bands. They came up with a conclusion at that time that LIBS was not ideally suited for the detection of all biological samples but that it is useful as a trigger that warns the presence of bio-matter different from the normal background.

In the same year, Samuels *et al*. used a broadband spectrometer to study bacterial spores as well as other forms of biomaterials such as molds, pollens, and proteins.[22] They deposited the bio-samples as an aqueous suspension onto silver membrane filters to create thin films of deposited bio-matter. This study concluded that it was possible to discriminate between bacterial spores and the molds and pollens using LIBS. Additionally, discrimination within the three bacilli types studied appeared feasible with a more rigorous modeling approach.

In 2005, this same group extended their work by applying a simple linear correlation technique to overcome this discrimination issue.[26] They compiled a library of LIBS spectra for eight bio-materials: three bacillus spores, two pollens, two molds and a

protein. By comparing test bio-materials to the library and applying a correlation analysis, all bacillus spores were positively identified as bacterial surrogates, with no false negatives and each bacillus spore strain was correctly identified two out of three times. They expect this approach to yield even higher results by increasing the number of laser shots taken per target material and further studying the spectra to identify the key spectral components within the very large spectrum.

Boyain-Goitia *et al.* demonstrated that single laser pulse LIBS can be performed on bioaerosols such as pollens of a variety of flowers.[23] The most dominant spectral feature in the majority of spectral segments recorded in this study was the presence of carbon, normally in the form of molecular features of CN or C_2, and a few common elements in biological tissue, namely alkali and alkaline earth elements. They analyzed the same pollens, in addition to LIBS measurements, by Raman microscopy. The overall conclusions drawn from the study were that single-pulse, single bioaerosol analysis is indeed feasible but that substantial technical development work still needs to be done and that many more species need to be measured to generate a suitable reference library before detection and identification can be made reliably in real time.

Kim *et al.* used LIBS to create fingerprints of the plasma emission for the colonies of vegetative cells or spores of five bacterial strains, including *Escherichia coli*.[25] They managed to identify clearly the major inorganic components of the bacterial samples, including calcium, manganese, zinc, sodium, potassium, iron, and sulfur, but primarily focused on emissions from phosphate and atomic calcium to provide the ultimate discrimination between bio-samples. The final discrimination was achieved by

creating maps of the ratios of the two calcium lines to the ratios of two phosphate lines for each bacilli species.

Hybl *et al.* investigated the technique's potential for detecting and discriminating aerosolized bacterial spores from more common background fungal/mold spores and pollens. [27] They utilized a principal component analysis (PCP) which worked very well at discriminating between classes of biomaterials (pollens from bacilli, for example) but did observe some overlap among similar materials. These authors raised the very important point that nearly all the elemental emissions lines used to obtain a spectral fingerprint in a biological sample are also present in common dirt, and stressed the importance of further study of LIBS in a real outdoor environment.

Baudelet *et al.* used femtosecond pulse LIBS to detect and identify spectral signature of native CN bonds for bacterium.[28] They demonstrated that a kinetic study of the CN band head intensity allows an identification of the contribution of native CN molecular bonds from the biological medium. Their observation on the kinetics of an intermolecular bond as the spectral marker of a bacterial sample should be also applied to other biospecies or even to other organic materials in general.

Rehse *et al*. analyzed three strains of *Escherichia coli,* one environmental mold and on strain of *Candida albicans* by LIBS using nanosecond laser pulses on target in an air atmosphere.[38] All microorganisms were analyzed on agar substrates while still alive and with no sample preparation. They managed to identify nineteen atomic and ionic emission lines in the spectrum, which was dominated by calcium, magnesium and sodium. A discriminant function analysis was used to discriminate between the bio-types and *E. coli* strains.

A typical LIBS spectrum of *E. coli* (intensity versus wavelength) in air environment obtained by Rehse *et al.* is shown in figure 1.6. The intensities of 19 emission lines from six major elements – C, Ca, Mg, K, P and Na - were analyzed in every spectrum by non-linear least squares fitting of a Lorentzian line shape to the area under the line. The 19 areas under the spectral peaks provide a 1 x 19 array, which give the "spectral fingerprint" of the bacteria. This spectrum was obtained by averaging 10 laser pulses, each acquired 1 microsecond after the laser ablation pulse.

The same group studied *Pseudomonas aeruginosa* grown on trypticase soy agar (TSA), a blood agar plate, and a MacConkey agar plate containing bile salts by LIBS using nanosecond laser pulses in air.[39] They obtained nearly ideal spectra from *P. aeruginosa* on the TSA plate and the blood agar plate, while the bacteria grown on the MacConkey plate exhibited easily distinguishable differences from the other two. All *P.aeruginosa* samples, independent of initial growth conditions, were readily discriminated from the two *E. coli* strains.

In this thesis, I investigate the use of LIBS as a technology to differentiate bacterial species in a noble gas environment. In particular, discrimination is shown between two strains of *E. coli*: a laboratory strain HF4714 and an environmental strain Nino C, both grown in TSA, prepared in an identical manner and tested with no sample preparation other than transfer to a suitable ablation substrate in both argon and helium environment. Also I analyze the reproducibility of the experiment in both gases.

In Chapter two, I will discuss the theory behind certain phenomena used in the thesis, such as plasma breakdown, affects of atmosphere on laser vaporization, plasma temperature and possible mechanisms and the importance of parameters which controls

the experiment. In Chapter three I will discuss and describe the experimental set-up with a detail description about the instruments and the optics used.

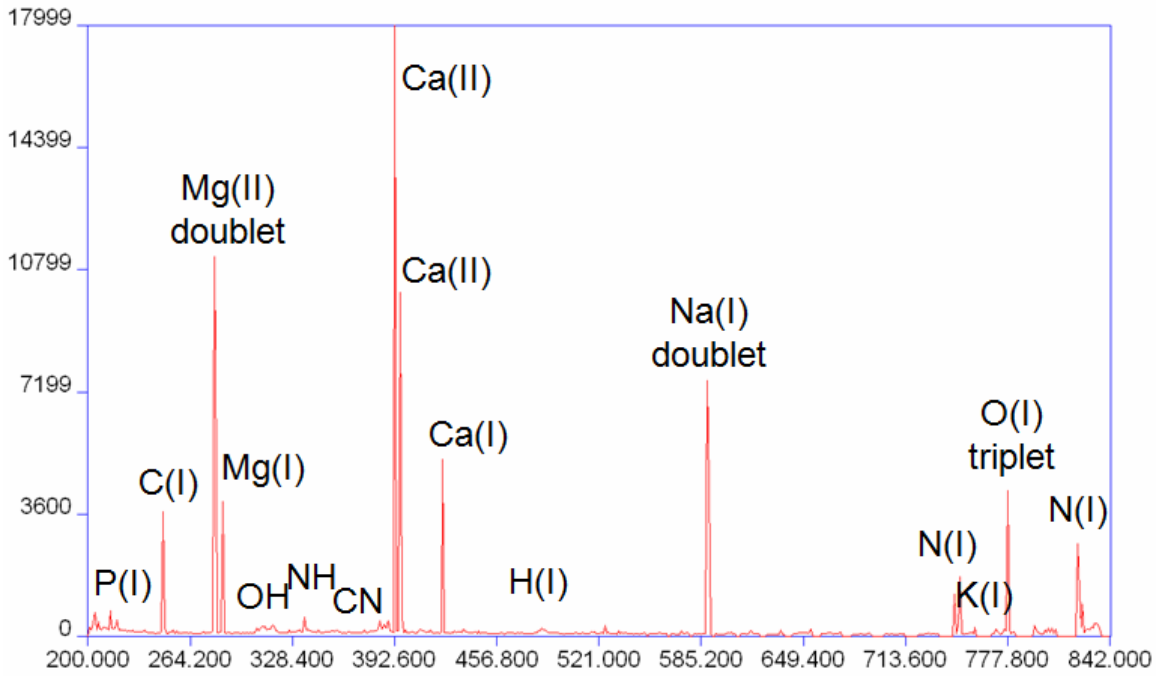

Figure 1.6 A typical LIBS spectrum of *E. coli* in air environment. The y-coordinate denotes the emission intensity and the x-coordinate gives the wavelength in nanometers. The intensities of 19 emission lines from six major elements – C, Ca, Mg, K, P and Na – are shown in the spectrum.

In Chapter four, I will discuss the importance of data analysis and the theory behind the analysis technique involved. A data analysis is very important in our experiment because the spectra obtained were subtlety different, yet highly similar, so that a casual or even a detailed inspection does not really work.

Chapter 5 will present the results. In this chapter, I will describe the way the results are obtained and give a detailed discussion about the results. I will conclude in Chapter six with a brief summary of the results and a discussion of the future avenues to be explored in this research.

Chapter 2

Theory

2.1 Plasma breakdown

The physics of laser-induced breakdown was well explained by Weyl in 1989.[10] There are two steps leading to breakdown due to optical excitation. The first one involves generating few free electrons that serve as initial receptors of energy through three body collisions with photons and neutrals. These are transient electrons liberated by cosmic rays or the local radioactivity of the earth.[10]

The second one is avalanche ionization in the focal region. Classically, free electrons are accelerated by the electric fields associated with the optical pulse in the period between collisions. As the electron energies grow, collisions produce ionization, other electrons, more energy absorption, and an avalanche occurs. For the irradiance values typically used in LIBS (10^8 - 10^{10} W/cm^2), this occurs through avalanche or cascade ionization. At higher irradiance values, significant multiphoton production of electrons can occur through:

$$M + mh\nu \rightarrow M^+ + e^- \qquad (2.1)$$

where, *m* is the number of photons, M is the atom of interest and M^+ is the corresponding ion. Multiphoton effects are necessary for direct ionization for species with greater ionization energies than energies of photon normally used. Despite the very small cross-sections for the multiphoton process, irradiances of 10^{10} W/cm^2 are sufficient for weak multiphoton ionization to occur.[11]

In the classical picture, free electrons are accelerated by the electric field in the optical pulse during the time period between collisions with neutral species. The collisions thermalize the electrons quickly. A small number of electrons in the tail of the Maxwellian distribution will have enough energy to ionize an atom or molecule through the reaction.

$$e^- + M \rightarrow 2e^- + M^+ \qquad (2.2)$$

This starts to produce other free electrons that gain energy from the field and produce more ionization. The process of electron multiplication continues during the laser pulse and results in the ionization of the gas and breakdown.

Alternatively, electrons can acquire energy from photons in the three-body collisions with atoms or molecules. This process is known as inverse Brehmsstrahlung. As the number of ions increases, the electron-photon-ion collisions increase yielding a higher probability of further electron multiplication.

$$e^-(slow) + h\nu \rightarrow e^-(fast) \qquad (2.3)$$

Following breakdown, the plasma expands outward in all directions from the focal volume. The initial rate of plasma expansion is on the order of 10^5 m/s. The loud noise that one hears is caused by the shock wave coming from the focal volume. Throughout the expansion phase the plasma emits useful emission signals. It cools and decays as its constituents give up their energies in a variety of ways. The ions and electrons recombine to form neutrals, and some of those recombine to form molecules. Energy escapes through radiation and conduction.[10,11]

In nanosecond laser pulses, electron plasma is generated by collision (avalanche) ionization. Statistical fluctuations of starting electrons for avalanche ionization lead to strong fluctuations of the damage threshold. On the other hand, optical breakdown threshold for femtosecond lasers is a well defined quantity. The breakdown threshold energy decreases with the femtosecond laser pulse duration. As a result, low ablation rates and minimal collateral damage can be achieved. Though femtosecond lasers look ideal for minimally invasive LIBS experiments with high resolution, with the experience from numerous experiments on LIBS clearly demonstrate the existence of high sensitivity of nanosecond lasers.[15]

Interestingly enough, the amount of energy in the laser pulse cannot be increased indefinitely to give brighter, hotter plasmas that contain more and more sample atoms. The problem is with plasma absorption. Once the plasma initiates, as discussed above, the absorption of laser radiation generally commences via inverse Bremsstrahlung. The absorbed energy is converted into internal energy of the plasma. With increasing irradiance, the temperature and the degree of ionization increases, which leads to additional plasma absorption. The plasma progressively behaves like an optically thick medium and effectively shields the target surface from the trailing part of the laser pulse. Most of the laser absorption occurs in a vapor layer confined close to the target surface.[33, 36]

A schematic showing various times during the development and evolution of laser-induced plasma is shown in figure 2.1. In 2.1(a), a laser pulse is incident on a bacteria target. In 2.1(b), some of the sample has been boiled or sublimated into the vapor phase. This vapor is still being irradiated by the incident laser pulse. In 2.1(c), this

expanding vapor cloud is ionized via the physical processes of electron avalanche, as described above. This step ends in the vapor "breakdown". In figure 2.1(d), some amount of time has passed since the ablation pulse, and the plasma plume has cooled. Atomic emission from the spontaneous de-excitation of atoms and ions is readily visible.

2.2 Effects of atmosphere on laser vaporization

It is well known that the laser induced plasma is time dependent and that time-resolved measurements may improve the signal-to-noise ratio of the spectra. Determining the main parameters of the plasma, such as the temperature, the electron density and the number densities of the different species present in the plasma, has acquired a high interest in recent years because it allows one to improve their applications, and also provides a better understanding of these complex and versatile spectroscopic sources. [16] The atmosphere is one of the important candidates of experimental conditions, which affects the plasma parameters severely, but the effects of the atmosphere have been discussed only in a few papers. The main effects of the atmosphere are the absorption of laser energy by the plasma, i.e. the shielding effect from the plasma, and the energy transfer from the plasma to the sample, i.e. the heating effect from the plasma. Several groups have done experiments with noble gases such as argon and helium and air as an environment.[16]

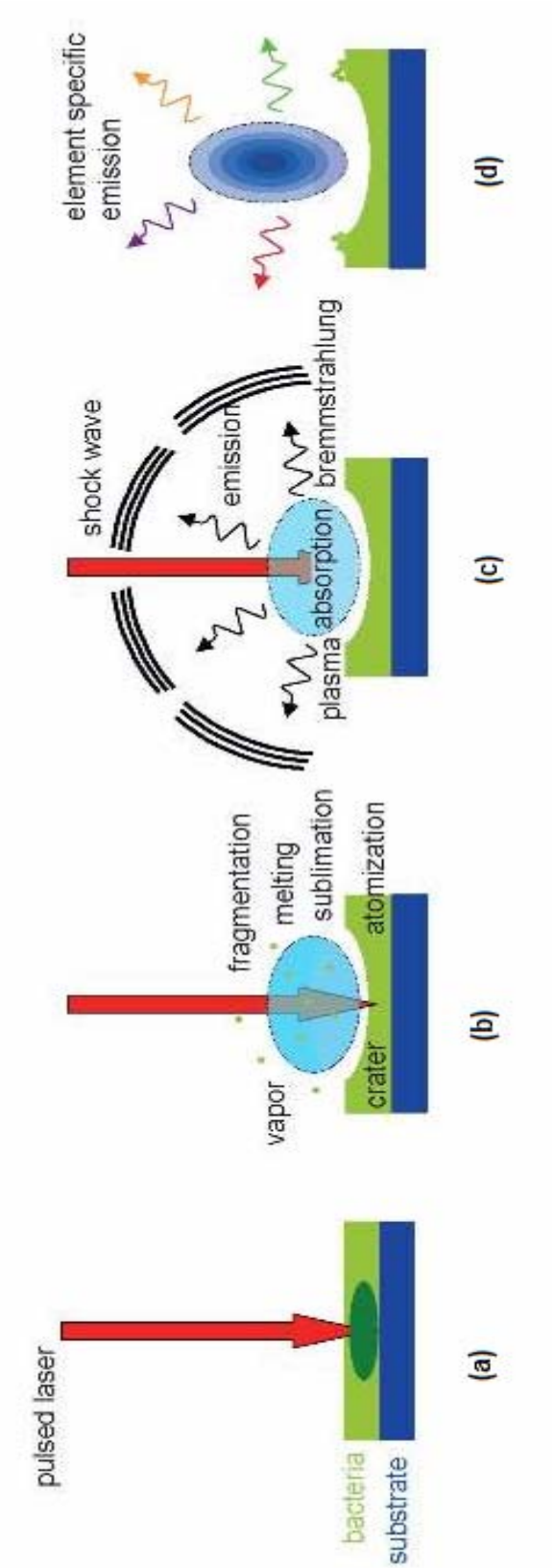

Figure 2.1 The diagram showing the main events in the LIBS process utilizing nanosecond laser pulses taken from http://www.physics.wayne.edu/~srehse/. (a) At early times the incident laser pulse irradiates a bacterial target (b) part of the sample is vaporized as the laser continues to irradiates the surface (c) laser energy absorbed by vapor plume (d) atomic emission follows some microseconds after the ablation pulse.

Sdorra and Niemax compared the effect of different ambient gases (argon, neon, helium, nitrogen, and air) in the production of plasma by means of a nanosecond Nd:YAG on a copper target. Argon was demonstrated to produce the higher plasma temperature, the higher electron density and, despite the lower mass ablation rate, the higher emission intensity for the chosen monitored element under fixed experimental conditions. Moreover, the decay rate of the temperature during the first 40 μs after the laser pulse was slower for argon than for the other gases.[18] The same behavior was found by Iida.[17] In conclusion, argon was found to be most efficiently heated by inverse Bremsstruhlung, generating a buffer plasma which optically shields the target surface, thus reducing the amount of mass ablated.

The helium gas has higher thermal conduction properties than air but yields fewer electrons than air for the same initial energy (see Table 2.1). Interestingly, the plasma generated in helium is hot but with fewer electrons than in air. This allows for weaker Bremsstralung continuous radiation from the plasma, thus improving the signal-to-noise ratio. Since a lower electron density also naturally leads to a more transparent plasma, the laser energy in the helium environment might be able to interact for a longer time with the target and with the plume of ablated matter instead of being absorbed in the buffer gas in front of the target, which would explain why the plasma in helium appears closer to the target surface than in air. [40]

Kim *et al.* observed the same signal increase and longer plasma lifetime in argon, and explained this phenomenon with the smaller conductivity (0.1387 cal/cm s deg in STP) and specific heat (0.0763 cal/g deg in STP) of argon gas with respect to the corresponding air values.[19] Such differences in thermal properties result not only in a

higher temperature plasma leading to stronger emission, but also in slower cooling of the plasma, leading to a longer emission period. Another important effect from argon environment is protection of the excited atoms from forming stable compounds such as oxides, which might reduce the LIBS emission from the analyte.

Wisbrun *et al.* found that the argon atmosphere was most favorable in terms of higher analyte emission intensity and better reproducibility. In the same work the authors observed that as the atomic mass of the ambient gas increases, the collisional translation energy transfer is less effective and the plasma life is shorter.[20]

Rehse et al. investigated the importance of atmosphere above the surface of laser-ablated pure water samples.[41] They concluded that argon produced a higher temperature and electron density in these plasmas (compared to air or dry nitrogen) but the largest effect was on the temporal evolution of the emission from the plasma, particularly from hydrogen atoms and recombining molecular species.

Table 2.1 Physical properties of gases

	He	Ar	O_2
Atomic (molecular) weight	4.00	39.95	32.00
Ionization energy (eV)	24.587	15.759	12.063
C_p (cal mol^{-1} $K^{-1)}$	4.96	4.95	7.01
Ratio of specific heats	1.67	1.67	1.40
Density (g/liter)	0.1785	1.784	1.429
Thermal conductivity (10^{-6} cal s^{-1} deg^{-1} cm^{-1})	360.36	42.57	63.64

2.3 Plasma temperature and possible mechanisms

Plasma descriptions start by trying to characterize properties of the assembly of atoms, molecules, electrons and ions rather than the individual species. If thermodynamic equilibrium exits, then plasma properties, such as the relative populations of energy levels, and the distribution of the speed of the particles, can be described through the concept of temperature. In fact, thermodynamic equilibrium is rarely complete, so physicists have settled for a useful approximation, local thermodynamic equilibrium (LTE).[11] All one demands is that equilibration occurs in small regions of space, although it may be somewhat different from region to region. A useful approximation usually exists after a sufficient number of collisions have occurred to thermalize the plasma, which mean to spread the energy in the plasma across volume and species. Even then, not all species may be in thermodynamic equilibrium. It is common for heavy species and light species to equilibrate separately more quickly, and later in time with each other. The fundamental physical reason is that energy between collision partners is shared more equally the closer the masses of the colliding particle. Note that there may be more than one 'temperature'.

The spectral line radiant intensity for any atomic transition observed in the plasma is determined by the temperature of the plasma, and is given by:

$$I = h\nu gAN / 4\pi = (hcN_0 gA / 4\pi\lambda Z)\exp(-E / kT) \qquad (2.4)$$

Where, I is in units of W/sr, gA is the product of the statistical weight and Einstein A coefficient, N may be the absolute number or the number density, Z is the partition function (which usually takes the statistical weight of the ground state), ν is the line

frequency, and *E* is the energy of the upper state for the transition.[11]Note that the ratio of the intensities of two lines is given by:

$$I'/I = (\lambda g' A'/\lambda' gA)\exp[-(E'-E)/kT] \qquad (2.5)$$

thus by choosing lines for which the *g*, *A* and *E* values and wavelength are known, and measuring the relative intensities, one can simply calculate *T* by this "two-line (2.6) ". If the lines have significantly different line widths, then integrated intensities are the measurements of choice. Relative intensities are not easy to measure precisely. A way to improve temperature values is to use many lines simultaneously and perform a graphical analysis. We rearrange equation (2.4) into the form:

$$\ln(4\pi Z/hcN_0) = \ln(I\lambda/gA) = -E/kT$$

$$\ln(I\lambda/gA) = -E/kT - \ln(4\pi Z/hcN_0) \qquad (2.7)$$

This is the equation of a straight line with slope of -1/kT. Hence if one plots the quantity on the left against E, and if there is a Boltzmann distribution, a straight line is obtained. Some of the crucial factors in obtaining a good Boltzmann plot are accurate line intensities, accurate transition probabilities and well spaced upper levels.[11] The most important factor is having a sufficient number of lines of a given species all origination in different upper energy levels. With the rather limited number of lines observed in LIBS plasmas of bacteria, this is usually problematic for us, and precludes accurate temperature measurements of the plasma.

2.4 Controlled parameters

There are two important parameters involved in time-resolved detection. First, the gate delay or delay time, τ_d, the time between the plasma and formation and the start of the observation of the plasma light and the second, the gate width, τ_w, the time period over which the light is recorded.

Because the laser plasma is a pulsed source, the LIBS spectrum evolves rapidly in time. Figure 2.2 describes the sequence of the laser induced plasma. At the earliest time, the plasma light is dominated by a "white light" continuum, which has little intensity variation as a function of wavelength. This light is caused by bremsstrahlung and recombination radiation from the plasma as free electrons and ions recombine in the coupling plasma. If the plasma light is integrated over the entire emission time of the plasma, this continuum light can seriously interfere with the detection of weaker emissions from minor and trace elements in the plasma. For this reason, LIBS measurements are usually carried out using time-resolved detection. In this way the strong white light at early times can be removed from the measurements by turning the detector on after this white light has significant impact on the intensity but atomic emissions are still present.

Having discussed the physics involved in the creation of laser-induced plasma, we will now turn our attention to how the plasma was experimentally created in the lab in Chapter 3.

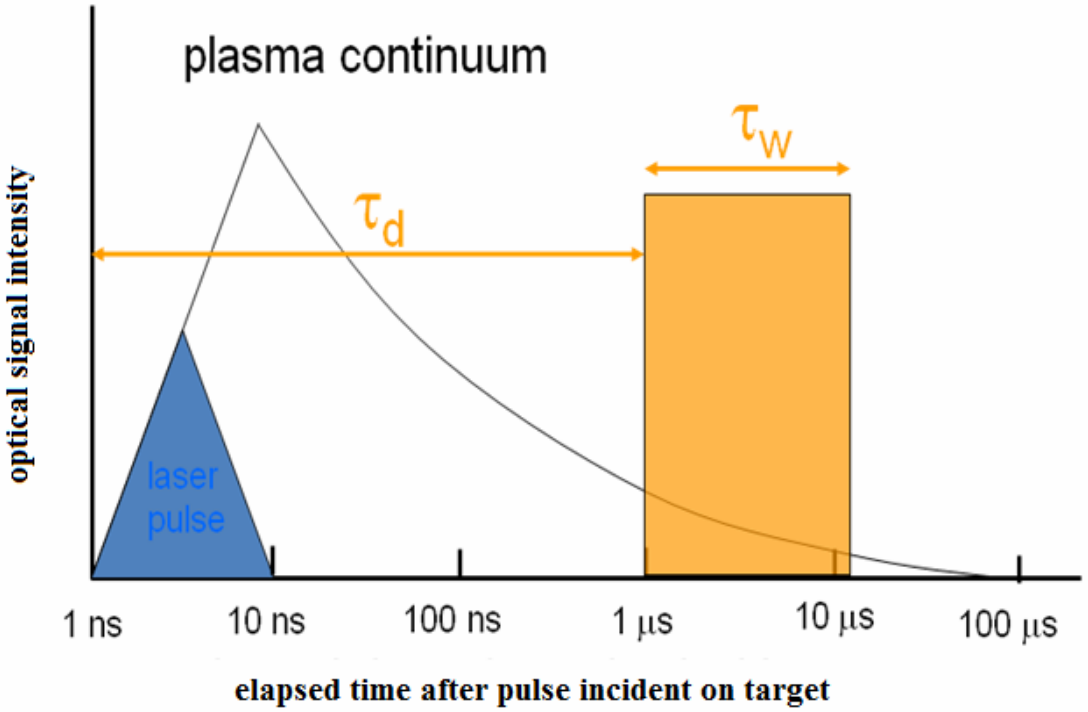

Figure 2.2 A schematic overview of the temporal history of LIBS plasma. The delay and window are shown.

Chapter 3

Experimental Set-up

3.1 Laser

A typical LIBS apparatus contains six main components: a pulsed laser which generates the powerful optical pulses used to form the microplasma, a collection of mirrors and lens, which directs and focuses the laser pulse on the target sample, a target holder or container, a light collection system, for example optical fiber cable, to collect the spark light and transport it to the detection system, a spectrometer, and finally a computer and electronics to gate the detector, fire the laser, and store the spectrum.[11]

Our LIBS apparatus consists of an Nd:YAG (Neodymium doped Yttrium Aluminum Garnet) pulsed laser (Spectra-Physics LAB 150), which operates with a pulse repetition frequency of 10 Hz at a wavelength of 1064 nm for target ablation and an Echelle spectrometer (200-800 nm) for spectroscopy. A schematic of the experimental apparatus is shown in Figure 3.1. Nd:YAG lasers with flash lamps are mostly preferred for LIBS applications because they provide a reliable, compact, and easy to use source of laser light with highly focused power density. In addition, the fundamental wavelength can be easily shifted to generate pulses with fixed wavelengths ranging from the near IR to the near UV spectral regions. There are other lasers such as excimer laser and CO_2 laser, which are rarely used for LIBS measurements.[11] They are less preferred because the lasers use gas as the lasing medium, so require periodic change of gases, their beam quality is generally inferior to the Nd:YAG, and they operate only in UV region and IR region, respectively.

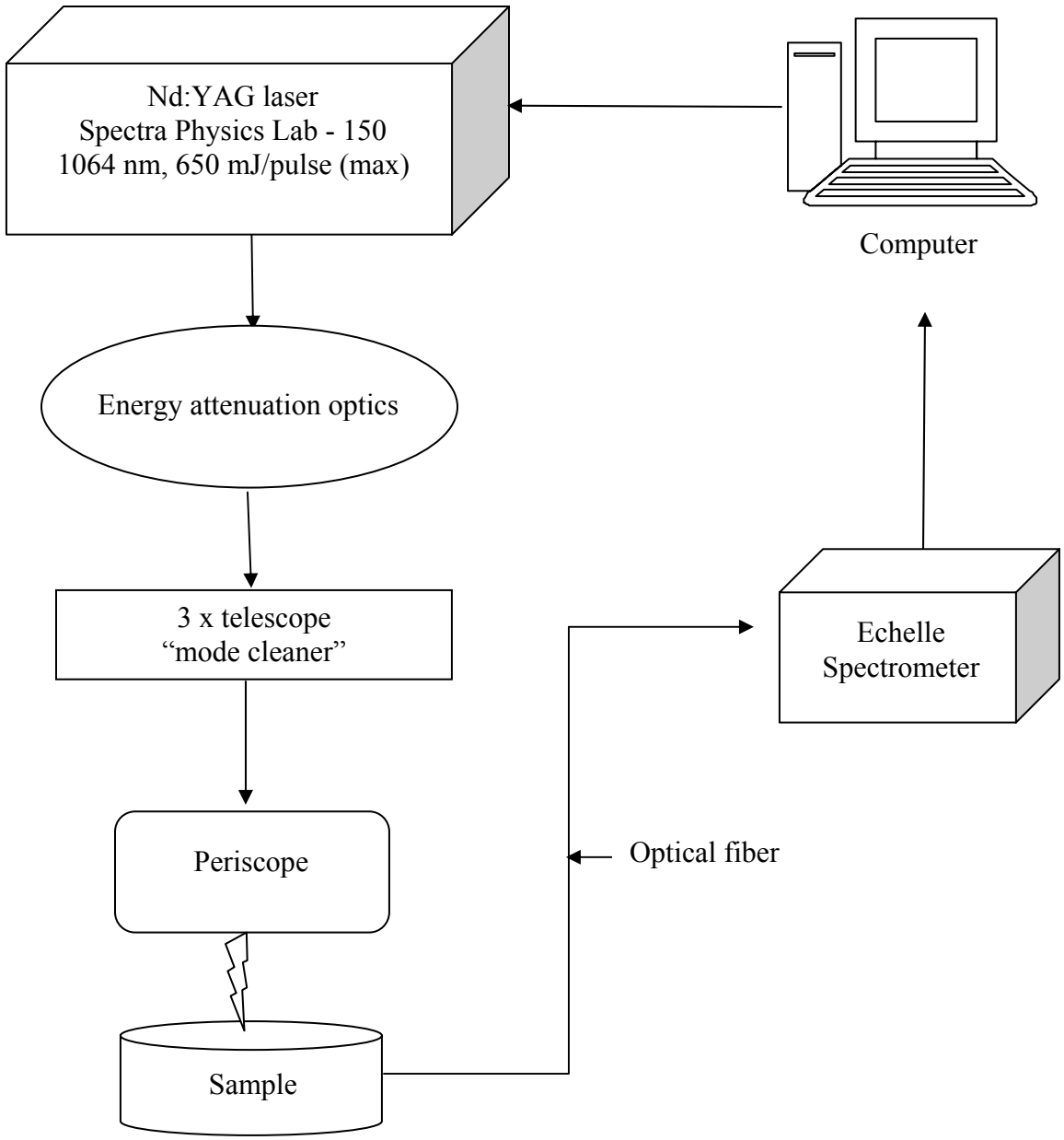

Figure 3.1 A schematic diagram of LIBS apparatus

The pulse duration of our laser is 10 ns, but in the past people have tried different pulse durations. In 2003, John D. Hybl and his team investigated the detection and identification of biological aerosols such as bacterial spores, fungi, mold spores and

pollen with 7 ns pulse duration.[27] Very recently, in 2006, Baudelet *et al*. used 5 ns to investigate *E. coli* samples.[30] These types of experiments are all referred to as "nanosecond LIBS." On the other hand, recent experiments have been carried out using femtosecond lasers. Assion *et al*, in 2003, tried 30 fs duration to demonstrate the wall-associated calcium ion (Ca^{2+}) distributions within the peripheral cell wall of the sunflower seedling stem.[15] Again the same Baudelet group, in 2006, used 120 fs pulse duration on *E. coli* and compared the spectra with the results from classical nanosecond LIBS.[29]

3.2 Laser Delivery Optics

The output pulse energy of the Nd:YAG laser is 650 mJ/pulse, when operating at its maximum. This energy was then cut down to the desired energy using a half wave plate, a polarizing beam splitter and a beam dump, as shown in figure 3.2. First, the vertically polarized beam from the laser was fed into the half wave plate. The half wave plate introduces a phase difference of π radians between perpendicular axes. Rotating a half wave plate by an angle θ relative to the polarization direction of linearly polarized light will therefore shift its polarization angle by 2θ.[31] The beam coming out from the half wave plate was then sent through the polarizing beam splitter, which transmitted only the vertical polarization through and the horizontally polarized beam was fed into the beam dump. In other words, the desired energy was acquired by changing the ratio between the vertical and horizontal polarization. The attenuated beam was then sent through a 3x telescope ("mode cleaner"), shown in figure 3.3.

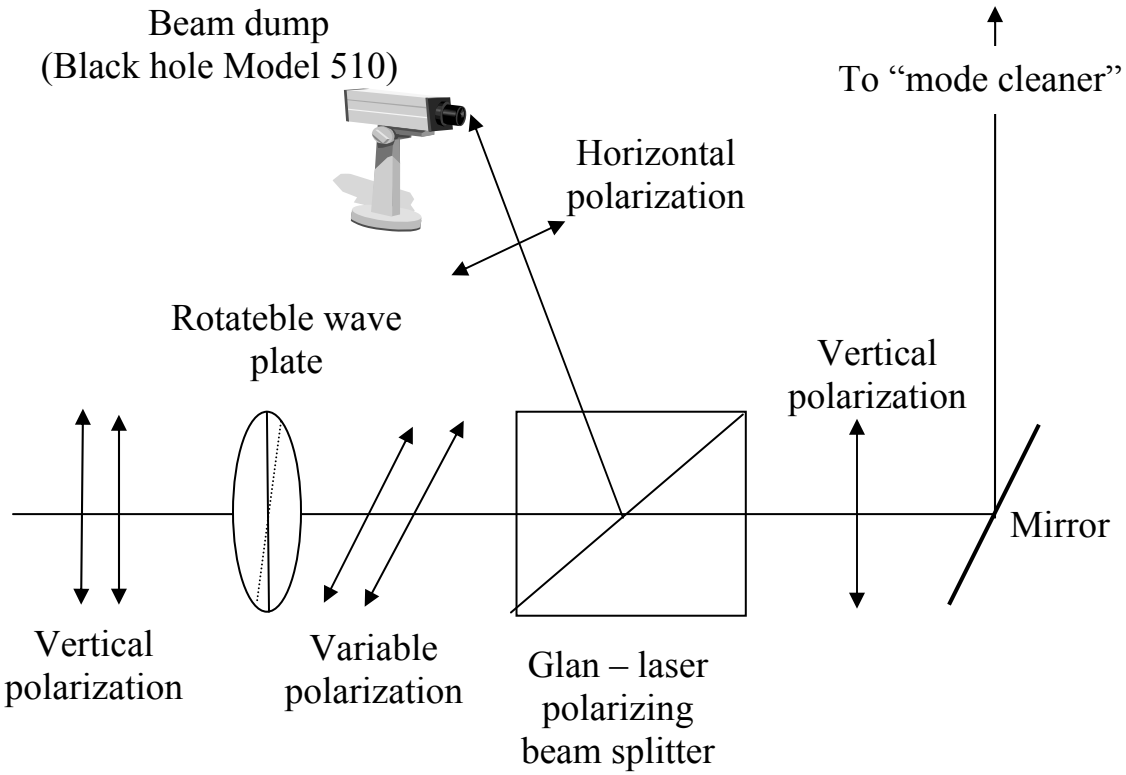

Figure 3.2 A schematic diagram of energy attenuation optics

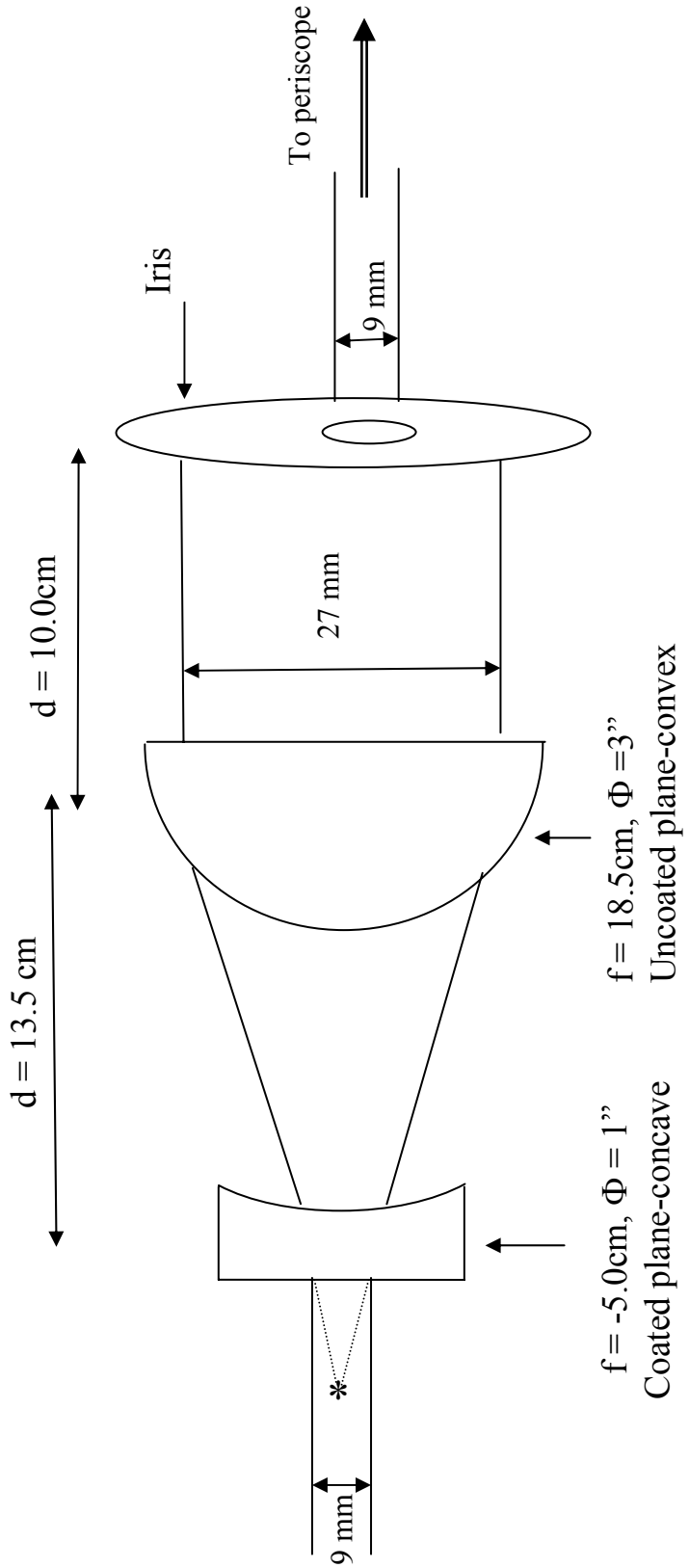

Figure 3.3 A schematic diagram of the telescope

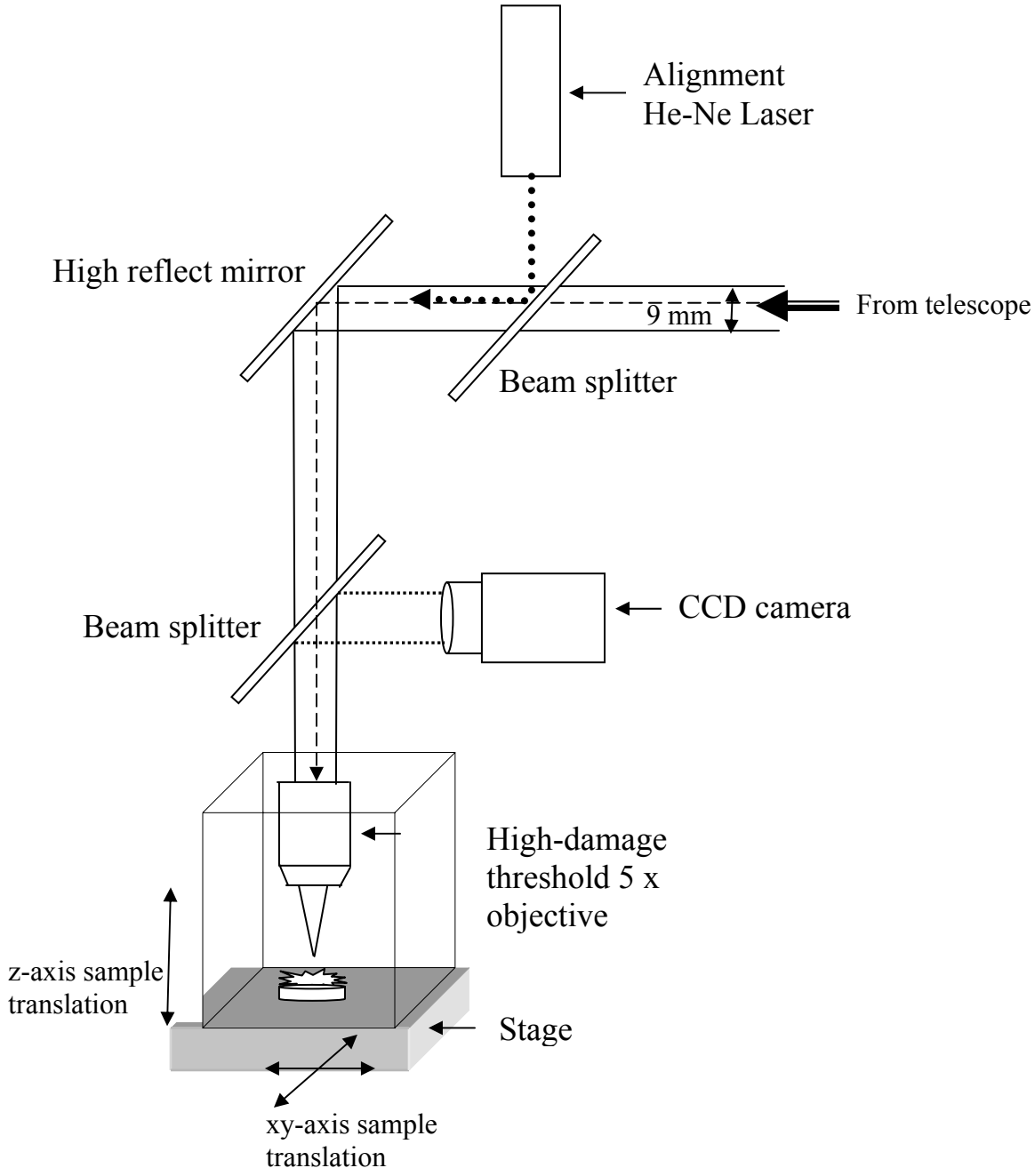

Figure 3.4 (a) The schematic side view of the periscope

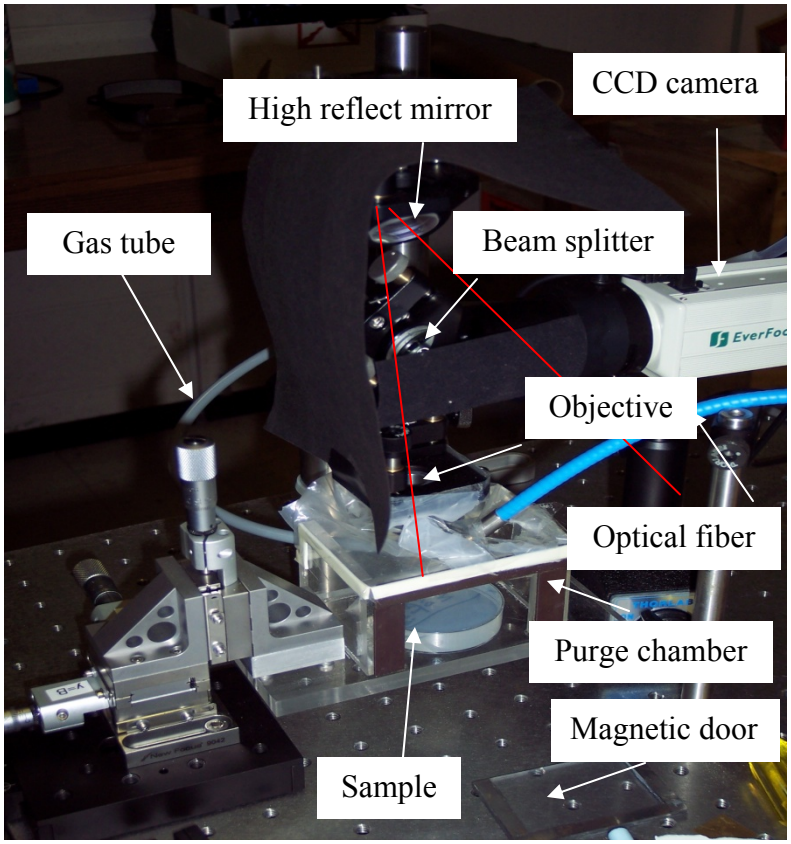

Figure 3.4 (b) The side view of the periscope

This mode cleaner was located 1.3 m after the laser and transmitted 15.4 % of the energy incident upon it. It consisted of a coated plano-concave lens (f = -5.0 cm, Φ = 1") and an uncoated plane-convex lens (f = 18.5 cm, Φ = 3") and expanded the beam from its beam diameter of 9 mm to 27 mm (Fig 3.3). An iris with a 9 mm opening immediately following the beam-expander sampled the inner one-third of the beam diameter.

A helium-neon laser at 632.8 nm was overlaid with the infra-red laser beam after the mode-cleaner in order to visualize the laser beam location after focusing in the focal plane. The collinear visible and infra-red laser beams were then reflected vertically via a periscope assembly (Fig 3.4a). After reflection, the two laser beams passed through a broadband visible wavelength beam splitter. This beam splitter was used to allow a CCD

camera (Everfocus EX 100) to image the magnified target. Both laser beams were focused by a 5x microscope objective coated with a high-damage threshold anti-reflection coating at 1064 (OFR 24-225). This objective has an aperture of 10 mm, an effective focal length of 40 mm, and the working distance of 35 mm.

3.3 Purge Chamber

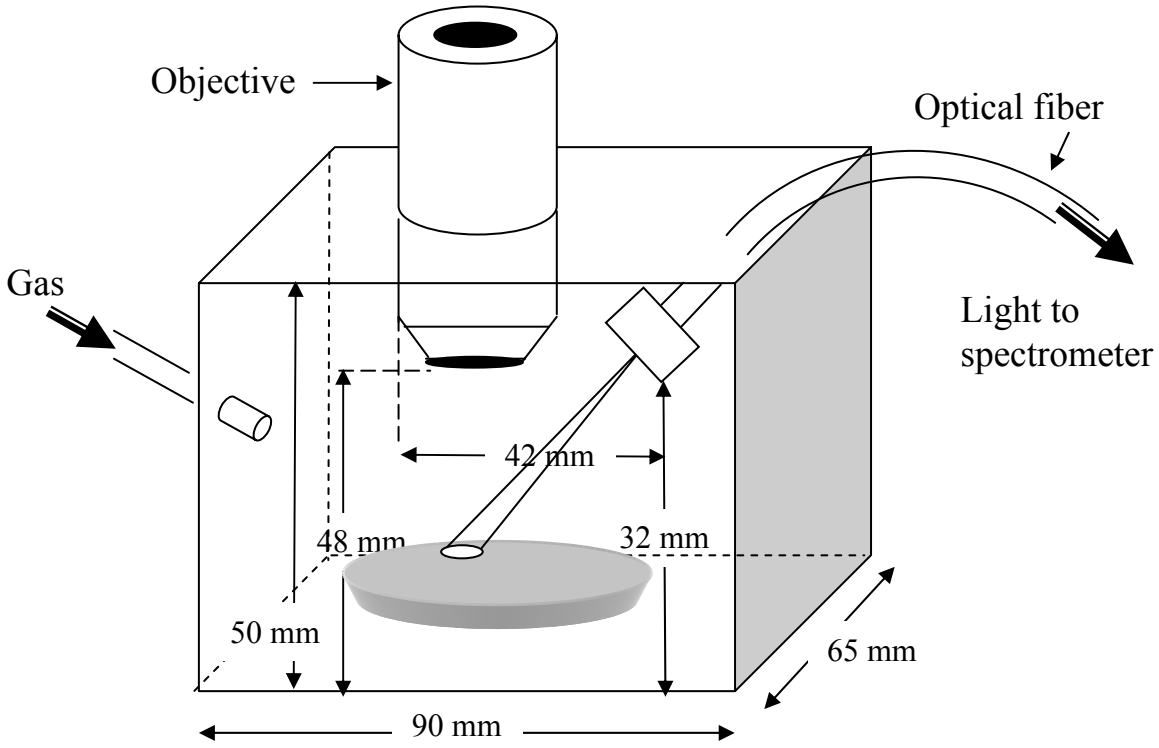

Figure 3.5 The schematic diagram of the purge chamber

A chamber with dimension 90 x 65 x 50 mm was set-up on a stage, which could be translated in x, y and z directions to place the sample, as shown in figure 3.4. The top and the back of the chamber were sealed with a polythene sheet in order to ease the movement of the objective and collecting fiber while translating the sample. The chamber was accessed through a magnetic door, which provided a tight gas seal. A tube, connected to a gas cylinder (He or Ar), was inserted through a small hole on the sheet

into the chamber and a constant flow of 10 standard cubic feet per hour (SCFH) was maintained into the chamber during the experiment.

3.4 Spectrometer

Optical emission from the microplasma was collected by an optical fiber (core diameter = 600 μm, N.A = 0.22). This fiber was angled at 30° (Fig 3.5) relative to sample normal and was aligned by illuminating the far end of exit end with a second helium-neon laser and overlapping the resulting cone of light from the fiber entrance with the alignment laser spot on the sample. This fiber was coupled to an Echelle spectrometer (ESA3000, LLA Instruments GmbH) equipped with a 1024 x 1024 intensified charges coupled device (ICCD) array, which provided a complete spectral coverage from 200 to 800 nm with a resolution of 0.005 nm in the UV.

The intensified charge coupled device (ICCD) can not only exploit gain to overcome the read noise limit but also has the added feature of being able to achieve very fast gate times, with a variable gate delay.[32] The gating and amplification occurs in the image intensifier tube. The image intensifier tube is an evacuated tube, which comprises the photocathode, micro channel pate (MCP) and a phosphor screen, and the properties of these determine the performance of the device (Fig 3.6).

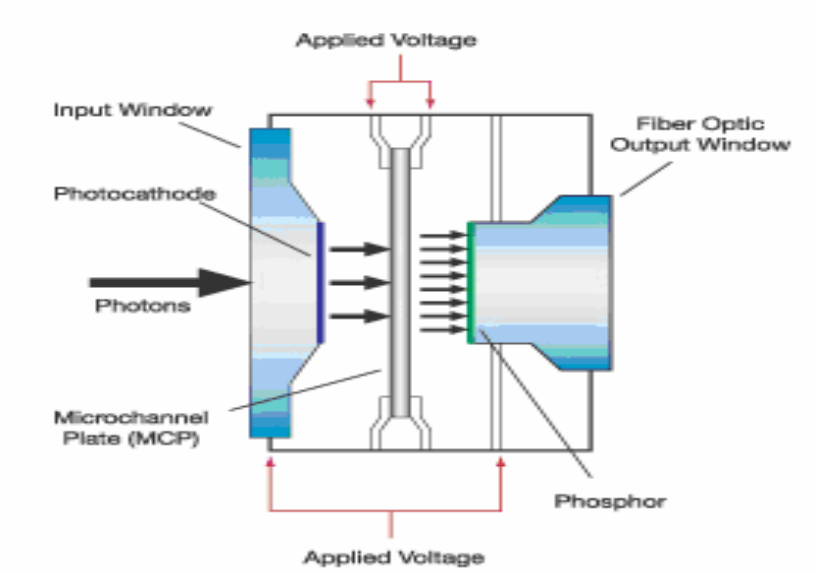

Figure 3.6 The structure of an intensified charge coupled device taken from http://www.andor.com

The photocathode is coated on the inside surface of the input window and it captures the incident image. When a photon of the image strikes the photocathode, a photoelectron is emitted, which is then drawn toward the MCP by an electric field. The MCP is a thin disc, which is a honeycomb of glass channels, each with a resistive coating. A high potential is applied across the MCP, enabling the photoelectron to accelerate down one of the channels in the disc. When the photoelectron has sufficient energy, it dislodges secondary electrons from the channel walls. These electrons in turn undergo acceleration, which results in a cloud of electrons exciting the MCP. The output of the image intensifier is coupled to the CCD typically by a fiber optic coupler.

3.5 Pulse energy

Typical pulse energy at the ablation surface was 10 mJ/pulse. Other groups have used diffeterent pulse energies on bacteria. In 2003, John D. Hybl *et al*. tried 50 mJ/pulse

to identify biological aerosols.[27] C.A. Munson *et al*., in 2003, investigated the statistics strategies for chemical and biological warfare agent with the pulse energy in the region of 30 – 120 mJ/pulse.[26] In the recent year 2006, Baudelet *et al*. used 4.5 mJ/pulse at 1064 nm and 3.8 mJ/pulse at 810 nm to identify and discriminate bacteria.[30]

Figure 3.7 depicts the "blue print" of the optical devices that the laser traverses. The figure also expresses the transmission coefficients of the laser through different branches of the apparatus. It was noticed that the 10 % of the attenuated energy out of laser reached the target surface, therefore, we set the energy to 100 mJ/pulse out of the laser in order to attain 10 mJ/pulse at the on sample.

The main components of LIBS are identified in the exact picture of the experimental set-up, shown in figure 3.8.

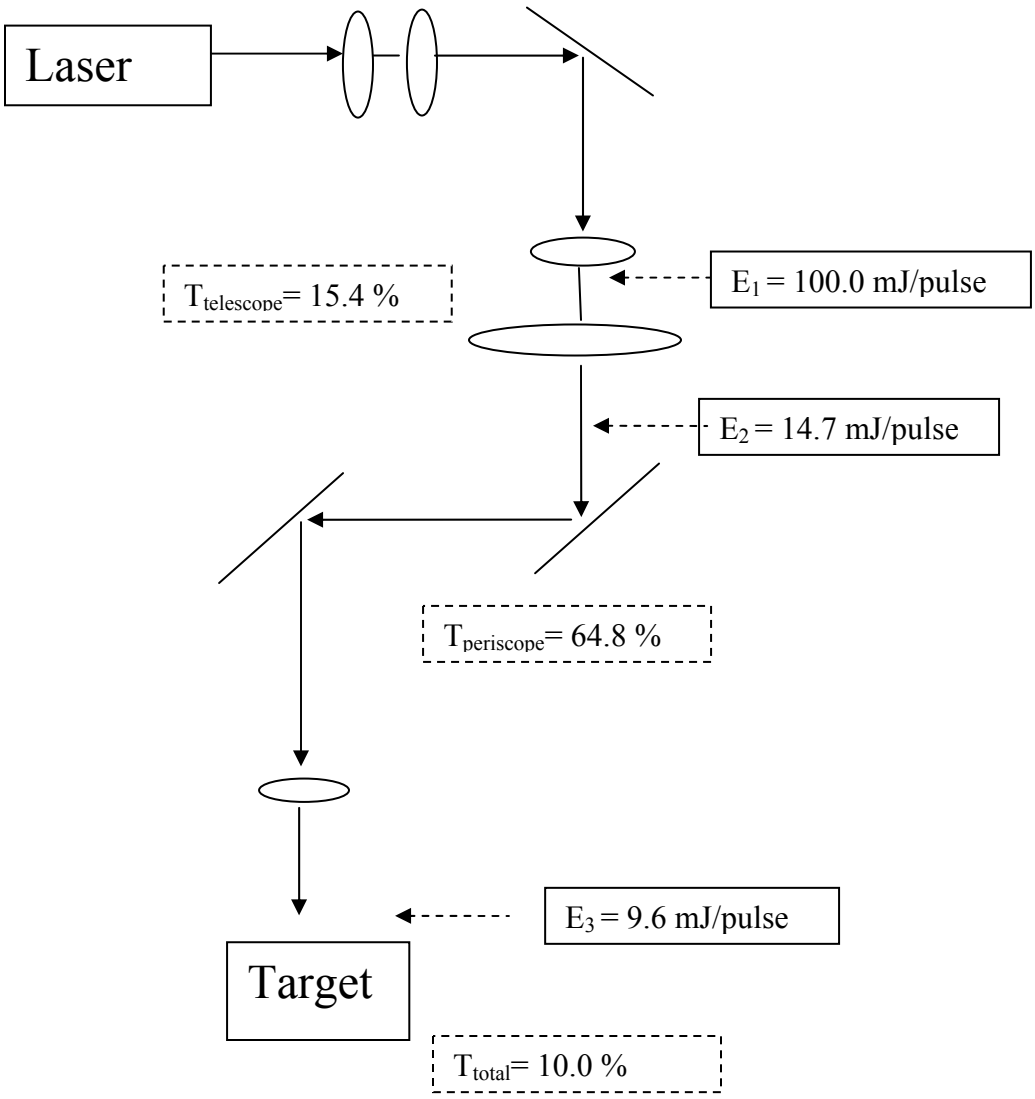

Figure 3.7 The transmission rates through the optical path

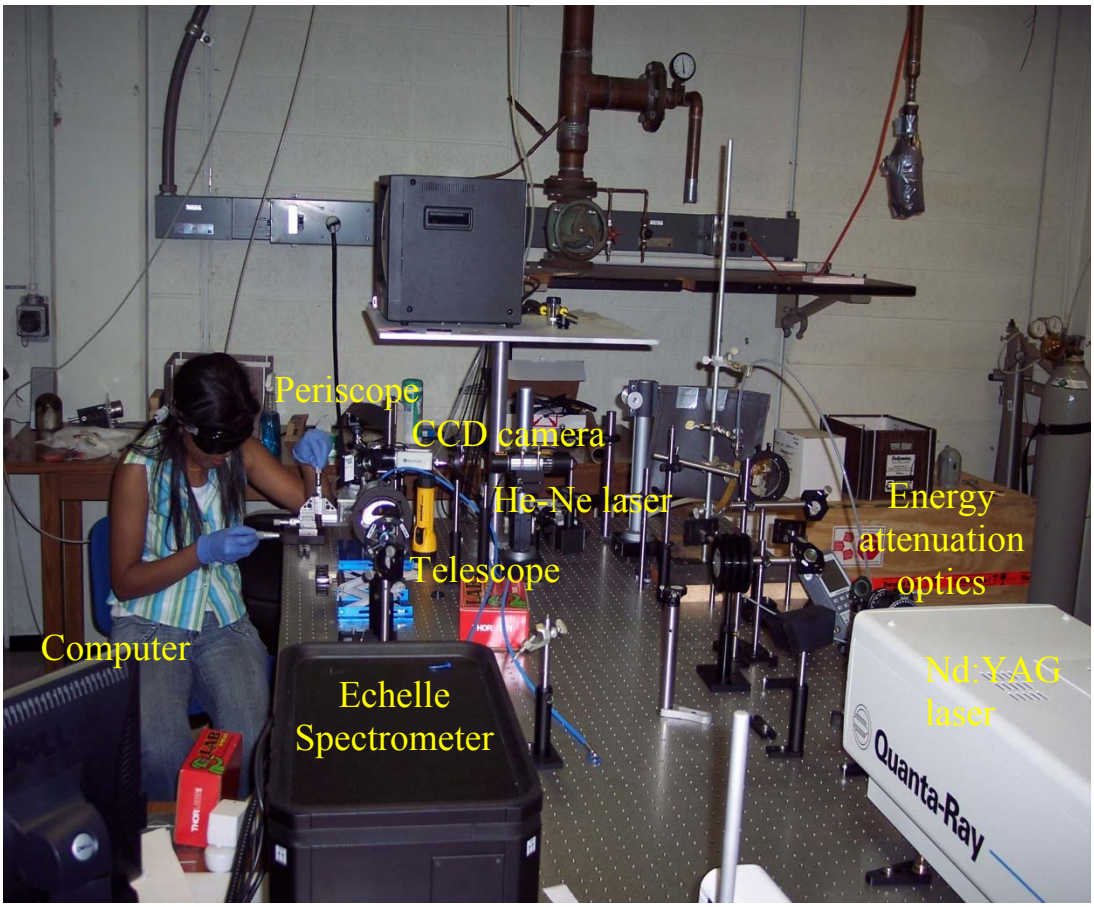

Figure 3.8 The entire LIBS set-up in the laboratory.

3.6 Experimental parameters

As discussed in chapter 2, the most important parameters involved in time-resolved detection are gate delay or delay time, τ_d, the time between the plasma formation and the start of the observation of the plasma light and the second, the gate width, τ_w, the time period over which the light is recorded.

In our experiment on bacteria, in argon environment, LIBS spectra were acquired at both 2 μs and 4 μs delay times after the ablation pulse, with an ICCD intensifier gate width of 20 μs duration. In helium the delay time was set to 1 μs in order to obtain a best signal to noise ratio. Spectra from 5 laser pulses were accumulated on the CCD chip prior to readout. The sample was then translated 250 μm and another set of 5 laser pulses were averaged. 5 accumulations were averaged in this manner, resulting in a spectrum of 25 laser pulses. Typically 15 – 20 such measurements could be made from one colony 24 hours after initial streaking.

3.7 ESAWIN

The Echelle spectrometer was controlled by a PC running manufacturer provided software called ESAWIN. The ESAWIN is a spectrometer system for the simultaneous measurement of complex spectra within the entire UV/Visible range. The main features of the program ESAWIN are control of the hardware of the spectra spectrometer, visualization of data, management of data and analysis of data. The software can be run in two configurations; with hardware control and without hardware control. The latter configuration is useful to process the measurement data on a commercial PC. The measurement data can be simultaneously displayed in different view windows. The view windows have their own toolbars and context menus.

3.8 Sample preparation

The 24 hour old bacterial colonies were grown on a tryptic soy agar (TSA) nutrient medium, and were delivered from the Department of Immunology & Microbiology, Wayne State University. The TSA plates were made as follows: First 10.0 grams of TSA powder (containing NaCl, agar, casein and soybean meal) was added into a flask, containing 250 ml distilled water, inside water bath at 50 °C. Then the flask was kept inside an autoclave (120 °C) for approximately 45 minutes. Next the flask was transferred from the autoclave to water bath and after couple of minutes the solution was poured into a diameter 9 cm sterile Petri dish and left for 1-2 minutes to dry at room temperature. Finally, the dish was placed inside the incubator (37 °C), for 90 minutes to remove the excess moisture on the lid. Then an inoculating loop was heated until red-hot, in order to sterilize the loop. After that one colony or a bit of a colony was picked up from a plate culture and was dragged on the surface of the TSA. Finally the TSA plate was kept inside the incubator for 24 hours to grow bacteria (Fig 3.9). Although I participated in the culturing of such samples, this was routinely done by Dr. Sunil Palchaudhuri, a Professor in the Department of Immunology and Microbiology or his assistant Dr. Ashan Habib.

Figure 3.9 A grown bacterial colony on TSA

3.9 Choice of *E. coli*

In this thesis, the use of LIBS to discriminate the two non-pathogenic strains: HF4714 a laboratory strain and Nino C, an environmental strain, of *Escherichia coli* (*E. coli*) will be discussed. There are two important reasons for utilizing *E. coli* in the project. Firstly, *E. coli* is an important indicator of water contamination. High levels of water borne fecal bacteria are associated with an increased risk of disease for people living in coastal areas. Because of the difficulties in the isolation and detection of pathogens in waste water and sludge, the use of surrogate bacteria has been standard practice in water quality monitoring for some time. For example, Michigan beach water showing 300 or more *E. coli* per 100 ml on a single day is considered out of compliance and results in beach closures. The USEPA has recorded that approximately 40,000 km of streams and coastal waters nationally have levels of bacteria that exceed health standards. This bacterium has been studied extensively at Wayne State University and an expertise exits

in its characterization and preparation. Indeed *E. coli* isolated from the Clinton River and Lake St. Clair watershed have been collected and characterized by Prof. Sunil Palchaudhuri and had been used in this project.

Secondly, *E. coli* is a perfect bacterium to use in this project, because there are several laboratory strains that have been fully characterized, and a direct comparison between these laboratory strains and wild Michigan strains will yield conclusive results as to the limits of discrimination possible with the LIBS technique.

Before doing LIBS these colonies were transferred to the surface of 0.7% agar plate (Fig 3.8a) with a very thin spread (Fig 3.10b). The 0.7% agar plates were prepared in the following way: First 0.7g of agar bacto (Becton, Dickinson and Company, Ref. no. 214010) was added into 125 ml of distilled water and the solution was boiled for 10 minutes (heat = 300 °C, stir =120). Then it was transferred to a small Petri dish (diameter = 5.0 cm) and the top surface was scraped 3 times in order to make it level. It is very important to make the surface level, because height variations in the sample make a huge difference in the spectrum. After that it was allowed to cool for 30 minutes (Fig 3.10a). Finally, the 24 hour old bacterial colony was carefully moved to the top of the agar pate, with a very thin smear. This was done using the stick shown in Fig 3.10b. It was very hard to spread the bacteria on the top of the agar plates smoothly, because the bacterial colonies are very sticky.

The reasons for choosing agar as an ablation substrate was its lack of nutrients, which would affect the bacterial growth, its relatively higher optical breakdown threshold due to optical transparency, and it provided a flat and large area substrate that was easy to prepare.

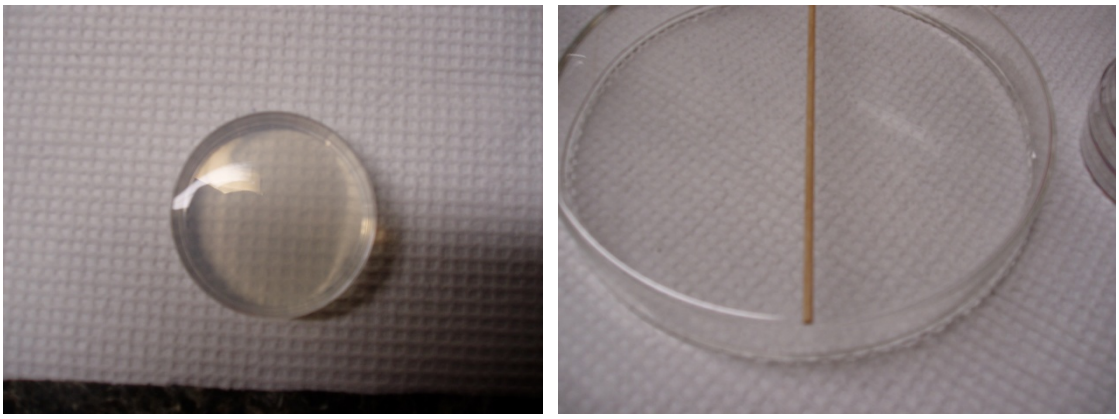

Figure 3.10 a) Agar plate, b) The stick, used to transfer the bacteria to the surface of agar from growth medium and smear in order to make the surface thin.

Due to their close proximity to the laser ablated plasma and the high percentage of liquid in the target materials, the end of the fiber and the exit of aperture of the microscope objective were prone to being coated with a thin film of splattered bacteria and substrate after acquisition of approximately 10-15 spectra from a sample. Frequent cleaning of both fiber and objective were necessary to maintain a constant pulse energy and to insure no optical emission was absorbed.

3.10 The environment

During the experiment the sample chamber, where the sample was ablated was kept at an over-pressure of noble gas (Ar or He). The flow of the gases was kept constant at 10 SCFH throughout the experiment. As discussed earlier, the use of these gases resulted in higher plasma temperature, higher electron density and, despite the lower mass ablation rate, a higher emission intensity for the chosen monitored elements, compared to air.

The experimental comparisons of spectra acquired in air, argon, and helium environments are shown in Chapter 5 “results”. But before examining the experimental

results, we must first examine the statistical analysis technique known as Discriminant Function Analysis (DFA) that must be used to analyze the spectra. This is done in chapter 4.

Chapter 4

Data Analysis

In this chapter, I will discuss the importance of data analysis and the theory behind the analysis technique involved. A data analysis is very important in our experiment because the spectra obtained were subtlety different, but highly similar and a casual or even a detailed inspection does not really work.

There are two commonly used techniques, particularly to discriminate bacteria, known as Principal Component analysis (PCA) and Discriminant Function Analysis (DFA). PCA is a technique used to reduce multidimensional data sets to lower dimensions for analysis whereas DFA is used to determine which variables discriminate between two or more naturally occurring groups.

4.1 Discriminant Function Analysis (DFA)

Computationally, discriminant function analysis is a data analysis technique similar to analysis of variance (ANOVA) which is used to predict and quantify group memberships between two or more groups. It is therefore described more accurately as multi-variate analysis of variance (MANOVA). DFA uses a set of independent variables from each spectrum (each spectrum is treated as a data point) to predict the group membership of that spectrum. Its does so in three basic steps. First, a set of orthogonal discriminant functions is obtained. The discriminant functions are linear combinations of the independent variables which best predict group membership. A canonical correlation analysis produces the successive discriminant functions and their corresponding canonical roots. These are essentially the eigenvalues and eigenvectors of the data,

expressed in a basis that maximizes the difference between groups. For discrimination between N groups, N-1 discriminant functions are made.

Second, a test for significance in the discriminant function is performed. This is done by performing a check on the differences in the means of the groups. The null hypothesis assumes that all data is sampled from a single normal distribution with mean μ and variance σ^2. If the groups are significantly different, they will exhibit means that differ by an amount significantly greater than the variance. In the last step, if significant differences between groups are observed, the group membership of each data spectrum is predicted based on the calculated canonical discriminant function scores for each data spectrum.

In the analysis presented in this work, the LIBS spectra obtained from ablation of the bacteria were analyzed by measuring the intensity of 31 emission lines from 6 different elements. The intensity of each line was divided by the sum of all 31 line intensities to normalize the spectra for shot-to-shot fluctuations and sample density variations. These relative line intensities constituted 31 independent variables that completely described each spectrum and were written as a 1 x 31 vector,

$$x = \begin{pmatrix} x_1 \\ x_2 \\ x_3 \\ . \\ . \\ . \\ x_{31} \end{pmatrix}$$

thus the entire information content of the visible wavelength spectrum was reduced to a single 1 x 31 vector.

All the independent variable vectors from all groups were then analyzed simultaneously by a commercial DFA program (SPSS Inc., SPSS v 15.0) to construct the canonical discriminant functions which were in turn used to calculate for each data spectrum a discriminant function score for that particular function. The N-1 discriminant function scores were found by multiplying the independent variables ($x_{k)}$ by their associated canonical discriminant function coefficients (b_k), summing overall variables, and adding a constant b_0. Therefore discriminant function score *j* is defined as,

$$DFS^{j} = b_0{}^{j} + \sum_{k=1}^{31} b_k{}^{j} x_k \qquad 4.1$$

where, j = 1,2,3,……,N-1, the b's are discriminant coefficients, which maximize the distance between the means of the criterion variable, in other words dependent variable, the x's are discriminating variables, and b_0 is a constant. In this way, N-1 discriminant function scores were calculated for each spectrum or data point.

The canonical discriminant functions and their associated coefficients, b_k, were determined by solving the general eigenvalue problem (T – W) V = λWV, where V is the unscaled matrix of discriminant function coefficients, λ is a diagonal matrix of eigenvalues, W is the within group sum-of-squares-and-cross-products-matrix, and T is the between group sum-of squares-and-cross-products-matrix.

4.1 (a) Eigenvalues

The eigenvalues obtained from matrix λ, also called characteristic roots in this context, reflect the amount of variance explained by the independent variables in a

particular discriminant function and ensure the discriminant functions do not correlate with one another. These eigenvalues also determine the rank of the canonical discriminant functions which are, in practice, always placed in order of decreasing importance to the overall discrimination. In such a way the first canonical discriminant function (DF_1) accounts for more of the variance between groups than the second canonical discriminant function (DF_2), which accounts for more of the variance than the third canonical discriminant function (DF_3), etc. Table 4.1 shows, for example, that 95.8% of the classification is done using function 1, and function 2 only contributes only 3.1% of the classification, while the rest is shared by function 3 and 4. When used to discriminate similar spectra, such as those obtained from bacteria, typically almost all of the variance was described by only the first two canonical discriminant functions.

Table 4.1 The eigenvalues

Function	Eigenvalue	% of Variance	Cumulative %	Canonical Correlation
1	94.491[a]	95.8	95.8	.995
2	3.078[a]	3.1	99.0	.869
3	.734[a]	.7	99.7	.651
4	.282[a]	.3	100.0	.469

a. First 4 canonical discriminant functions were used in the analysis.

4.1 (b) Wilks' Lambda

As well as classifying the groups, the DFA returned parameters that indicated which of the independent variables contributed most strongly to the classification and which had little or no effect on overall discrimination. One such parameter is called the Wilk's lambda, which varies from zero to one. A small Wilks' lambda score indicates a

greater relation to the between-group variance than a large value, i.e. an independent variable with a small Wilk's lambda. Table 4.2 shows the Wilks' lambda results from a test of bacteria and the growth medium TSA. At the left are the 31 lines indentified in the LIBS spectrum. The sodium lines, 588.995 and 589.593 have the smallest Wilks' lambda scores which imply they play an important role in overall discrimination. The Sig column indicates which independent variables don't contribute to the overall discrimination. Any independent variables with a value over 0.10 are considered non-contributing. For example, in table 4.2 the line at 215.408 has a sig value of 0.997 indicating it did not contribute to the discrimination.

Table 4.2 Test of equality of group mean

	Wilks' Lambda	F	df1	df2	Sig.
P203.347	.764	13.163	4	170	.000
P213.546	.577	31.171	4	170	.000
P213.618	.161	222.232	4	170	.000
P214.914	.231	141.149	4	170	.000
P215.294	.891	5.179	4	170	.001
P215.408	.999	.040	4	170	.997
P247.856	.159	224.183	4	170	.000
P253.398	.683	19.735	4	170	.000
P253.566	.272	113.587	4	170	.000
P255.326	.425	57.465	4	170	.000
P255.491	.649	22.983	4	170	.000
P277.983	.788	11.440	4	170	.000
P279.079	.730	15.724	4	170	.000
P279.553	.477	46.646	4	170	.000
P270.806	.637	24.195	4	170	.000
P280.271	.495	43.327	4	170	.000
P285.213	.136	269.876	4	170	.000
P315.887	.394	65.479	4	170	.000
P317.933	.458	50.212	4	170	.000
P373.690	.548	35.029	4	170	.000
P382.931	.850	7.482	4	170	.000
P383.231	.507	41.335	4	170	.000
P383.829	.466	48.618	4	170	.000
P393.366	.194	176.674	4	170	.000
P396.847	.249	128.405	4	170	.000
P422.673	.181	192.051	4	170	.000
P430.253	.547	35.142	4	170	.000
P518.361	.614	26.674	4	170	.000
P588.995	.032	1305.999	4	170	.000
P589.593	.030	1354.454	4	170	.000
P769.896	.777	12.194	4	170	.000

4.1 (c) Standard canonical discriminant function coefficients

The standardized canonical discriminant function coefficients in table 4.3 are the b_k coefficients in equation 4.1 above. These coefficients allow one to determine which variable contributes most significantly to the discrimination. Coefficients with large absolute values correspond to variables with greater discriminating ability. For example, from table 4.3, 588.995 sodium line, 247.856 carbon line and 589.593 sodium line contribute mainly in discrimination by function 1.

Table 4.3 Standardized canonical discriminant function coefficients

	Function			
	1	2	3	4
P203.347	-.031	.177	.405	.199
P213.546	.003	.061	-.007	-.187
P213.618	.211	.020	.808	.604
P214.914	.112	.234	.479	.598
P215.294	-.086	.123	.277	-.023
P215.408	.836	1.021	1.114	.872
P247.856	1.978	3.355	3.375	1.680
P253.398	-.052	-.025	-.351	.223
P253.566	.239	-.110	-.132	.322
P255.326	-.209	.032	.031	.474
P255.491	.001	.080	.014	-.089
P277.983	.021	-.228	-.116	.291
P279.079	-.056	.172	.362	.688
P279.553	1.625	1.751	2.712	3.127
P270.806	.039	.688	.205	-.702
P280.271	1.022	1.098	1.927	-.801
P285.213	.322	.906	.168	.151
P315.887	-.030	.222	.189	-.037
P317.933	.107	.647	.179	.137
P373.690	.096	-.206	-.083	-.071
P382.931	-.107	.039	-.013	-.051
P383.231	.185	.104	.223	-.146
P383.829	-.063	-.051	.579	-.038
P393.366	1.047	1.785	1.440	1.617
P396.847	.811	1.040	.800	.791
P422.673	.018	1.506	1.248	1.170
P430.253	.059	.131	.256	.025
P518.361	.019	.156	.415	.198
P588.995	2.021	2.305	2.104	.909
P589.593	1.905	1.760	2.056	2.046

4.1 (d) Function Wilks' lambda

The Function Wilks' lambda, as opposed to the Wilks' lambda for each independent variable described above, is a measure of how well each function separates cases into groups. This value is shown in table 4.4 for discrimination with four functions. It is equal to the proportion of the total variance in the discriminant scores not explained by differences among the groups. Smaller values of Wilk's lambda indicate greater discriminatory ability of the function. The associated chi-square statistic tests the hypothesis that the means of the functions listed are equal across groups. The small significance value indicates that the discriminant function does better than chance at separating the groups.

Table 4.4 Function Wilk's Lambda

Test of Function(s)	Wilks' Lambda	Chi-square	df	Sig.
1 through 4	.001	1058.405	120	.000
2 through 4	.110	344.916	87	.000
3 through 4	.450	124.955	56	.000
4	.780	38.818	27	.066

4.1 (e) Structure matrix

Another parameter returned by the DFA is called the structure matrix, which shows the correlation of each independent predictor variable with the discriminant function. Shown in Table 4.5 is the structure matrix from an analysis of 5 objects (4 discriminant functions). The 31 independent variables are shown on the left, and the structure matrix shows the importance of that variable to each of the four particular discriminant functions, which are listed across the top. In particular, the asterisks denote

which variables contribute primarily to the functions. Using the structure matrix and the Wilks' lambda, not only could the overall importance of the independent variable be determined, but we could interpret which specific predictor variables each canonical discriminant function utilized to discriminate between groups. Such information was required to obtain a deeper physical interpretation of what the discriminant functions were actually analyzing and what the chemical/elemental basis of the discrimination really was. That being said, it was typically very small, subtle, yet reproducible and real changes in the relative intensities of all the lines that provided the basis of the discrimination. For all the bacteria tested, it was not generally possible to simply state that it was something as obvious as the presence or absence of a single line which allowed discrimination.

Table 4.5 The structure matrix

	Function			
	1	2	3	4
P589.593	.580*	.164	-.177	.307
P588.995	.569*	.154	-.303	-.097
P285.213	-.257*	.140	-.203	.033
P247.856	-.235*	.122	.106	-.137
P393.366	-.210*	-.045	-.021	.080
P396.847	-.178*	-.075	-.144	.055
P317.933	-.111*	.001	.098	-.009
P422.673	-.192	.566*	-.259	.208
P213.618	-.220	-.468*	-.017	.091
P214.914	-.176	-.346*	-.199	.090
P253.566	-.157	-.326*	-.036	.089
P255.326	-.109	-.270*	.131	.039
P383.231	-.099	.127*	-.028	.022
P279.553	-.091	-.252	.394*	-.089
P769.896 [a]	.042	-.086	-.366*	-.001
P270.806	-.064	-.156	.364*	-.171
P280.271	-.087	-.264	.338*	-.165
P279.079	-.057	.005	.285*	.062
P518.361	-.077	.054	.263*	.035
P383.829	-.108	-.029	.210*	.059
P277.983	-.046	-.109	.204*	-.023
P373.690	-.092	-.026	.173*	-.086
P430.253	-.088	.160	.162*	.025
P315.887	-.127	-.039	.129*	.008
P382.931	-.042	.003	.116*	.023
P203.347	-.054	-.090	.109*	.055
P253.398	-.069	-.067	-.092*	.039
P213.546	-.086	-.083	-.037	-.206*
P255.491	-.073	-.109	.040	-.122*
P215.294	-.035	-.020	-.040	-.119*
P215.408	.002	-.009	.012	.033*

Pooled within-groups correlations between discriminating variables and standardized canonical discriminant functions
Variables ordered by absolute size of correlation within function.

*. Largest absolute correlation between each variable and any discriminant function

a. This variable not used in the analysis.

4.1 (f) Discriminant function analysis plot

The information contained in each spectrum or data point was thus reduced to N-1 discriminant function scores. Discriminant function score 1 represents the most distinct or obvious differences between spectra while discriminant function score 2 is used as the ordinate. Discrimination among many groups will possess more than two canonical discriminant function scores, but these typically perform very little discrimination and are not usually utilized. Spectra created from the members of the same groups should exhibit scatter about a mean μ which is not a value, but an N-1 dimensional vector. The within-group variance is a measure of that scatter and should be significantly less than the difference of between-group mean and would maximize the distance between groups. On a discriminant function graph, this would be represented by highly isolated clusters of tightly clumped data points, as shown in figure 4.1.

Figure 4.1 is obtained with the data collected in the past by our group. The figure shows the discrimination between two *E. coli* strains (Nino C and AB) and TSA, the growth medium, on which they were grown, obtained in air environment. Each spectrum becomes a data point. Since three groups are taken for analysis, two discriminant functions (DF1 and DF2) are produced. DF1 mainly discriminates the bacteria from the growth medium whereas DF2 shows the discrimination between the two *E. coli* strains.

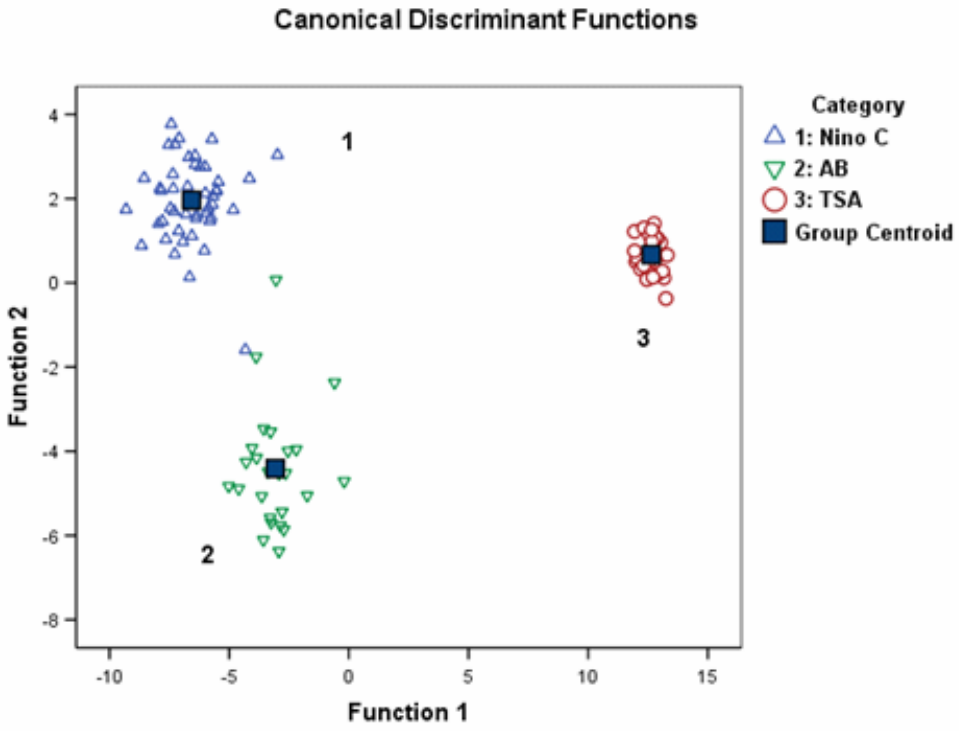

Figure 4.1 The discriminant function analysis plot of two *E. coli* strains and TSA obtained in an air environment.

4.2 Summary

To complete identification based on a discriminant function analysis, samples with known identification must first be obtained to construct the required canonical discriminant functions. The DFA cannot identify unknown members of a group without first having known members to compare them to. Therefore the LIBS technique coupled with a DFA is not suited for random identification of completely unexpected or unknown pathogens. It is particularly useful, however, for identifying particular strains of a pathogenic agent, or diagnosing which species of a particular micro-organism is responsible for a given infection.

Chapter 5

Results

In this chapter, a detailed description of data and the results are given. As mentioned in chapter four, the spectra obtained from different strains of *E. coli* ablated in different gases were very similar. Therefore, a more detailed analysis becomes necessary. A typical LIBS spectrum of an *E. coli* (HF4714) in argon is shown in figure 5.1(a), where the y coordinate points the intensity and the x coordinate shows the wavelength in nanometers (nm). In the figure, the atomic emsision lines from many inorganic elements (labelled) appear in the UV/blue end of the spectrum, while the infra-red end of the spcetrum (lines with wavelength grater than 700 nm) is dominated by emission from the environment gases (argon).

Figure 5.1(b) is the typical LIBS spectrum of *E. coli* (HF4714) in helium. The y coordinate gives the intensity and the x coordinate shows the wavelength in nanometers. The 31 spectral lines of six major elements; phosphorus, calcium, magnesium, sodium, potassium, and carbon, and the helium line (environment gas) are visible in the spectrum.

As mentioned in the introduction chapter, only 19 emission lines were found in air. But an additional 12 emission lines were seen in noble gas which add up to 31 spectral lines. The list of all 31 lines is shown in table 5.1.

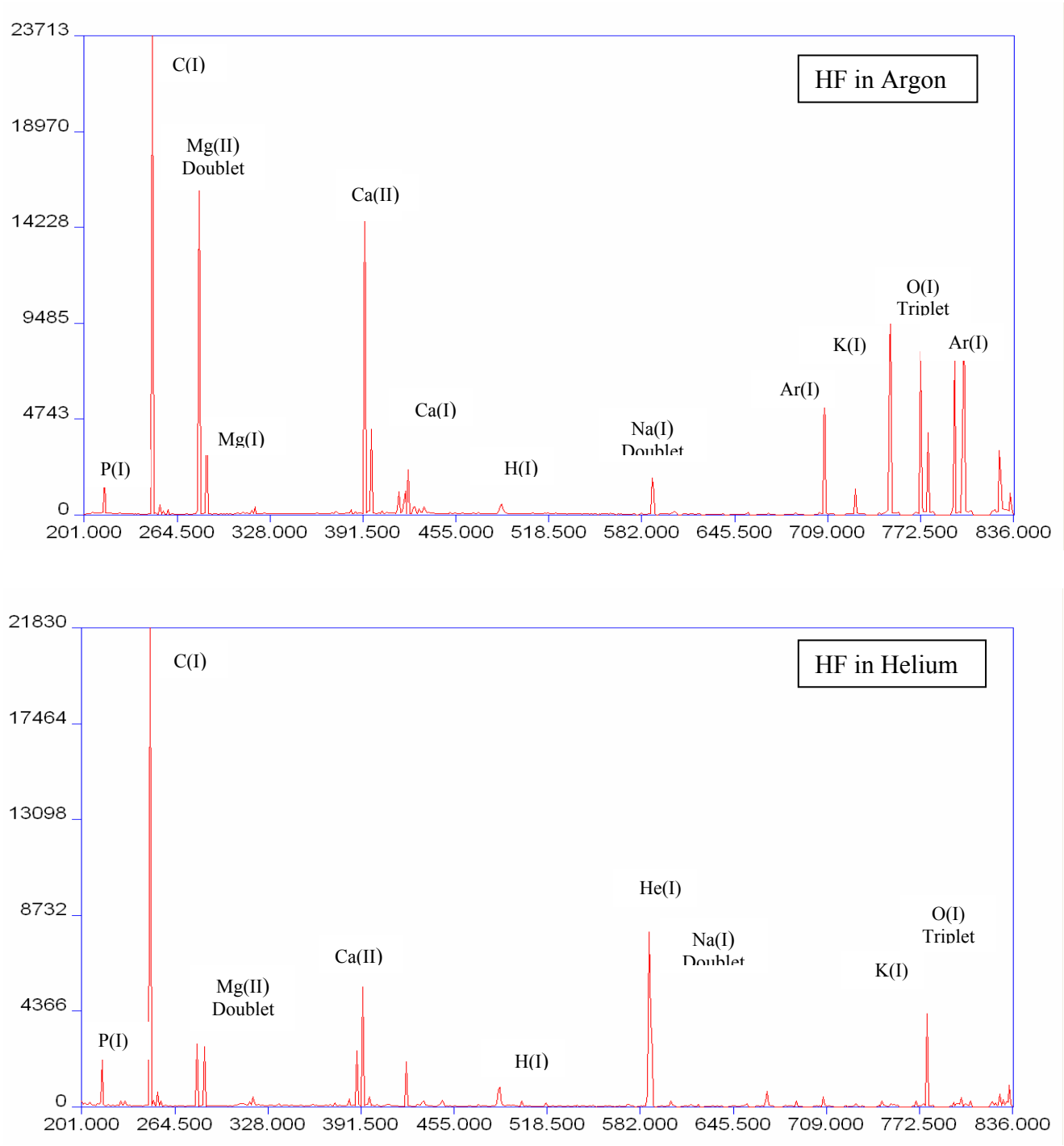

Figure 5.1(a) The LIBS spectrum of HF 4714 in argon, (b) The LIBS spectrum of HF 4714 in helium. In both spectra the 31 spectral lines of six major elements – P, Ca, Mg, Na, K, C – are shown.

Table 5.1 The list of 31 emission lines, visible in the enviornment of noble gas. LIBS spectrum of *E. coli* ablated in an enviornment of noble gas. The idnetifier "I" indicates a neutral atom, the identifier "II" indicates a singly ionized ion.

Wavelength (nm)	Line identification
203.347	P I
213.546	P I
213.618	P I
214.914	P I
215.294	P I
215.408	P I
247.856	C I
253.398	P I
253.56	P I
255.491	P I
277.983	Mg I
279.079	Mg II
279.553	Mg II
279.806	Mg II
280.271	Mg II

Wavelength (nm)	Line identification
285.213	Mg I
315.887	Ca II
317.933	Ca II
373.69	Ca II
382.931	Mg I
383.231	Mg I
383.829	Mg I
393.366	Ca II
396.847	Ca II
422.673	Ca II
430.253	Ca I
518.361	Mg I
585.745	Ca I
588.995	Na I
589.593	Na I
769.896	K I

Therfore, a new standard region of interest (ROI) was created, including those new visible emission lines. Figure 5.2 shows the ROI view of figure 5.1(a). The line plot in red is the intensity versus x-pixel coordinates for 60 pixels and the center of the peak is shown as a green vertical line. The text left above denotes the element of interest whereas the number below each box gives the wavelength (in nanometers) of the position in the middle of the window. The number above the window is the peak area and the number above this is the ratio of the peak area to certain reference lines (not used in our analysis).

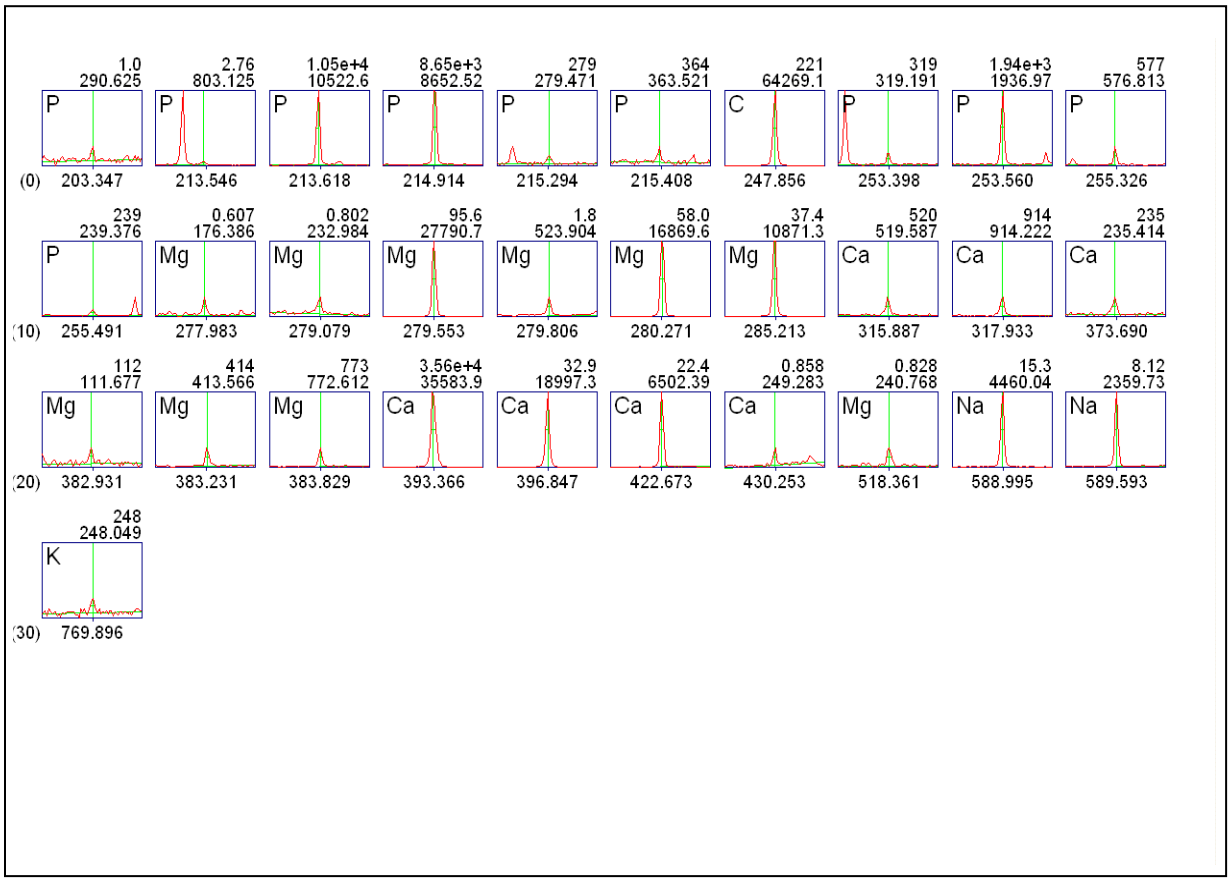

Figure 5.2 The ROI view of the spectrum shown in figure 5.1.

5.1 Results of parameters

The most important parameters in our experiments were the delay time (τ_d), gate width (τ_w), the number of CCD on-chip accumulations (OCA), laser pulse energy, and the number of averaged accumulations to increase the signal to noise ration.. With the intention of observing as much optical emission as possible, the gate width was set to 20 μs. Also the pulse energy at the target was adjusted to be 10 mJ/pulse. The parameters were checked in the argon environment. A constant flow of gas, 10 standard cubic feet per hour (SCFH), was maintained inside the chamber.

5.1 (a) Gate delay

The gate delay is defined as the time between the plasma formation and the start of the observation of the plasma light and the second. Figure 5.3 shows the result at different delay times on Gram negative bacteria, HF 4714, grown in TSA. The 1 μs spectrum gives an enormous background compared to 2 μs and 4 μs. Though the 2 μs plot has a pretty large background, it gives a good signal to noise ratio compared to 4 μs. But 4 μs gives the least background, therefore, the experiments were done mostly at a delay time of 4 μs. Similarly, in a helium environment, it was found 1 μs delay time produced better spectra.

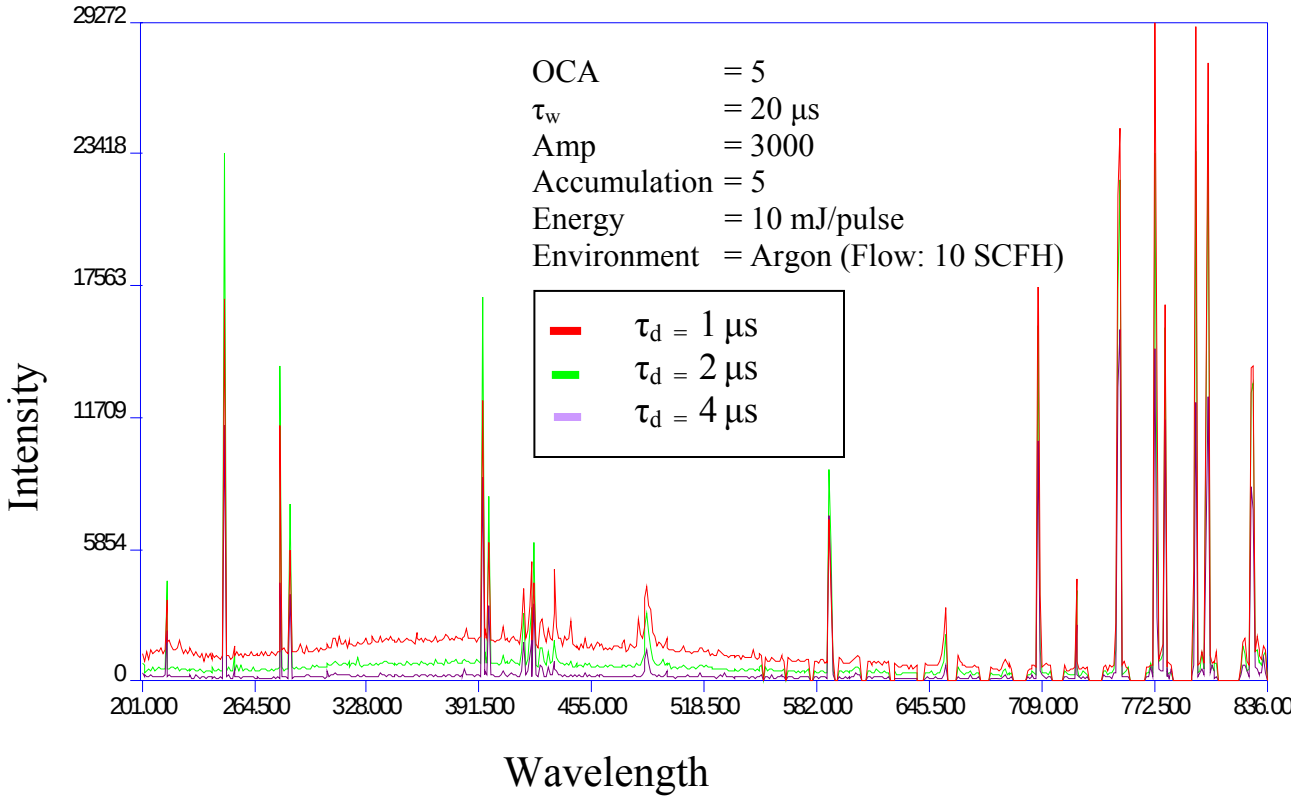

Figure 5.3 The spectrum of Gram-negative bacterium, HF grown in TSA, taken at different delay times in argon environment.

5.1 (b) On-chip accumulations (OCA)

Figure 5.4 illustrates the result of using different OCA values, number of laser pulses, on the same HF 4714 bacteria, grown in TSA. 10 OCA gives a very high signal compared to 1 OCA and 5 OCA, with a significant background. The reason could be after 5 on-chip accumulations a very small amount of bacteria would be left out, as a result a small amount of agar will get ablated during 10 accumulations, and the background goes up. It is obvious from the plot that 1 OCA cannot be used since it provides extremely small signal. 5 OCA gives better signal with minimum background.

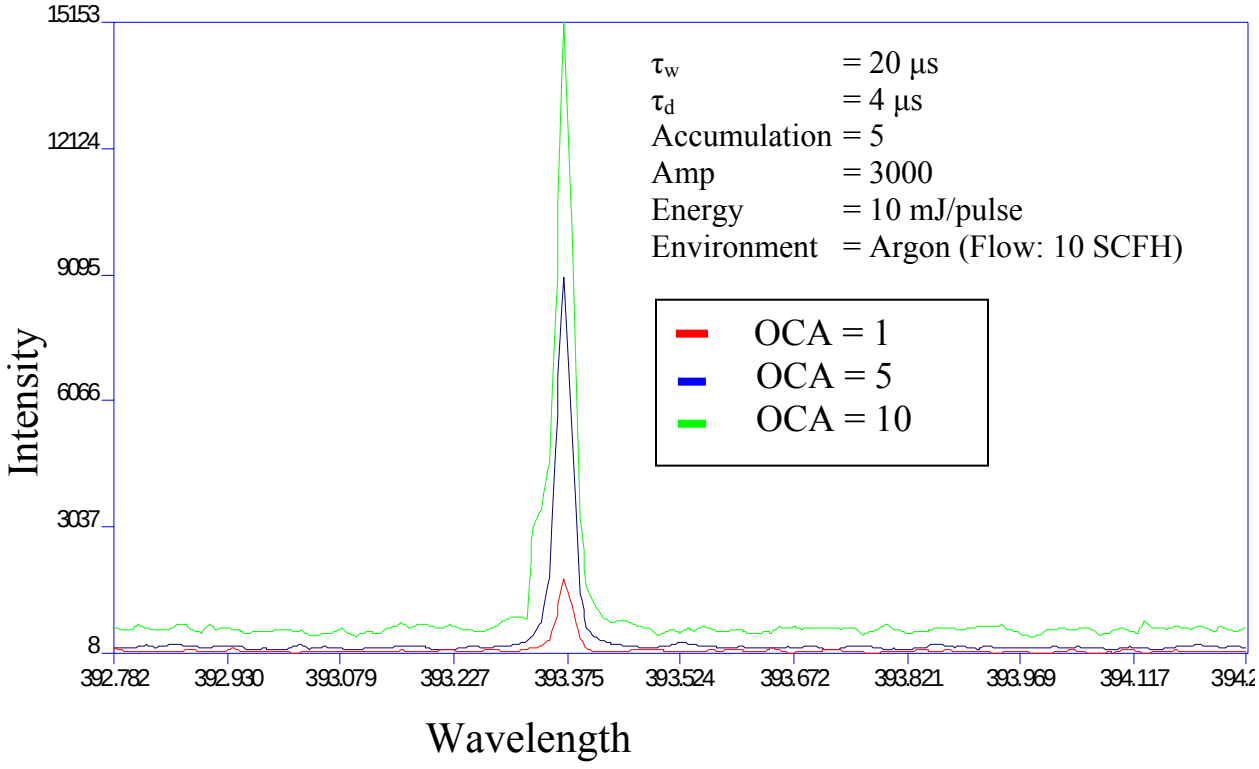

Figure 5.4 The spectrum of HF grown in TSA, with different on-chip accumulations (OCA) in argon environment.

5.1 (c) Accumulations

Figure 5.5 shows the spectra of HF 4714 obtained with different numbers of accumulated spectra; which is the number of spectra averaged for a single data point. The result of a single accumulation shows large noise compared to 5 and 10 accumulations in figure 5.5 (a). More accumulations imply better signal to noise since the noise is averaged away when 5 or 10 spectra are averaged for the final spectrum. Comparing accumulations 5 and 10, as shown in figure 5.5 (b), although they both give good signal to noise ratio, in order to get more measurements from a bacterial colony, we decided to stick with 5 accumulations as a compromise. Utilizing 10 accumulations would give better signal to noise ratio, but would reduce the overall number of measurements.

(a) (b)

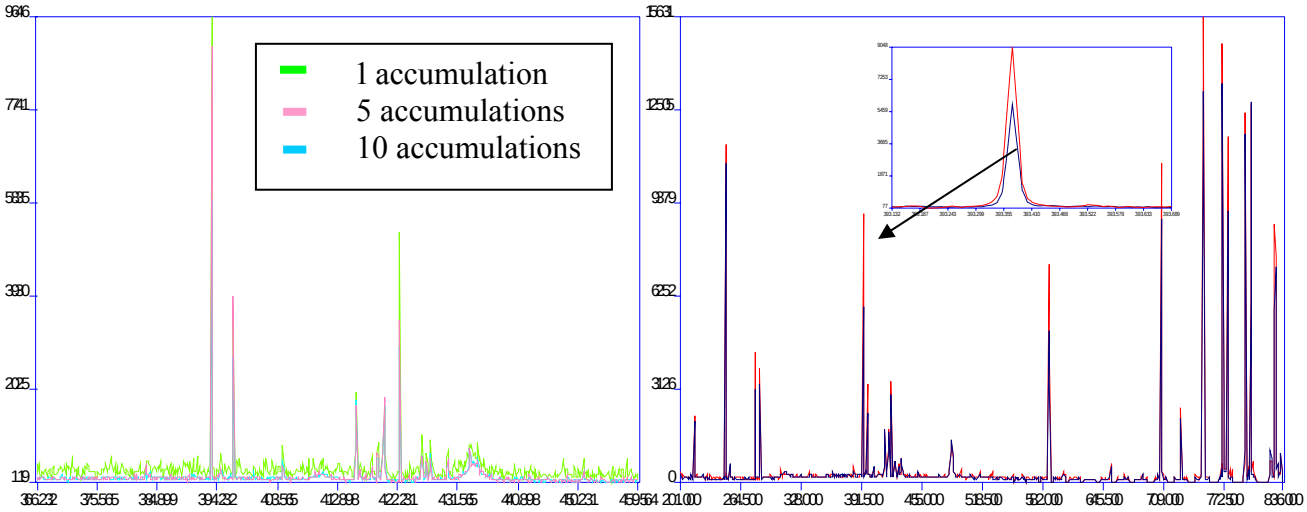

OCA	= 5
τ_d	= 4 µs
τ_w	= 20 µs
Amp	= 3000
Energy	= 10 mJ/pulse
Environment	= Argon (Flow: 10 SCFH)

Figure 5.5 (a) The spectrum of HF grown in TSA, obtained with three different accumulations in argon environment, (b) Comparison between 5 accumulations and 10 accumulations.

After choosing the appropriate parameters, data were taken. As discussed in chapter 3, the target or the sample was kept inside the gas chamber filled with helium or argon. The important reason for flushing noble gas into the chamber is that this enhances the signal to noise ratio. Figure 5.6 illustrates the spectrum of the second kind of bacteria, Nino C, taken in argon, helium and air environment. Argon produces the higher emission intensity, due to its ability to be efficiently heated by inverse Bremsstrahlung. Though the background of argon is noticeably high, it gives the best signal to noise ratio. Compared to air, the use of helium creates a much improved emission signal.

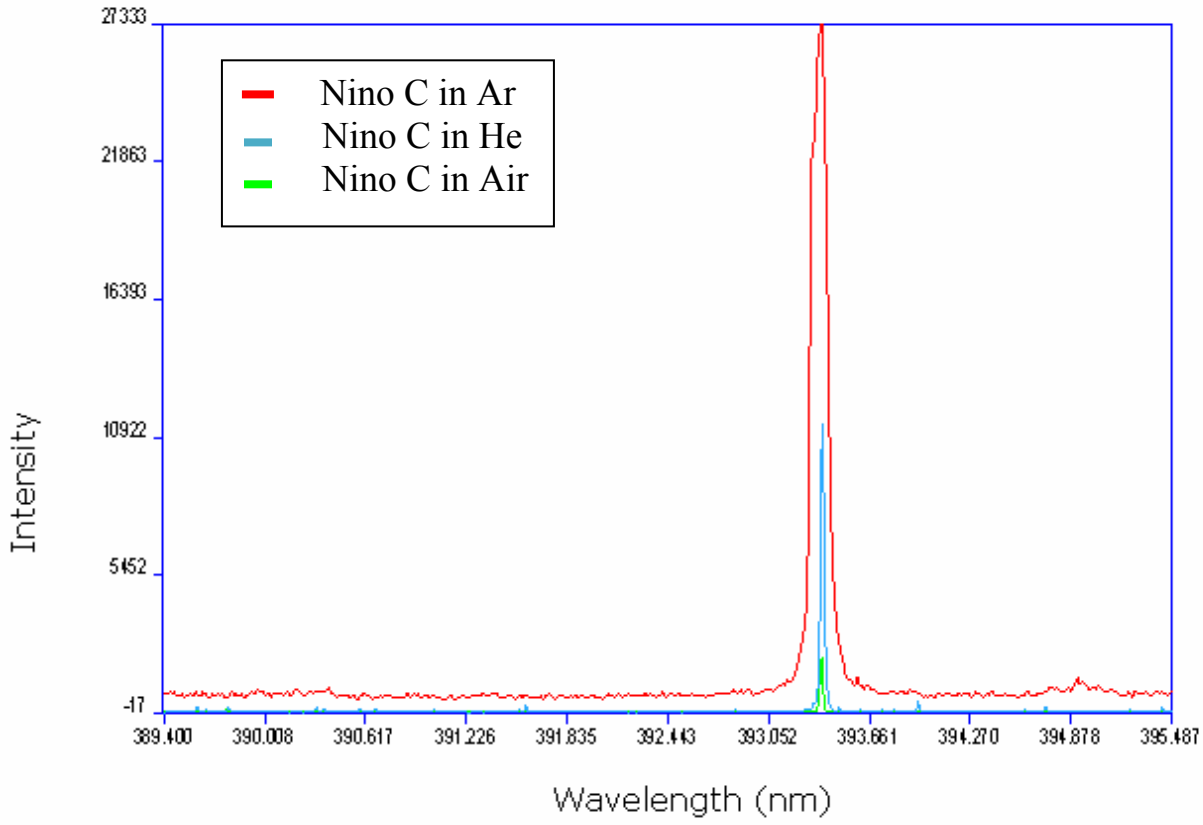

Figure 5.6 The spectrum of Gram-negative bacteria, Nino C, in argon, helium and air environment. The region around the Ca II line at 393.366 nm is shown.

As emphasized in chapter 4, a full spectrum data analysis is very important in our experiment because the spectra obtained were subtlety different, but highly similar in that a casual or even a detailed inspection does not really reveal the differences. Figure 5.7 (a) shows the spectra of HF 4714 and Nino C grown in TSA in helium environment (b) HF 4714 and Nino C grown in TSA in argon environment.

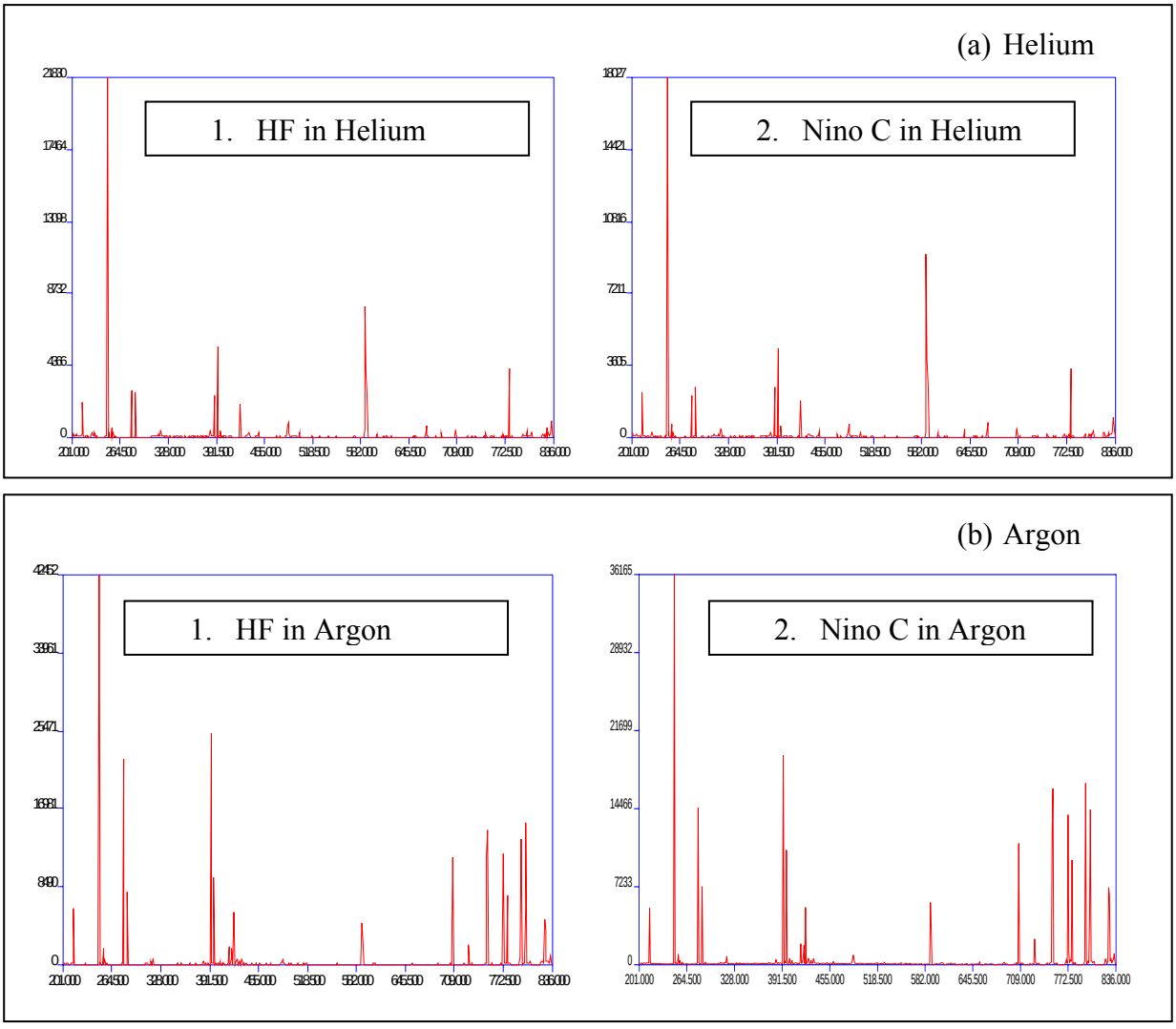

Figure 5.7 (a) The spectra obtained in helium gas environment; 1. A typical spectrum of HF4714, 2. A typical spectrum of Nino C (b) The spectra obtained in argon gas environment; 1. A typical spectrum of HF4714, and 2. A typical spectrum of Nino C. The spectra are plots of intensity (arbitrary units) versus wavelength (nm).

At this point, it is important to show the LIBS spectrum produced by agar and TSA, the growth medium to make sure they are different from the spectra of bacteria. Figure 5.8 shows a typical spectrum of TSA. The spectrum contains much less or no emission from inorganic elements which dominated the bacteria spectrum, except sodium. The reason is sodium chloride comprises the highest percentage in the TSA. On the right hand side of the spectrum, the spectral lines corresponding to environmental gas, argon, can be seen.

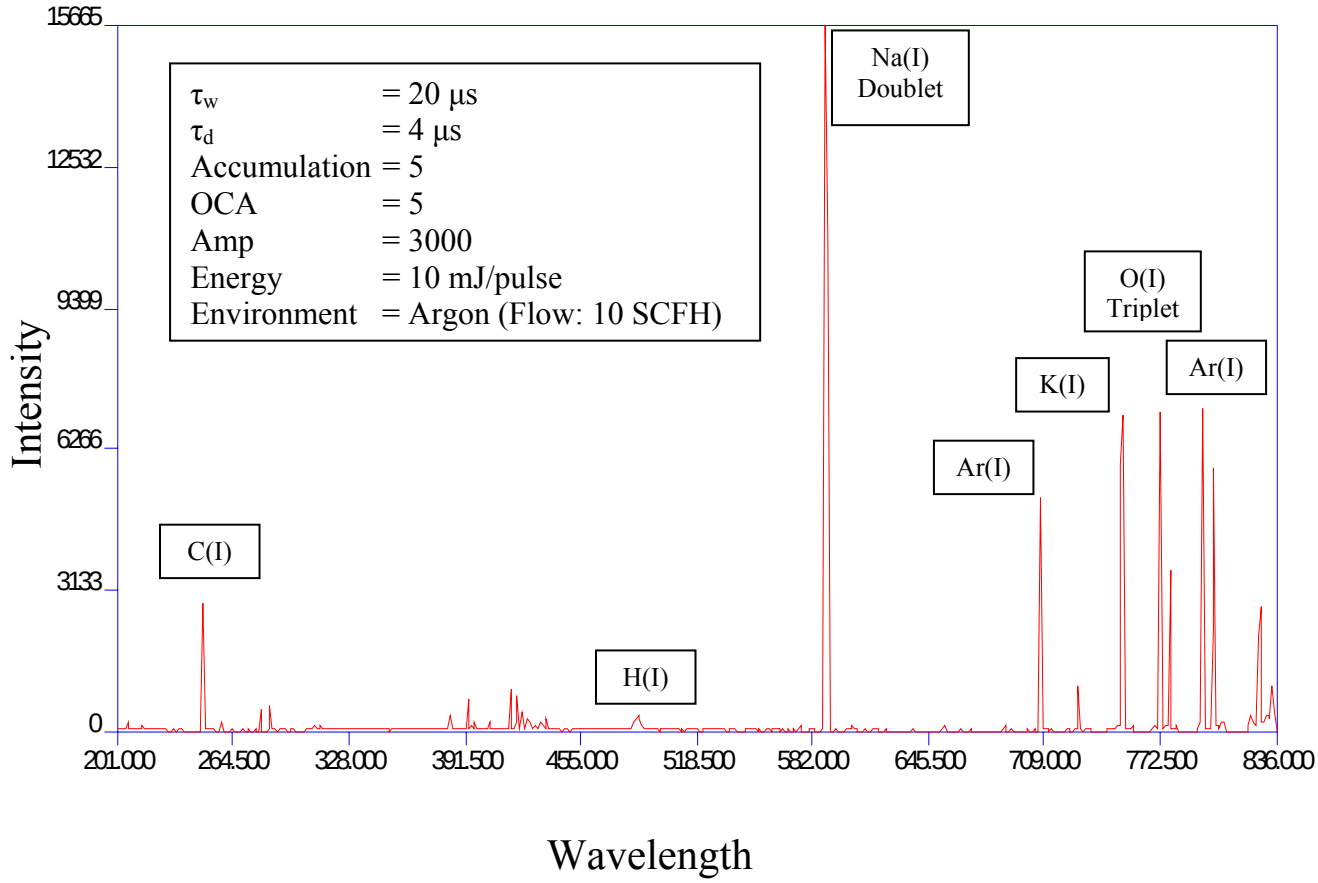

Figure 5.8 The typical spectrum of TSA in argon

Similarly a typical spectrum of 0.7% agar, which has no nutrients at all, is shown in figure 5.9. This shows no inorganic emission lines other than hydrogen line, which apparently comes from water. The argon lines also appear in the agar spectrum. This confirms that the spectrum of bacteria is completely different from the spectrum of agar or spectrum of TSA.

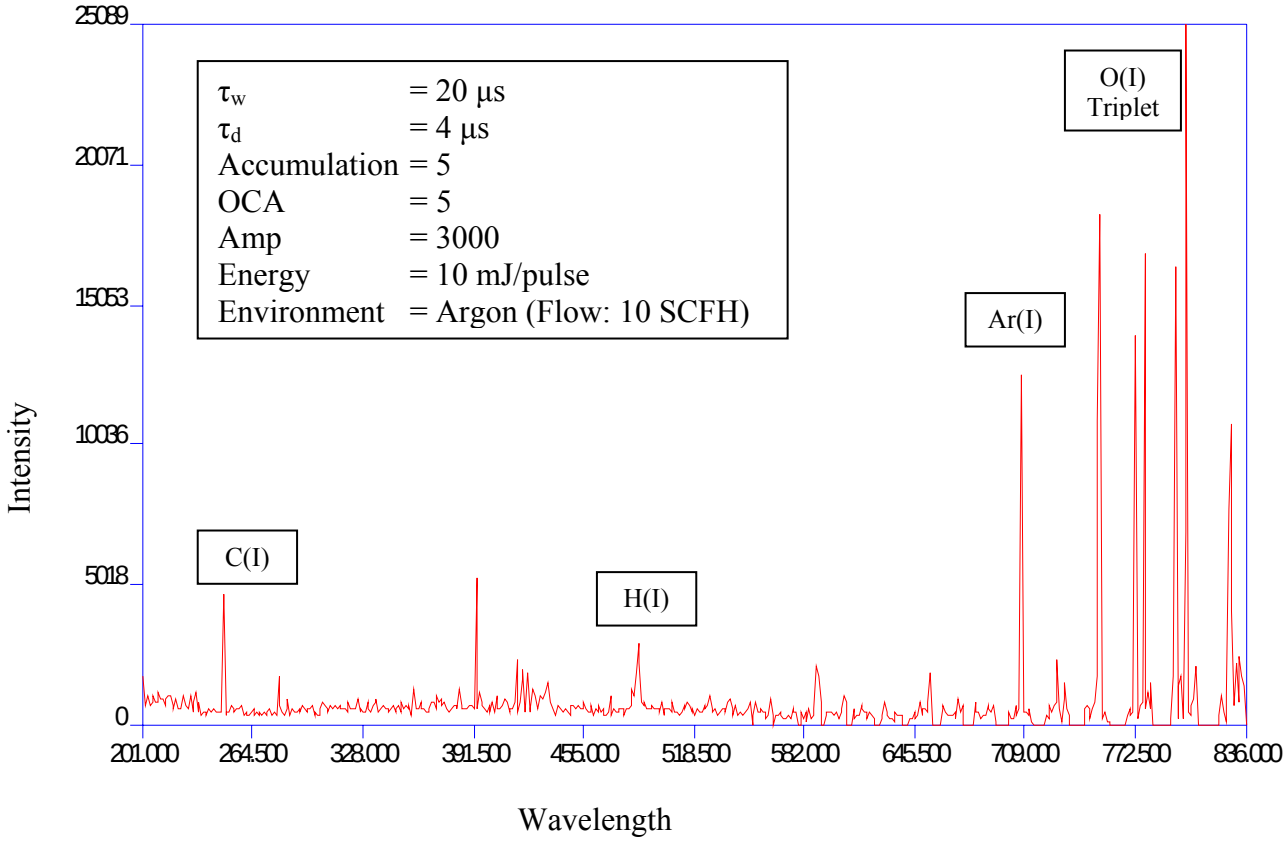

Figure 5.9 The typical spectrum of 0.7% agar in argon environment.

To quickly and conveniently analyze the data, we needed a fairly automated way to obtain the 31 emission peak areas from each spectrum obtained in the ROI view shown in Figure 5.2. To analyze this data, each spectrum file (of type ".spe") was converted to a text-formatted ".dat" file. Figure 5.10 shows the excel sheet of the ".dat" ROI data shown in figure 5.2. The third column in the sheet (marked in "bold") contains the area under the peak. In order to extract only these values from the files, an MS Excel macro was written (see Appendix A). This macro selected the area under the peak, corresponding to each emission line from each data file, created a new excel worksheet and pasted just the areas into this sheet. In other words, first the macro opens a data file and collects the values in C11, C13, C15,…….,C71. Then it creates a new excel book called "Final_data.xls" and saves these numbers in a row. It then repeats the same procedure to the arbitrary number of data files in a particular folder (and there could be around 100 files generated per day) and saves all the data in "Final_data.xls", shown in figure 5.11.

Rather than using the raw emission peak intensities, each intensity was normalized by dividing it by the sum of all peak intensities in that spectrum called the total spectral power. These 31 numbers were then input into a commercial program (SPSS Inc., V 15.0) which performed the discriminant function analysis (DFA).

	A	B	C	D	E	F	G
1	ROI file: bacteria090607.roi						
2	--: --						
3	Output Conc / Ratio						
4	Gate Delay 2 µs						
5	Gate Width 20 µs						
6	Amplification 3000						
7	On-Chip Accus 5						
8	FL Voltage -----						
9	Clean Pulses 0						
10	Pixel Shift 0.0 -2.0						
11	P	0.213618	**4605.44**	4.61E+03	4.61E+03	6	
12	3861	3837	3845	3919	3861	3877	3897
13	P	0.214914	**3828.11**	3.83E+03	3.83E+03	6	
14	3840	3823	3873	3956	3902	3885	3868
15	C	0.247856	**45197**	4.52E+04	4.52E+04	6	
16	4124	4065	4085	4042	4109	4100	4126
17	P	0.25356	**3077.03**	3.08E+03	3.08E+03	6	
18	3987	3971	4018	4005	3978	4055	4012
19	Mg	0.279553	**59634.3**	5.96E+04	5.96E+04	6	
20	4356	4388	4476	4458	4324	4329	4271
21	Mg	0.280271	**24936.9**	2.49E+04	2.49E+04	6	
22	4177	4276	4278	4239	4368	4318	4225
23	Mg	0.285213	**26053.8**	2.61E+04	2.61E+04	6	
24	4364	4359	4461	4443	4368	4357	4284
25	Ca	0.393366	**66132.6**	6.61E+04	6.61E+04	6	
26	5148	5317	5119	5129	5220	5045	5107
27	Ca	0.396847	**17258.3**	1.73E+04	1.73E+04	6	
28	4760	4724	4698	4677	4585	4444	4299
29	Ca	0.422673	**14573.3**	1.46E+04	1.46E+04	6	

Figure 5.10 The data file of the ROI view shown in figure 5.2 which contains the numeric details of the corresponding spectrum.

A	B	C	D	E	F	G	H	I	J	K	L	M	N	O
HF1_1		4163.41	3455.16	38062.2	2855.15	49782.9	22562.8	22312.8	58608.4	14232.3	13445.9	22545.1	9945.16	681.241
HF1_2		4605.44	3828.11	45197	3077.03	59634.3	24936.9	26053.8	66132.6	17258.3	14573.3	30066.4	14405.4	1017.36
HF1_3		4133.92	3426.75	43989.1	2557.88	52386.3	23115	23855.3	55648.9	15005.7	12383.8	29994.5	12248.4	1265.04
HF1_4		3914.83	3371.67	42871.4	1982.75	73464.1	27926	22181.1	83080.6	17587	14603.3	30006	15881.4	778.185
HF1_5		3180.07	2571.13	39058.8	1529.13	64914.9	24427.3	19200.7	75748.1	16176.6	12015.3	22350.2	11708.7	876.87
HF1_6		3385.81	2415.97	33561.5	1964.65	50179	21790	17996	62954.3	13899.7	11425.3	16571.6	7609.13	867.273
HF1_7		4543.95	3448.78	45658.2	2888.36	69620.4	27768.8	25132	96516.6	20896.8	15452.3	31232.5	15591.9	971.873
HF1_8		3080.89	2828.8	29911	2144.8	47568	20459	15104	55087.2	13561.5	10919.7	19635.2	9186.2	0
HF1_9		2980.5	2404.57	31712	1681.5	46197.1	19816.1	18125.1	66672.7	15429	11864.1	16278.3	7366.62	1028.56
HF1_10		4732.66	3871.18	57229.9	3583.78	100172	36566.1	29702.1	125371	28831.7	20145.4	27423	11912.1	746.567
HF1_11		2358.39	1633.87	25093.4	1422.89	45814.9	20378.3	14825.9	60542.1	15259.2	10082.2	12451.1	4788.01	438.648
HF2_12		4376.06	3743.71	42315.1	2559.4	50908.2	22375.5	23589.8	68910.4	16960	12831.3	29642.4	15133.3	1274.41
HF2_13		3890.46	3111.53	44318.3	2332.46	63301.2	28389	20867.6	96427.4	20676.9	15215.3	31523	14169.3	956.422
HF2_14		3401.66	3093.36	39304	1958.37	59998.1	23550.3	17887.8	78377.3	19166.9	10368.2	21190.1	10455.7	531.054
HF2_15		2423.23	2188.76	33294.7	2138.6	53263.3	25149.4	13595.4	84971.9	16775.8	7649.35	17832.6	8589.04	721.85
HF2_16		3086.73	2287.36	32210.6	1728.64	55343.4	23492.2	16770.2	72279.7	16540.2	7894.18	15016.6	4719.76	457.266
HF2_17		3658.5	2945.54	46680.8	2395.54	55493.9	24875.3	22444.3	69698.1	18861	14083.7	30283.3	14719.1	977.451
HF2_18		4832.11	3677.54	47176.2	2896.62	67874.7	29445.1	22658.8	83820.3	19651.8	13924.9	28431.7	13231.8	1230.4
HF2_19		4074.86	3360.46	40967.6	2358.86	75294.8	28721	18825.6	67222.6	16998.8	11797.7	24467	14219.2	1478.72
HF2_20		3804.82	3647.94	45725.5	2206.51	66928.6	26190.1	21400.9	65558.8	17463.8	14083	27705.8	14859.9	799.056
HF2_21		5353.19	4475.51	65587.6	3391.22	91246.9	38167.2	31688.4	146305	31315.8	20000.4	42834.2	24026	884.82
HF2_22		5126.78	3800.94	51406.6	2761	80851.8	32296.3	26514.6	104112	21205	15215.7	39614.6	18067.5	1082.25
HF2_23		2498.26	1902.45	29065.4	1326.31	39904.7	17842.1	12735.4	45082	11724.7	7629.08	16100.5	10352.1	1096.97
HF3_24		3885.48	3651.21	46324	2749.61	49498	22247.3	20177.7	59895.9	14665.1	11614.5	43960.3	22377.1	1188.59
HF3_25		4303.52	2995.75	49393.1	2403.98	48670.4	20350.9	19276.4	55706.5	14202	13690.6	38104.2	21292	1128.78
HF3_26		2503.57	2803.19	33487.9	1483.11	33098.9	14300	14113.4	36185.3	10788.4	8931.24	26171.8	14812	2078.85
HF3_27		3143.52	2644.42	34134.1	2239.29	30404.8	12393.1	14970.2	30947.1	9380.45	10184.8	26678.5	13340.8	1311.03
HF3_28		3908.29	3217.95	37662	2373.4	49010	19719.8	20372.9	48688.6	12168.9	11737.5	24597.3	10788	1238.36
HF3_29		2748.4	2041.9	36218.6	1659.47	33831.7	15197	12517.9	46611.5	13663.9	9814.99	26564.4	12736.2	895.504
HF3_30		3157.61	2421.77	39325	2134.71	34071.9	14680.3	14398.5	46472.4	13543.5	13605.1	33720.2	20367.4	1461.25
HF3_31		3462.63	3024.12	42560.1	2132.49	46055.9	20260.1	17233.5	49451	13507.9	13136.4	39383.3	22312	1450.77
HF3_32		2608.83	2011.37	37789.6	1665.96	32192.2	13328.1	13062.1	35862.2	11217.1	10790	31548.8	16869.3	753.541
HF3_33		2316.29	1797.55	29117.2	1321.84	29076.1	11882.9	10503.5	36808.3	11277.9	9293.68	26245.6	15350.9	1309.62
HF3_34		3525.36	2700.95	40590.2	2377.68	48155.6	21316.8	16709.2	53854.2	14317	13691.2	37060.3	19665.6	1481.91

Figure 5.11 A typical "Final_data.xls". The file names are listed in column A and the columns represent the 31 elements in the order.

5.2 DFA results

5.2 (a) Argon results

As mentioned before in this chapter, the experiments were done with both delay times of 2 and 4 microseconds in argon.

5.2 (a) 1. With delay time = 4 µs

Figure 5.12(a) shows the DFA plot of two *E. coli* strains (Nino C and HF4714) and TSA on which they were all grown, in argon. Function 1 discriminates the bacteria from its growth medium, whereas function 2 discriminates the two different bacteria.

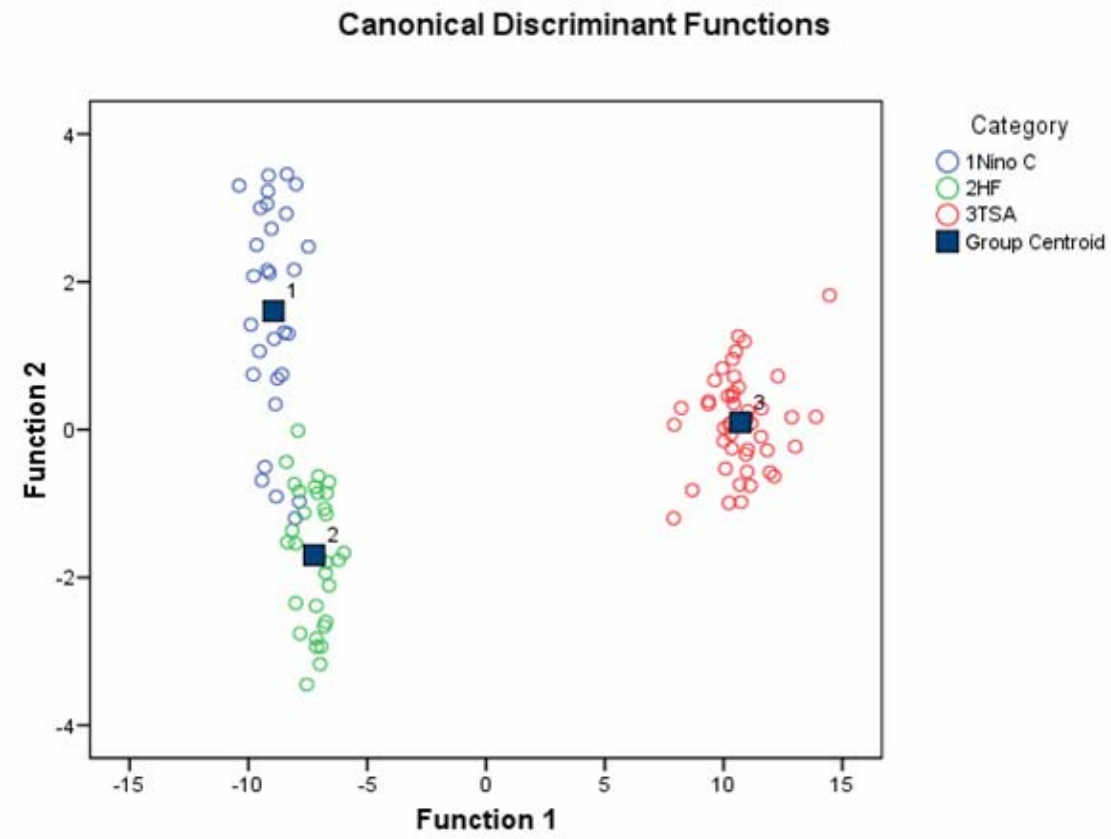

Figure 5.12 (a) The discriminant function scores of two *E. coli* strains and the TSA growth medium.

The difference betwwen the TSA and bacteria in DF1 is larger than the difference in DFA2 between bacteria. This demonstrate that LIBS can easily discriminate between the microorganism of interest and potential environmental contamination. In this analysis, all group memberships were predicted correctly 100.0% of the time, with 98.2% of variance between groups represented by DF1 and 1.8% by DF2. Figure 5.12 (b) shows these eigenvalues of the results. Figure 5.12 (c) tells that the 100.0% of original grouped cases are correctly identified and 87.9% of cross validated grouped cases are correctly identified.

Eigenvalues

Function	Eigenvalue	% of Variance	Cumulative %	Canonical Correlation
1	89.423[a]	98.2	98.2	.994
2	1.608[a]	1.8	100.0	.785

Figure 5.12 (b) The eigenvalues produced by DFA for the above test

Classification Results[b,c]

			Predicted Group Membership			
		Category	1	2	3	Total
Original	Count	1	23	0	0	23
		2	0	14	0	14
		3	0	0	20	20
	%	1	100.0	.0	.0	100.0
		2	.0	100.0	.0	100.0
		3	.0	.0	100.0	100.0
Cross-validated[a]	Count	1	23	0	0	23
		2	3	11	0	14
		3	0	0	20	20
	%	1	100.0	.0	.0	100.0
		2	21.4	78.6	.0	100.0
		3	.0	.0	100.0	100.0

Figure 5.12 (c) The classification results of the three groups.

The structure matrix, shown in figure 5.12 (d), of the result proves that the sodium doublet lines, 589.593 nm and 588.995 nm, are mainly used in DF1 to discriminate bacteria from its growth medium. On the other hand, DFA has used 422.673 nm calcium line and 279.553 nm magnesium line to discriminate the two *E. coli*. This confirms the presence of Mg^{2+} and Ca^{2+} divalent cations in the outer membrane of Gram-negative bacteria.

Structure Matrix

	Function	
	1	2
P589.593	.503*	-.125
P588.995	.493*	-.208
P213.618	-.263*	.052
P285.213	-.227*	-.226
P247.856	-.223*	.057
P393.366	-.202*	-.033
P253.566	-.191*	.016
P214.914	-.190*	-.115
P396.847	-.167*	-.121
P213.546	-.117*	-.013
P315.887	-.114*	.098
P317.933	-.108*	.077
P383.231	-.084*	-.063
P255.491	-.073*	.055
P215.408	-.064*	.054
P215.294	-.039*	-.028
P422.673	-.156	-.478*
P279.553	-.101	.338*
P270.806	-.069	.313*
P280.271	-.096	.296*
P769.896[a]	.042	-.250*
P279.079	-.053	.238*
P518.361	-.068	.207*
P383.829	-.102	.175*
P277.983	-.047	.167*
P373.690	-.093	.149*
P255.326	-.115	.138*
P430.253	-.092	.135*
P203.347	-.064	.107*
P382.931	-.045	.103*
P253.398	-.067	-.073*

Figure 5.12 (d) The structure matrix of the DFA

5.2 (a) 2. With delay time = 2 µs

Figure 5.13 shows the DFA plot of the same two *E. coli* and TSA in argon, obtained at an early delay time 2 µs. An early delay time eventually picks light from less stable plasma and figure 5.3 clearly shows the instability of the plasma with a large background. As a result, the inorganic elements and their ratio seen by the spectrometer will change. But the ability of discrimination remains unchanged. Figure 5.13 (a) is very much comparable to figure 5.12 (a) taken at 4 µs delay time.

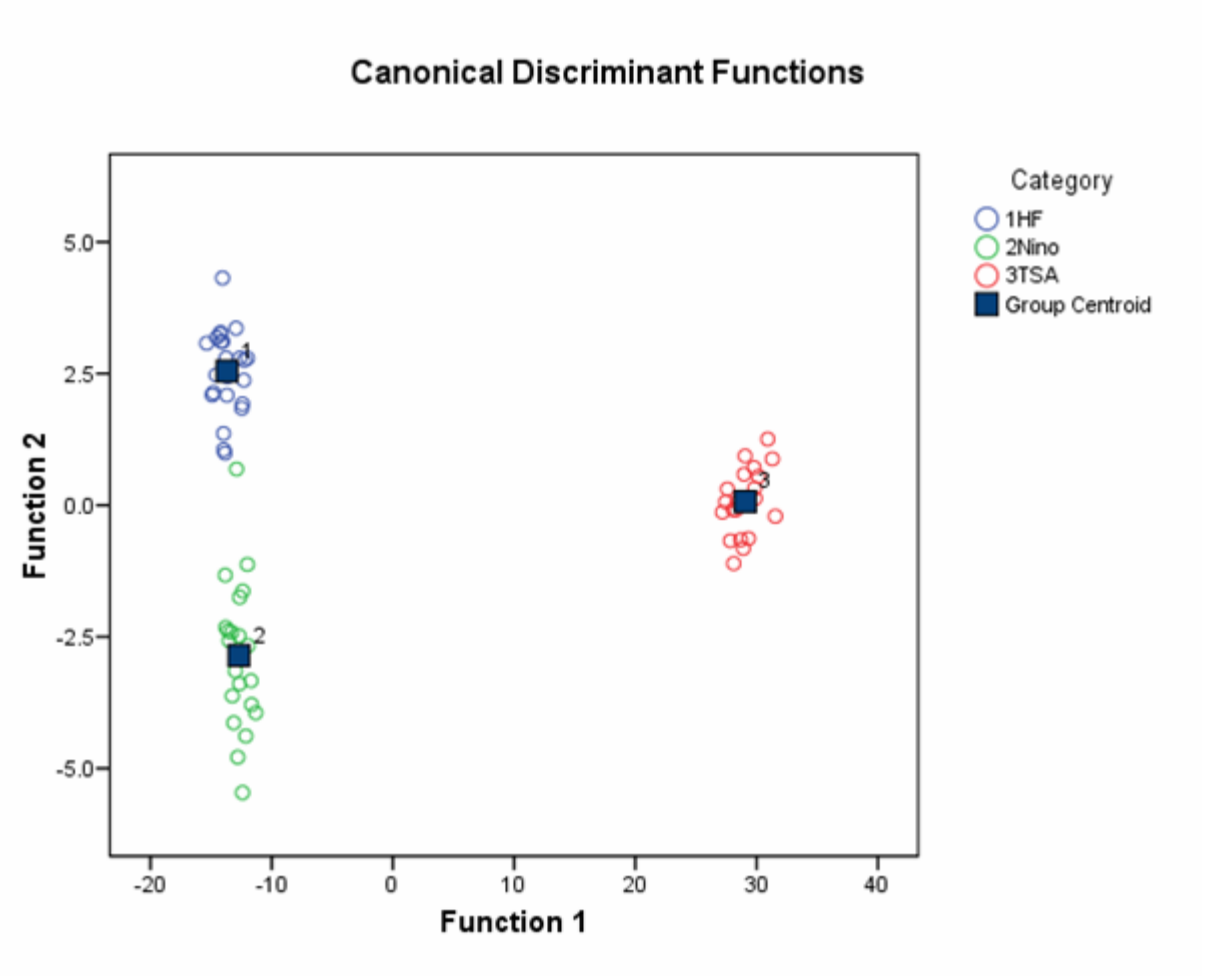

Figure 5.13 (a) The DFA plot of two *E. coli* and TSA in argon at delay time 2 µs.

Eigenvalues

Function	Eigenvalue	% of Variance	Cumulative %	Canonical Correlation
1	403.011[a]	98.7	98.7	.999
2	5.258[a]	1.3	100.0	.917

Figure 5.13 (b) The eigenvalues of the DFA, which tells that all group memberships were predicted correctly with 98.7% of the variance between groups represented by DF1 and 1.3% by DF2.

Classification Results[b,c]

			Predicted Group Membership			
		Category	1	2	3	Total
Original	Count	1	23	0	0	23
		2	1	20	0	21
		3	0	0	20	20
	%	1	100.0	.0	.0	100.0
		2	4.8	95.2	.0	100.0
		3	.0	.0	100.0	100.0
Cross-validated[a]	Count	1	20	3	0	23
		2	6	15	0	21
		3	0	0	20	20
	%	1	87.0	13.0	.0	100.0
		2	28.6	71.4	.0	100.0
		3	.0	.0	100.0	100.0

Figure 5.13 (c) The classification results which tells that the 98.4 % of original grouped cases are correctly identified and 85.9% of cross validated grouped cases are correctly identified.

The structure matrix, shown in figure 5.13 (d), of the DFA shows difference between 2 µs delay time and 4. Even though DF1 uses the same sodium lines for discrimination, DF2 makes use of 280.271 nm magnesium line and 247.856 nm carbon line to discriminate the two *E. coli.*

Structure Matrix

	Function	
	1	2
P588.995	.542*	-.263
P589.593	.435*	-.329
P213.618	-.208*	.033
P214.914	-.163*	-.049
P253.566	-.107*	-.089
P270.806	-.057*	-.015
P213.546	-.043*	-.021
P317.933	-.041*	-.029
P383.829	-.039*	-.030
P315.887	-.030*	.015
P279.079	-.028*	-.011
P280.271	-.150	.445*
P247.856	-.106	-.431*
P279.553	-.152	.425*
P393.366	-.134	.402*
P769.896[a]	-.005	-.390*
P285.213	-.142	.287*
P396.847	-.168	.260*
P422.673	-.112	-.246*
P277.983	-.028	-.179*
P255.326	-.073	-.131*
P383.231	-.025	-.099*
P430.253	-.017	-.097*
P373.690	-.025	-.077*
P255.491	-.055	-.073*
P203.347	-.036	-.069*
P382.931	-.006	-.063*
P253.398	-.050	-.062*
P518.361	-.013	-.056*
P215.408	-.038	-.050*
P215.294	-.026	-.043*

Figure 5.13 (d) The structure matrix of DFA

Figure 5.14 (a) shows the DFA plot for the two *E. coli* strains, the substrate agar and TSA growth medium taken at 2 μs delay time. All group memberships were predicted correctly 100.0% of the time, with 71.3% of variance between groups represented by DF1, 27.2% by DF2 and 0.9% by DF3. Since the contribution by DF3 is very small, it can be neglected and assumed that DF1 and DF2 wholly contribute in the analysis. DF1 is used to discriminate the bacteria and the substrate from TSA and DF2 discriminates the two *E. coli* from agar. Also in the analysis 100.0% of original grouped cases are correctly identified and 94.8% of cross validated grouped cases are correctly identified as shown in figure 5.14 (b).

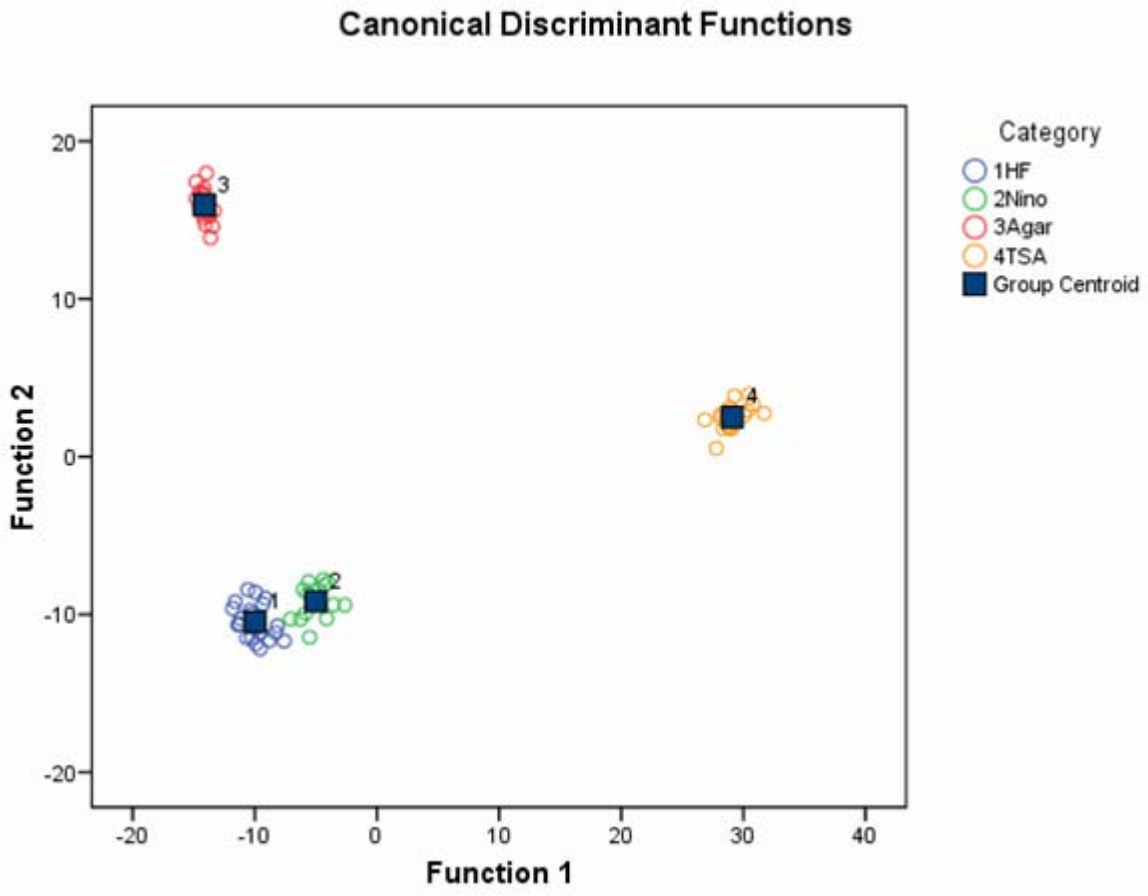

Figure 5.14 (a) The discriminant function scores of two *E. coli* strains, Nino C and HF4714, the substrate agar and TSA on which they were grown.

Classification Results[b,c]

			Predicted Group Membership				
		Category	1	2	3	4	Total
Original	Count	1	23	0	0	0	23
		2	0	14	0	0	14
		3	0	0	20	0	20
		4	0	0	0	20	20
	%	1	100.0	.0	.0	.0	100.0
		2	.0	100.0	.0	.0	100.0
		3	.0	.0	100.0	.0	100.0
		4	.0	.0	.0	100.0	100.0
Cross-validated[a]	Count	1	23	0	0	0	23
		2	1	13	0	0	14
		3	1	2	17	0	20
		4	0	0	0	20	20
	%	1	100.0	.0	.0	.0	100.0
		2	7.1	92.9	.0	.0	100.0
		3	5.0	10.0	85.0	.0	100.0
		4	.0	.0	.0	100.0	100.0

Figure 5.14 (b) The classification results of discriminant function analysis.

In the DFA plot, the two *E. coli* strains show similar classification, while the agar and TSA show a greater discrimination compared to figure 5.13 (a). The structure matrix shown in figure 5.14 (c) tells that DF1 utilizes sodium lines to discriminate bacteria and agar from TSA as it is rich in sodium and DF2 uses 213.618 nm phosphorous line and 285.213 nm magnesium line to discriminate two *E. coli* from agar, since agar has almost no inorganic element.

Structure Matrix

	Function		
	1	2	3
P588.995	.483*	.174	-.126
P589.593	.298*	.113	-.006
P396.847	-.078*	-.027	-.063
P213.546	-.022*	.019	.016
P213.618	-.061	-.149*	.036
P285.213	-.046	-.101*	-.078
P382.931	-.030	.085*	.021
P383.231	-.033	.081*	.031
P215.408	-.034	.079*	.015
P255.491	-.033	.075*	.021
P373.690	-.027	.068*	.011
P214.914	-.051	-.065*	.058
P203.347	-.028	.063*	.020
P277.983	-.024	.059*	.035
P518.361	-.022	.056*	.020
P215.294	-.024	.056*	.013
P383.829	-.028	.055*	.013
P253.398	-.024	.047*	.006
P430.253	-.020	.046*	.027
P270.806	-.027	.044*	.019
P279.079	-.023	.043*	.015
P317.933	-.024	.032*	.024
P315.887	-.025	.032*	.017
P247.856	-.079	-.083	.541*
P279.553	-.105	-.252	-.381*
P280.271	-.093	-.186	-.362*
P393.366	-.102	-.072	-.265*
P769.896[a]	-.005	.013	.211*
P422.673	-.051	.034	.126*
P255.326	-.030	.016	.063*
P253.566	-.031	-.018	.050*

Figure 5.14 (c) The structure matrix of the discrimination of two *E. coli* strains, the substrate agar and TSA on which they were grown.

5.2 (b) Helium results

In helium, we managed to obtain a spectrum at 1 microsecond delay time. Figure 5.14 (a) shows a DFA plot of the two same *E. coli* and TSA in helium. The DFA correctly identified the group membership of Nino C, HF and TSA spectra 100% of time, with 86.2% of variance between groups represented by DF1 and 13.8% by DF2. As mentioned above 100% of original grouped cases were correctly identified in addition, 90.2% cross validated grouped cases were correctly classified.

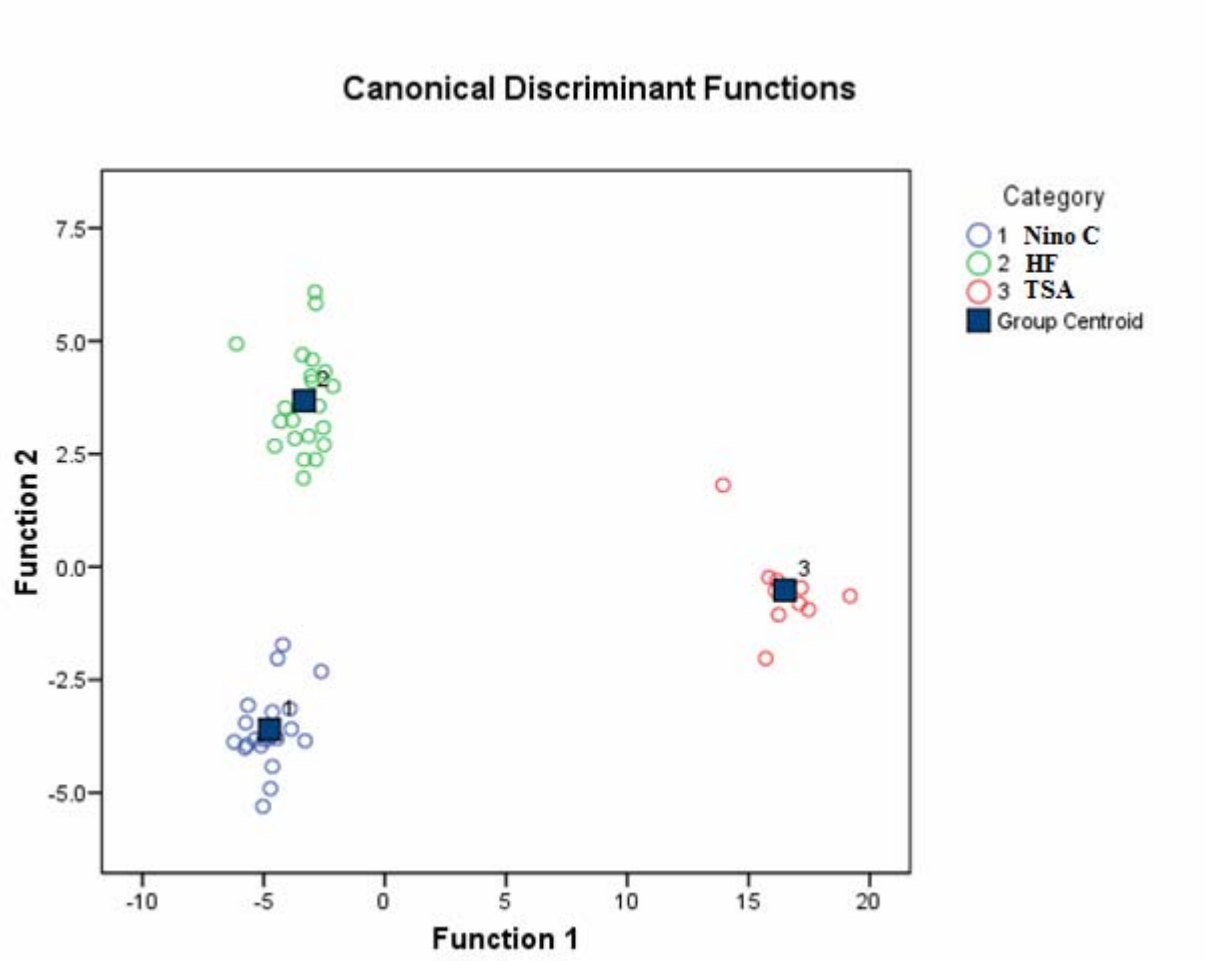

Figure 5.15 (a) The discriminant function scores of two *E. coli* strains and the growth medium TSA in helium at 1 μs.

Figure 5.15 (b) shows the structure matrix of the above DFA result. As expected, 589.593 nm and 588.995 nm sodium doublet lines are used for the discrimination in DF1. In helium DF2 makes use of 393.366 nm calcium line and 279.553 nm magnesium line to discriminate the two *E. coli.*

Structure Matrix

	Function	
	1	2
P589.593	.616*	-.205
P588.995	.457*	-.141
P285.213	-.181*	.023
P247.856	-.131*	.012
P317.933	-.108*	-.091
P315.887	-.091*	.029
P270.806	-.080*	.026
P255.491	-.078*	-.053
P279.079	-.063*	-.036
P277.983	-.057*	-.019
P215.294	-.041*	-.035
P430.253	-.036*	-.035
P393.366	-.176	.404*
P279.553	-.113	.314*
P280.271	-.120	.314*
P214.914	-.217	-.241*
P396.847	-.139	.238*
P422.673	-.163	.217*
P213.618	-.200	-.205*
P383.231	-.091	-.204*
P255.326	-.109	-.171*
P253.566	-.162	-.169*
P383.829	-.092	-.121*
P215.408	-.062	-.107*
P373.690	-.064	.098*
P203.347	-.051	-.090*
P518.361	-.054	-.084*
P213.546	-.034	-.083*
P253.398	-.059	-.068*
P769.896[a]	.044	-.046*
P382.931	-.027	-.036*

Figure 5.15 (b) The structure matrix of the DFA of two *E. coli*, Nino C and HF 4714, in helium

5.3 The reproducibility of the experiment

The ultimate goal of the experiments was to prove the reproducibility of the technique. In order to make the data identical, we started with three plates of Nino C and three plates of HF 4714, both grown on TSA and cultured on the same day. An agar plate was divided into three sections and the first Nino C sample was transferred to one of these three sections. A set of data was obtained in argon and then the second sample of Nino C was transferred to the same agar plate but in a different section to avoid contamination. A second set of data was acquired again in argon and finally the third sample was transferred on to the agar plate and the third argon data sets were collected. In this way, three independent measurements of different, yet nominally identical, Nino C were all measured on the same agar substrate in a relatively short period of time. Similarly three sets of HF 4714 data in argon were obtained. The same procedure was repeated in helium environment. After all bacteria were analyzed, slices of the TSA growth medium were removed from the sample Petri dishes, placed on the agar sample plates, and analyzed in both gases.

5.3 (a) In Helium

Figure 5.16 (a) shows a DFA plot of three HF 4714 groups, three Nino C groups and TSA in helium with delay time 1 microsecond. In the plot, the three groups belong to both *E. coli* were well separated (as circled). Within the groups they showed small deviations which could be due to lack constancy in the height introduced by the evaporation of water from agar due to its exposure for a long time.

The DFA correctly identified the group memberships 100% of time, with 93.8% of variance between groups represented by DF1, 3.8% by DF2, 1.3% by DF3 and less than 1% by

other three discriminant functions. Also 97.5% of original grouped cases were correctly identified in addition, 66.3% cross validated grouped cases were correctly classified.

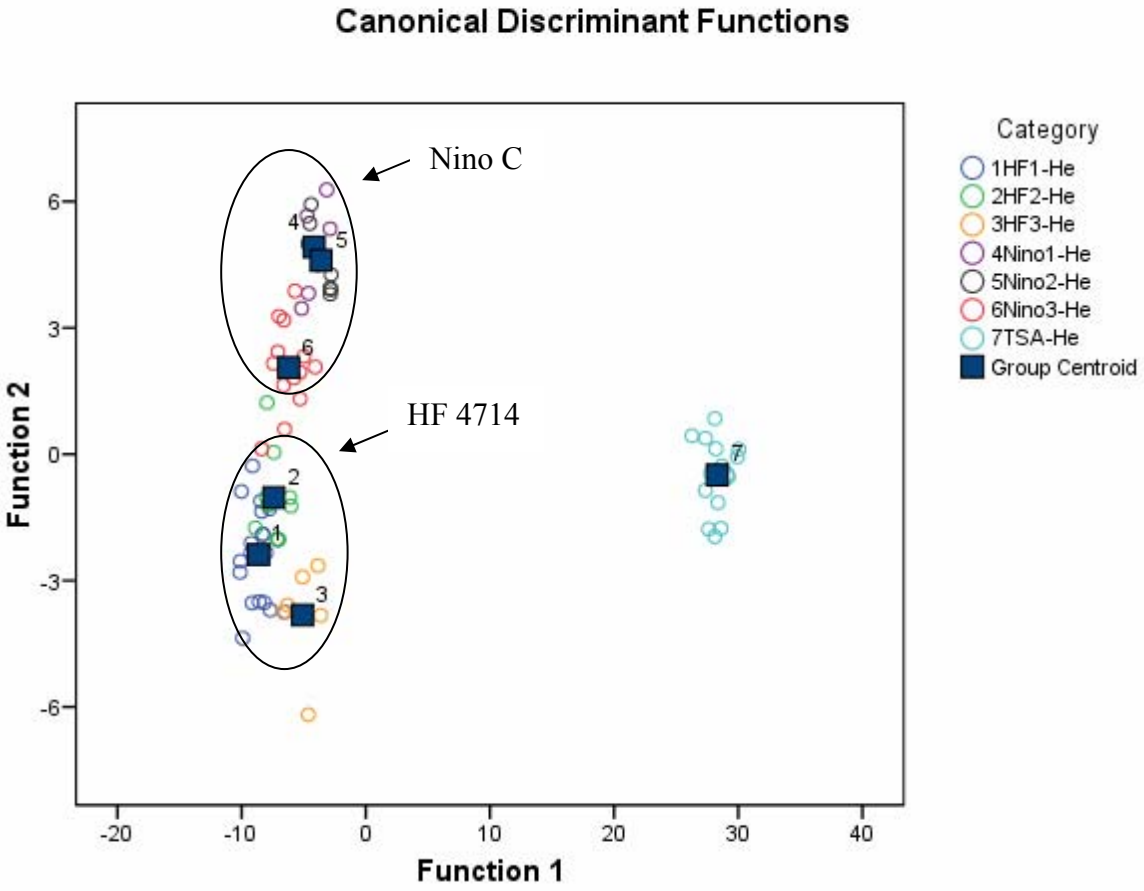

(a)

Classification Results[b,c]

		Category	Predicted Group Membership							Total
			1	2	3	4	5	6	7	
Original	Count	1	20	0	0	0	0	0	0	20
		2	1	10	0	0	0	0	0	11
		3	0	0	7	0	0	0	0	7
		4	0	0	0	6	0	0	0	6
		5	0	0	0	0	8	0	0	8
		6	1	0	0	0	0	12	0	13
		7	0	0	0	0	0	0	15	15
	%	1	100.0	.0	.0	.0	.0	.0	.0	100.0
		2	9.1	90.9	.0	.0	.0	.0	.0	100.0
		3	.0	.0	100.0	.0	.0	.0	.0	100.0
		4	.0	.0	.0	100.0	.0	.0	.0	100.0
		5	.0	.0	.0	.0	100.0	.0	.0	100.0
		6	7.7	.0	.0	.0	.0	92.3	.0	100.0
		7	.0	.0	.0	.0	.0	.0	100.0	100.0
Cross-validated[a]	Count	1	14	5	0	0	0	1	0	20
		2	3	6	0	0	0	2	0	11
		3	0	2	5	0	0	0	0	7
		4	0	0	0	0	4	2	0	6
		5	0	0	0	3	5	0	0	8
		6	1	1	0	1	2	8	0	13
		7	0	0	0	0	0	0	15	15
	%	1	70.0	25.0	.0	.0	.0	5.0	.0	100.0
		2	27.3	54.5	.0	.0	.0	18.2	.0	100.0
		3	.0	28.6	71.4	.0	.0	.0	.0	100.0
		4	.0	.0	.0	.0	66.7	33.3	.0	100.0
		5	.0	.0	.0	37.5	62.5	.0	.0	100.0
		6	7.7	7.7	.0	7.7	15.4	61.5	.0	100.0
		7	.0	.0	.0	.0	.0	.0	100.0	100.0

(b)

Figure 5.16 (a) The discriminant function scores of three HF 4714 and three Nino C groups in helium (b) The classification results of the DFA.

Then we combined the three groups of both *E. coli,* and analyzed the data. Figure 5.17(a) illustrates the DFA plot of groups in figure 5.16(a) combined. The plot was quite similar to figure 5.15(a).

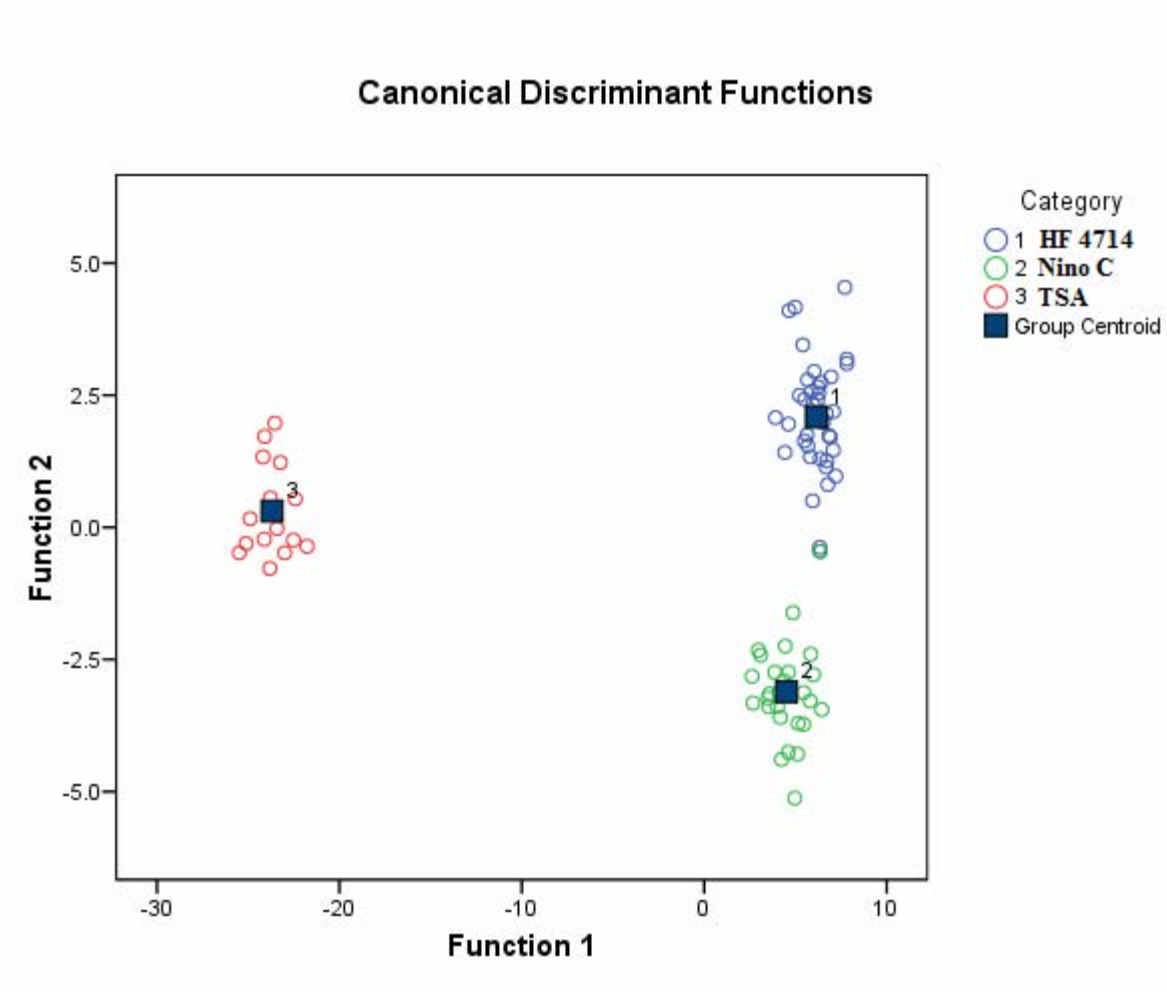

(a)

Eigenvalues

Function	Eigenvalue	% of Variance	Cumulative %	Canonical Correlation
1	135.129[a]	96.0	96.0	.996
2	5.566[a]	4.0	100.0	.921

a. First 2 canonical discriminant functions were used in the analysis.

(b)

Structure Matrix

	Function	
	1	2
P589.593	-.603*	-.133
P588.995	-.551*	-.139
P285.213	.296*	.077
P213.618	.214*	-.197
P214.914	.213*	-.202
P279.553	.213*	-.128
P253.566	.178*	-.147
P280.271	.167*	-.032
P383.829	.103*	-.015
P253.398	.087*	-.054
P213.546	.082*	-.077
P279.079	.081*	.051
P270.806	.079*	.063
P373.690	.075*	.061
P383.231	.075*	.019
P382.931	.044*	.005
P422.673	.247	.396*
P315.887	.117	.346*
P396.847	.197	.271*
P393.366	.210	.247*
P317.933	.105	.221*
P255.326	.141	-.207*
P255.491	.089	-.199*
P518.361	.088	.170*
P247.856	.134	.165*
P769.896[a]	-.091	-.163*
P430.253	.078	.157*
P215.408	.082	-.136*
P277.983	.023	.092*
P203.347	.044	-.067*
P215.294	.044	-.056*

(c)

Figure 5.17 (a) The DFA plot of the three groups of both *E. coli* strains combined. It shows a quiet similar pattern of discrimination to figure 5.15(a) (b) The eigenvalues of the DFA. The DFA correctly identified the group memberships 100% of time, with 96.0% of variance between groups represented by DF1, and 4.0% by DF2 (c) The structure matrix of DFA. DF1 uses sodium doublet lines to discriminate the bacteria from TSA and DF2 makes use of calcium lines for discrimination.

5.3 (b) In Argon

The experiment in argon was done at 2 microsecond delay time. Figure 5.18 (a) shows the DFA plot of three HF 4714 groups, three Nino C groups and TSA in argon. In the plot, Nino3 and HF3 look different from their group so we removed them and the resultant plot is shown in figure 5.18(b), where HF and Nino C group together quite well (as circled). The DFA correctly identified the group memberships 100% of time, with 97.1% of variance between groups represented by DF1, 2.4% by DF2, 0.4% by DF3 and 0.2% by DF4. Also 98.4% of original grouped cases were correctly identified in addition, 71.9% cross validated grouped cases were correctly classified.

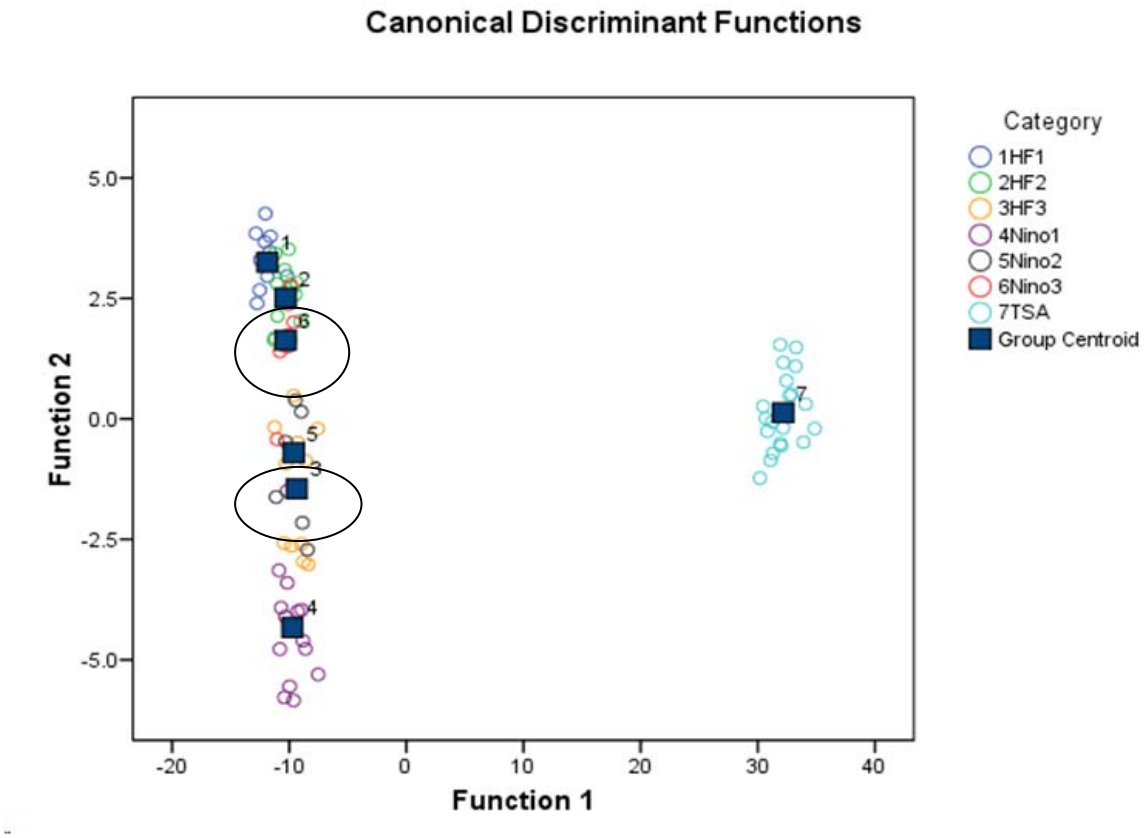

(a)

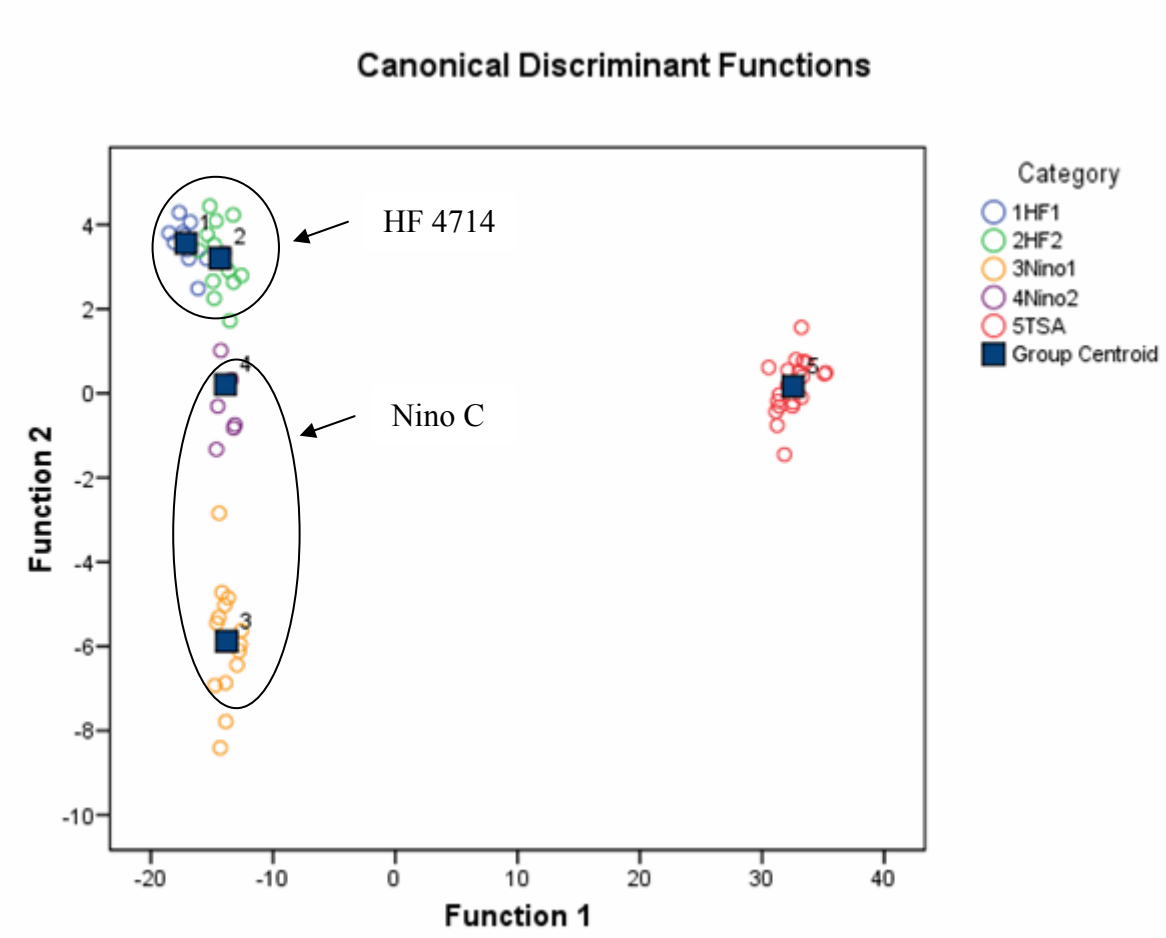

(b)

The structure matrix of both figures 5.18 (a) and (b) are very much comparable with 5.13 (d). The two sodium doublet lines dominate DF1, whereas DF2 uses the 247.856 nm carbon line and 280.271 nm magnesium line.

Structure Matrix

	Function			
	1	2	3	4
P588.995	.482*	-.128	-.152	.337
P589.593	.387*	-.171	-.030	.332
P213.618	-.188*	.029	.084	.099
P214.914	-.144*	-.030	.098	.064
P247.856	-.110	-.389*	.083	-.087
P280.271	-.155	.364*	.117	-.178
P769.896[a]	-.004	-.334*	.038	-.055
P279.553	-.145	.302*	.008	-.188
P277.983	-.025	-.132*	.005	.034
P203.347	-.031	-.048*	.011	.042
P285.213	-.134	.167	-.276*	-.069
P270.806	-.053	-.034	-.183*	.067
P215.408	-.033	-.022	.148*	-.011
P315.887	-.027	-.011	-.078*	-.074
P383.829	-.035	-.011	.076*	.035
P215.294	-.022	-.026	.068*	-.011
P382.931	-.005	-.049	-.068*	.064
P279.079	-.024	-.017	-.065*	.018
P253.398	-.047	.010	.166	.353*
P393.366	-.125	.275	.055	-.286*
P396.847	-.150	.157	.071	-.273*
P422.673	-.116	-.228	-.224	.233*
P255.326	-.067	-.102	-.114	.185*
P373.690	-.022	-.018	.162	.171*
P430.253	-.015	-.052	.046	.132*
P253.566	-.095	-.059	.024	.112*
P383.231	-.022	-.061	.021	.098*
P213.546	-.038	-.010	-.012	.096*
P255.491	-.049	-.056	-.052	.089*
P518.361	-.011	-.051	.011	-.080*
P317.933	-.036	-.030	-.005	-.043*

(c)

Figure 5.18 (a) The discriminant function scores of three HF 4714 and three Nino C groups in argon (b) The DFA plot of the three groups of both *E. coli* after removing HF3 and Nino3 from (a) (c) The structure matrix of DFA.

Then those two groups of each *E. coli* were grouped together. Figure 5.19(a) illustrates the resultant plot of combining those data.

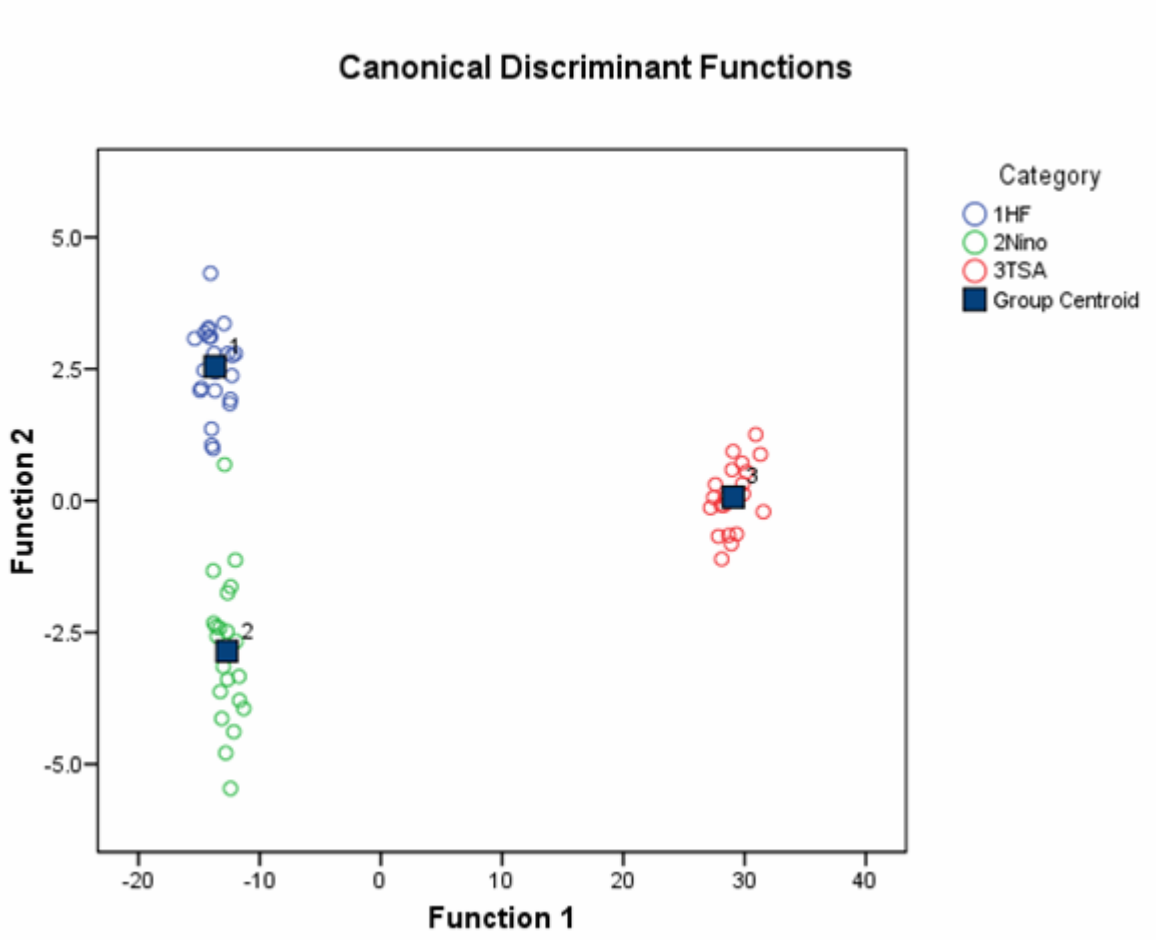

(a)

Classification Results[b,c]

			Predicted Group Membership			
		Category	1	2	3	Total
Original	Count	1	23	0	0	23
		2	1	20	0	21
		3	0	0	20	20
	%	1	100.0	.0	.0	100.0
		2	4.8	95.2	.0	100.0
		3	.0	.0	100.0	100.0
Cross-validated[a]	Count	1	20	3	0	23
		2	6	15	0	21
		3	0	0	20	20
	%	1	87.0	13.0	.0	100.0
		2	28.6	71.4	.0	100.0
		3	.0	.0	100.0	100.0

(b)

Structure Matrix

	Function	
	1	2
P588.995	.542*	-.263
P589.593	.435*	-.329
P213.618	-.208*	.033
P214.914	-.163*	-.049
P253.566	-.107*	-.089
P270.806	-.057*	-.015
P213.546	-.043*	-.021
P317.933	-.041*	-.029
P383.829	-.039*	-.030
P315.887	-.030*	.015
P279.079	-.028*	-.011
P280.271	-.150	.445*
P247.856	-.106	-.431*
P279.553	-.152	.425*
P393.366	-.134	.402*
P769.896[a]	-.005	-.390*
P285.213	-.142	.287*
P396.847	-.168	.260*
P422.673	-.112	-.246*
P277.983	-.028	-.179*
P255.326	-.073	-.131*
P383.231	-.025	-.099*
P430.253	-.017	-.097*
P373.690	-.025	-.077*
P255.491	-.055	-.073*
P203.347	-.036	-.069*
P382.931	-.006	-.063*
P253.398	-.050	-.062*
P518.361	-.013	-.056*
P215.408	-.038	-.050*
P215.294	-.026	-.043*

(c)

Figure 5.19 (a) The DFA plot of the two groups of both *E. coli* combined. It shows much similar pattern of discrimination to figure 5.13(a) (b) The classification results of DFA. 98.4% of the original grouped cases are correctly identified. Also 85.9% of cross validated grouped cases are correctly classified. (c) The structure matrix of DFA. DF1 uses sodium doublet lines to discriminate the bacteria from TSA and DF2 makes use of calcium lines for discrimination.

5.4 Helium and argon results combined

Next we tried combining the results obtained by argon and helium together. The two 31 line spectra obtained from argon and helium were combined to create a 62 element spectral fingerprint for DFA. Figure 5.20 (a) shows the DFA plot of the combination of argon results (τ_d = 4 μs) shown in figure 5.12 (a) and helium results (τ_d = 1μs) shown in 5.14 (a). The discrimination in DF1 is two times larger and DF2 discrimination is six times larger than the individual plots. Also it gives less scattered and more focused discrimination.

The DFA correctly identified the group memberships 100% of the time, with 83.5% of variance between groups represented by DF1, and 16.5% by DF2. Also 100.0% of original grouped cases were correctly identified in addition, 71.7% cross validated grouped cases were correctly classified.

(a)

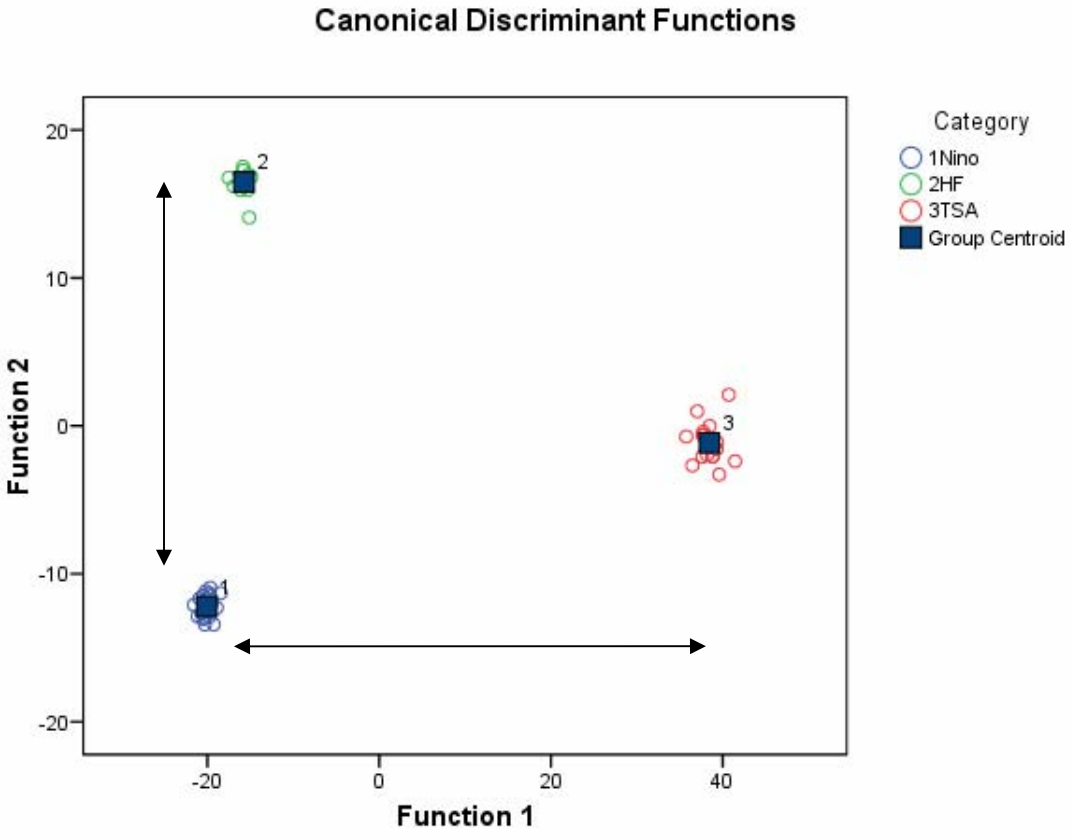

Structure Matrix

	Function	
	1	2
He588.995	.259*	-.055
Ar373.690 [a]	.158*	-.060
He589.593	.136*	-.041
Ar422.673 [a]	.129*	.111
Ar279.079 [a]	.127*	.068
Ar588.995 [a]	.119*	-.088
He285.213	-.089*	.044
Ar213.618	-.088*	-.011
He213.618	-.087*	-.005
He214.914	-.081*	.010
Ar247.856	-.068*	-.013
He393.366	-.063*	.053
Ar285.213	-.063*	.014
He253.566	-.062*	-.019
He279.553	-.057*	.016
Ar214.914	-.055*	.003
Ar253.566	-.054*	.008
He396.847	-.050*	.030
He280.271	-.049*	-.012
He422.673	-.048*	.037
Ar383.231 [a]	-.046*	.016
He247.856	-.044*	.008
He253.398	-.043*	-.002
He383.829	-.040*	.001
He255.491	-.040*	-.028
He255.326	-.038*	.009
He270.806	-.038*	-.011
Ar255.326	-.037*	-.027
Ar213.546	-.036*	.001
Ar317.933	-.031*	.000
Ar430.253	-.028*	-.020
He383.231	-.027*	-.007
Ar253.398	-.023*	.009
Ar255.491	-.022*	-.011
He430.253	-.022*	.019
He279.079	-.021*	.005
Ar215.408	-.018*	-.010
He215.408	-.018*	.013
Ar215.294	-.015*	.007
He518.361	-.011*	.010
He277.983	-.010*	.007
Ar383.829 [a]	-.087	.181*
Ar382.931 [a]	.124	.176*
Ar315.887 [a]	.028	-.143*
Ar589.593 [a]	.116	.116*
Ar518.361 [a]	-.046	-.088*
Ar769.896 [a]	-.022	.083*
Ar280.271 [a]	-.027	-.062*
Ar393.366 [a]	-.027	.058*
Ar279.553	-.027	-.041*
He373.690	-.017	.038*
Ar270.806	-.021	-.035*
He317.933	-.029	.032*
Ar277.983	-.015	-.030*
Ar396.847 [a]	-.001	.028*
He382.931	-.010	.026*
He215.294	-.016	-.025*
He315.887	-.019	.025*
Ar203.347	-.020	-.021*
He213.546	-.019	.020*
He203.347	-.001	-.018*
He769.896 [a]	.002	.010*

Pooled within-groups correlations between discriminating variables and standardized canonical discriminant functions
Variables ordered by absolute size of correlation within function.

*. Largest absolute correlation between each variable and any discriminant function

a. This variable not used in the analysis.

(b)

Figure 5.20 (a) The DFA plot of Nino C, HF 4714 and TSA obtained by combining helium results and argon results. (b) The structure matrix of the plot.

Chapter 6

Conclusion

Nanosecond laser-induced breakdown spectroscopy has been used to identify and discriminate between two non-pathogenic strains of the *E. coli* bacteria called Nino C and HF4714. One of the most important questions surrounding the practical application of LIBS as a diagnostic tool for identification and discrimination of bacterial strains is the reproducibility of the measurements and the specificity of the measurements. In this work, we have examined the effect that ablating *E. coli* in a noble gas (argon or helium) environment had on the LIBS spectra, on our subsequent ability to classify or identify these bacteria based on those spectra, and on the reproducibly of the measurements. Noble gases were demonstrated to produce a higher plasma temperature, a higher electron density and, despite the lower mass ablation rate, a higher emission intensity for the chosen monitored element under fixed experimental conditions.

A discriminant function analysis was used to analyze the LIBS spectra from bacteria colonies grown on TSA plates. The DFA clearly showed discrimination between the common environmental strain of *E. coli* (Nino C) and the laboratory strain of *E. coli* (HF4714) in both argon and helium environments. The addition of TSA and agar spectra to the discrimination analysis showed that they were immediately differentiable from both *E. coli* samples. In argon, we tried two delay times, 2 μs and 4 μs. While providing an overall increase in absolute intensity, the DFA of the 2 μs measurements revealed an influence on the discrimination due to the carbon 247.856 nm emission line that is not preferred.

One of the goals of this work was to prove the reproducibility of the technique in different gas environments. In order to test that reproducibility, three independent measurements of different, yet nominally identical, Nino C were obtained from the same agar substrate in a

relatively short period of time. A similar procedure was followed with HF4714. The results obtained in helium showed a more consistent and promising ability to create highly reproducible spectra than in argon. One possible explanation for this could be that maintaining the exact experimental conditions each and every time is much more crucial when argon is used, compared to helium. Due to the lack of constancy in the height introduced by the evaporation of water from agar due to its exposure to noble gas (dry gas) for a long time, it becomes a challenge, especially in argon, to maintain the precise focusing and ablation conditions.

The rate of the absorption of water from the sample or the atmosphere by a gas, which has no water in it (a dry gas), is very high. In order to avoid that, the apparatus set up should be modified as shown in figure 6.1. In the figure, the noble gas is first sent through a tube into a conical flask, which is tightly sealed with a cork, and the end of the tube is attached to a gas dispersion tube. The gas dispersion tube is useful when gas must be introduced into a container with narrow opening. Then the gas combined with moisture is collected and flushed into the purge chamber using another tube. In this way, the moisture inside the chamber will be maintained constant throughout the experiment.

Finally, we combined the results obtained in both helium and argon together and the resultant DFA plot showed a much clearer discrimination not only between the substrate and the sample but also between bacteria. It is puzzling however, how the overall ability to predict the identity of the bacteria using the “leave one out” routine actually decreased due to the combination of these spectra. This result will need to be studied in future work if the “dual-gas” technique is to be seriously considered for practical applications.

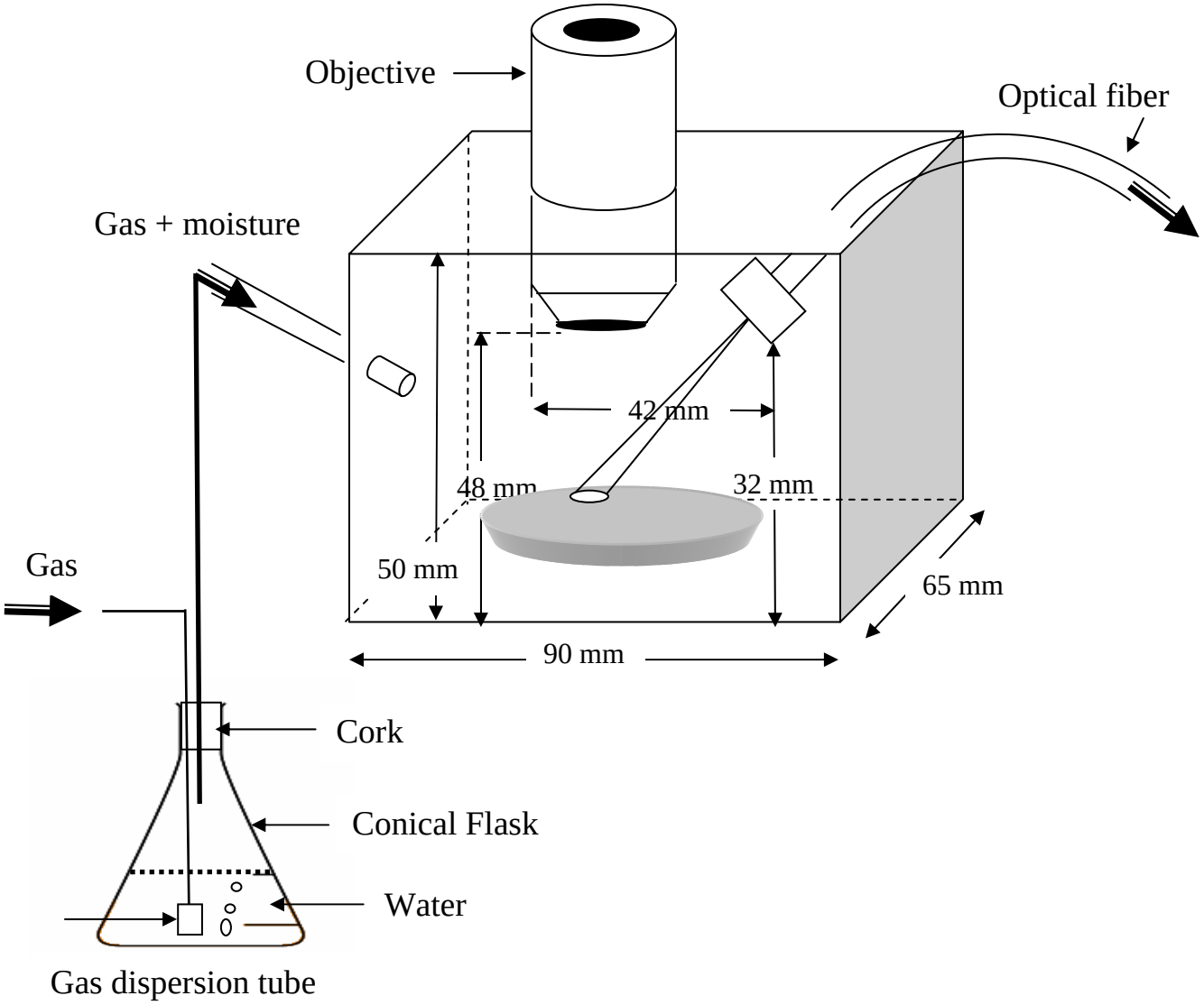

Figure 6.1 The modified apparatus set-up. The gas is sent through water so that the gas flushed into the purge chamber will contain moisture as a result the evaporation of water from agar will greatly reduce.

From this work, it is very clear that the environmental gases play an important role in LIBS analysis of bacteria. They determine the ratio of elements picked up from the plasma; therefore, it is worth to investigate reproducibility in vacuum, which would entirely eliminate the influence of environmental gases in the signal. Furthermore, an experiment should be designed to explore the correlation of the ability of discrimination with the amount of time a bacterial colony sits on the nutrient medium prior to LIBS analysis. Why would this be necessary? First, the strains of bacteria may be more or less prone to changes in biochemistry depending upon the medium in which they are grown. Second, the bacteria form a biofilm in order to survive in natural environments. A biofilm can develop on a static surface (in a static phase the bacteria will be alive but cannot grow) and generally consists of bacterial cells entwined in a protective matrix of extracellular polysaccharides. This biofilm could have a significant impact on the observed LIBS spectra and would be a time-dependent phenomenon. Because of these two reasons, it will be very important to investigate this time dependence.

Appendix

The Macro

To quickly and conveniently analyze the data, we needed a fairly automated way to obtain the 31 emission peak areas from each spectrum obtained in the ROI view. To analyze this data, each spectrum file (of type ".spe") was converted to text-formatted ".dat" file. In order to extract only the peak area from the ".dat" files, an MS Excel macro was written. The excel sheet shown below was created to input the required data to run the macro. Ones the "execute" button clicked, the macro selects the area under the peak, corresponding to each emission line from each data file, creates a new excel worksheet and pastes just the areas into this sheet. In other words, first the macro opens a data file and collects the values in C11, C13, C15,……,C71. Then it creates a new excel book called "Final_data.xls" and saves these numbers in a row. It then repeats the same procedure to the arbitrary number of data files in a particular folder (and there could be around 100 files generated per day) and saves all the data in "Final_data.xls".

In the excel sheet shown below, first enter the directory path or the path to reach the folder, which contains the ".dat" files to be executed. A back slash "\" should be included at the end of the path name. Next the root name of the files must be given. We maintained a pattern while saving the data during data taking process. For example, 091107_001. Here the root name is 091107, the date, the experiment was done. Finally, the total number of files must be inserted before click on "execute".

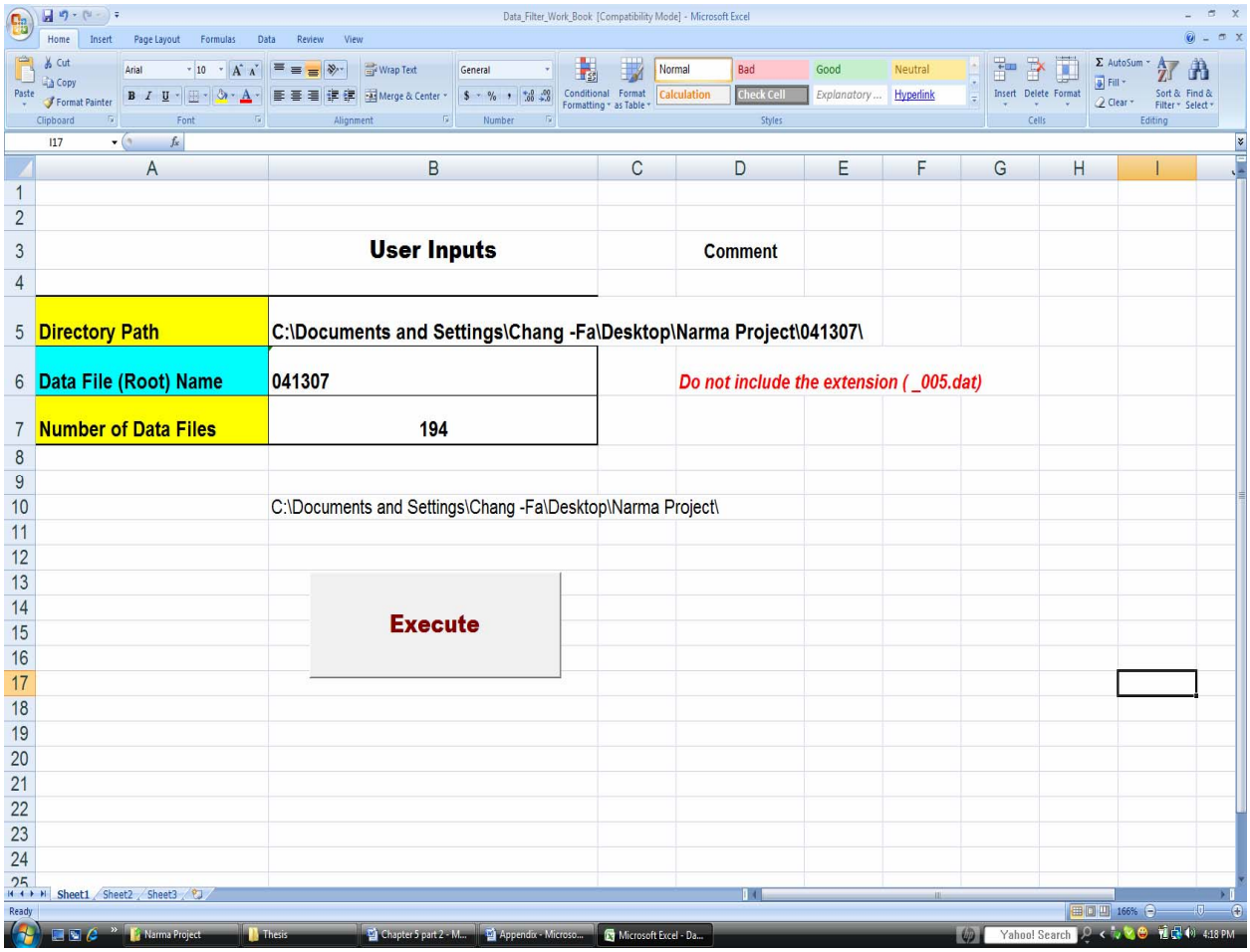

Visual basic coding

```
Sub Data_Filter_Main()
'
' Macro created by Jeynarma
'

 Dim Dir_path, File_name, N_row, icol, N_Row_max, DatFile

'o-------------------------------------------------------------------------------------------o
'|                    User Inputs                                                            |
'o-------------------------------------------------------------------------------------------o

' Dir_path = "H:\Jeynarma\2007\Excel\"            ' User Input
' File_name = "032607"                    ' User Input
' numDatFile = 20                        ' User Input   (Number of Total Data Files)
'o-------------------------------------------------------------------------------------------o
```

```
 Dir_path = Range("B5").Value              ' User Input
 File_name = Range("B6").Value             ' User Input
 numDatFile = Range("B7").Value            ' User Input   (Number of Total Data
Files)

   ChDir _
      Dir_path

   Workbooks.Add
   Sheets("Sheet1").Name = "Sorted Data"
   ActiveWorkbook.SaveAs Filename:= _
      Dir_path & "Final_Data.xls" _
      , FileFormat:=xlNormal, Password:="", WriteResPassword:="", _
      ReadOnlyRecommended:=False, CreateBackup:=False

 Dim Number As Integer

   Number = 1

  Do While Number <= numDatFile

    If Number < 10 Then
      DatFile = File_name & "_00" & Number & ".dat"
    ElseIf Number < 100 Then
      DatFile = File_name & "_0" & Number & ".dat"
    ElseIf Number < 1000 Then
      DatFile = File_name & "_" & Number & ".dat"
    End If

 'MsgBox " File Name " & DatFile
 'MsgBox "Dir " & Dir_path
     Call Data_file_open(Number, DatFile, File_name, Dir_path)

     Number = Number + 1
  Loop

   Windows("Final_Data.xls").Activate
   Sheets("Sheet2").Select
   Cells.Select
   Selection.Copy
   Sheets("Sorted Data").Select
   Selection.PasteSpecial Paste:=xlPasteValues, Operation:=xlNone, SkipBlanks
_
       :=False, Transpose:=False
```

```
    Sheets("Sheet2").Select
    Cells.Select
    Selection.ClearContents
    Sheets("Sorted Data").Select
    Range("A1").Select

    ActiveWorkbook.Save


MsgBox " Copying completed! "

End Sub

Sub Data_file_open(DatFileNumber, DatFile, File_name, Dir_path)
'
' Macro_file_open Macro

 Dim N_row, icol, N_Row_max, Number As Integer

     Workbooks.OpenText Filename:= _
        Dir_path & DatFile _
       , Origin:=xlWindows, StartRow:=1, DataType:=xlDelimited, TextQualifier _
       :=xlDoubleQuote, ConsecutiveDelimiter:=False, Tab:=True, Semicolon:= _
       False, Comma:=False, Space:=False, Other:=False, FieldInfo:=Array(1, 1)

   ' Workbooks.OpenText Filename:=Dir_path & DatFile, Origin:= _
     '   932, StartRow:=1, DataType:=xlDelimited, TextQualifier:=xlDoubleQuote,
_
      '  ConsecutiveDelimiter:=False, Tab:=True, Semicolon:=False,
Comma:=False _
      '  , Space:=False, Other:=False, FieldInfo:=Array(1, 1), _
      '  TrailingMinusNumbers:=True

 ' Cells.Select

    Range("A1").Select
    Range(Selection, Selection.End(xlDown)).Select
    N_Row_max = Selection.Rows.Count                    ' Count the max number of
rows in the dat file

 ' MsgBox " Last Row number " & N_Row_max

    Number = 1
 Do While Number <= N_Row_max

   Call Cell_Copying(DatFileNumber, N_Row_max, DatFile)
```

```
    Number = Number + 1
Loop

   Windows(DatFile).Activate
   ActiveWindow.Close

End Sub

Sub Cell_Copying(DatFileNumber, N_Row_max, DatFile)
   Windows("Final_Data.xls").Activate
   Sheets("Sheet2").Select

   icol = 1
   N_row = 11
Do While N_row < N_Row_max
   Cells(DatFileNumber, icol).Value = "='" & DatFile & "'!R" & N_row & "C3"
   icol = icol + 1
   N_row = N_row + 2
Loop

'    ActiveCell.FormulaR1C1 = "='" & File_name & "'!R11C3"

End Sub
```

References

[1] Michael T. Madigan, John M. Martinko and Jack Parker, *Brock Biology of Microorganisms*, 9th ed. (Prentice Hall, Upper Saddle River, NJ 07458, 2000).

[2] Gabriel Bitton, *Wastewater Microbiology*, 3rd ed. (Wiley series in Ecological and Applied Microbiology, Ralph Mitchell, 2005)

[3] Richard A. Harvey, Pamela C. Champe and Bruce D. Fisher, *Microbiology-Lippincott's Illustrated Reviews*, 2nd ed. (Lippincott Williams & Wilkins, 2006).

[4] Scott Snyder, Dennis Kim and Thomas J. McIntosh, "Lipopolysaccharide Bilayer structure: Effect of chemotype, Core mutations, Divalent cations, and Temperature", Biochemistry **38**, 10758-10767 (1999).

[5] Roberto D. Lins and T. P. Straatsma, "Computer simulation of the rough lipopolysaccharide membrane of Pseudomonas aeruginosa", Biophys. J. **81**, 1037-1046 (2001).

[6] Hiroshi Nikaido and Marti Vaara, "Molocular basis of bacterial outer membrane permeability", Microbiol. Rev. **49**, 1–32 (1985).

[7] Sven O Hagge, Malte U Hammer, Andre Wiese, Ulrich Seydel and Thomas Gutsmann, "Calcium adsorption and displacement: characterization of lipid monopolymers and their interaction with membrane-active peptides/proteins", BMC Biochem. **7**, **(**2006).

[8] D. A. Pink, L. Truelstrup Hansen, T. A. Gill, B. E. Quinn, M. H. Jericho, and T. J. Beveridge, "Divalent calcium ions inhibit the penetration of protamine through the polysaccharide brush of the outer membrane of gram-negative bacteria", Langmuir **19**, 8852-8858 (2003).

[9] Kathleen Park Talaro, *Foundations in Microbiology*, 5th ed. (McGraw-Hill, 2005).

[10] Edited by Andrzej W. Miziolek, Vincenzo Palleschi and Israel Schechter, *Laser-Induced Breakdown Spectroscopy – Fundamentals and Applications,* (Cambridge University Press, 2006).

[11] David A. Cremers and Leon J. Radziemski, *Handbook of laser-induced breakdown spectroscopy*, (John Wiley & Sons, Ltd, 2006).

[12] James D. Winefordner, Igor B. Gornushkin, Tiffany Correll, Emily Gibb, Benjamin W. Smith and Nicolo Omenrtto, "Comparing several atomic spectrometric methods to the super stars: special emphasis on laser induced breakdown spectrometry, LIBS, a future super star", Anal. At. Spectrom. **19**, 1061-1083 (2004).

[13] C. Chaleard, P. Mauchien, N. Andre, J. Uebbing, J. L. Lacour and C. J. Geertsen, J. L. Lacour and C. Geertsen, "Correction of Matrix Effects in Quantitative Elemental Analysis With Laser Ablation Optical Emission Spectrometry", Anal. At. Spectrom. **12**, 183-188 (1997).

[14] M. Adamson and S. J. Rehse, "Detection of trace aluminum in model biological tissue with laser-induced breakdown spectroscopy", Appl. Opt. **46**, 5844-5852 (2007).

[15] A. Assion, M. Wollenhaupt, L. Haag, F. Mayorov, C. Sarpe-Tudoran, M. Winter, U. Kutschera and T. Baumert, "Femtosecond laser-induced breakdown spectrometry for Ca^{2+} analysis of biological samples with high spatial resolution", Appl. Phys. B **77**, 391-397 (2003).

[16] E. Tognoni, V. Palleschi, M. Corsi and G.Cristoforetti, "Quantitative micro-analysis by laser-induced breakdown spectroscopy: a review of the experimental approaches", Spectrochim. Acta B **57,** 1115-1130 (2002).

[17] Yasuo Iida, “Effects of atmosphere on laser vaporization and excitation processes of solid samples”, Spectrochim. Acta B **45**, 1353-1367 (1990).

[18] Wolfgang Sdorra and Kay Niemax, “Basic investigations for laser microanalysis: Application of different buffer gases for laser-produced sample plumes”, Mikrochim. Acta. **107**, 319-327 (1992).

[19] D. E. Kim, K. J. Yoo, H. K. Park, K. J. Oh and D. W. Kim, “Quantitative analysis of aluminum impurities in zinc alloy by laser-induced breakdown spectroscopy”, Appl. Spectrosc. **51**, 22-29 (1997).

[20] R. Wisburn, I. Schechter, R. Niessner, H. Schroder, and K. Kompa, “Detector for trace elemental analysis of solid environmental samples by laser plasma spectroscopy”, Anal. Chem. **66**, 2964-2975 (1994).

[21] Stephane Morel, Nicolas Leone, Philippe Adam, and Jacques Amouroux, “Detection of bacteria by time-resolved laser-induced breakdown spectroscopy”, Appl. Opt. **42**, 6184-6191 (2003).

[22] Alan C. Samuels, Frank C. DeLucia, Jr., Kevin L. McNesby, and Andrzej W. Miziolek, “Laser-induced breakdown spectroscopy of bacterial spores, molds, pollens, and protein: initial studies of discrimination potential”, Appl. Opt. **42**, 6205-6209 (2003).

[23] Ana R. Boyain-Goitia, David C. S. Beddows, Ben C. Griffths, and Helmut H. Telle, “Single-pollen analysis by laser-induced breakdown spectroscopy and Raman spectroscopy”, Appl. Opt. **42**, 6119-6132 (2003).

[24] P. B. Dixon and D. W. Hahn, “Feasibility of detection and identification of individual bioaerosols using laser-induced breakdown spectroscopy”, Anal. Chem. **77**, 631-638 (2005).

[25] T. Kim, Z. G. Specht, P. S. Vary, C. T. Lin, “Spectral fingerprints of bacterial strains by laser-induced breakdown spectroscopy”, J. Phys. Chem. B **108**, 5477-5482 (2004).

[26] Chase A. Munson, Frank C. De Lucia Jr., Thuvan Piehler, Kevin L. McNesby, Andrezej W. Miziolek, “Investigation of statistics strategies for improving the discriminating power of laser-induced breakdown spectroscopy for chemical and biological warfare agent stimulants”, Spectrochim. Acta B **60**, 1217-1224 (2005).

[27] John D. Hybl, Shane M. Tysk, Shaun R. Berry and Michael P. Jordan, “Laser-induced fluorescence-cued, laser-induced breakdown spectroscopy biological-agent detection”, Appl. Opt. **45**, 8806-8814 (2006).

[28] Matthieu Baudelet, Laurent Guyon, Jin Yu, Jean-Pierre Wolf, “Spectral signature of native CN bonds for bacterium detection and identification using femtosecond laser-induced breakdown spectroscopy”, Applied Physics Letters **88**, 063901 (2006).

[29] Mathieu Baudelet, Tanguy Amodeo and Emeric Frejafon, Patrick Laloi, “Discrimination of microbiological samples using femtosecond laser-induced breakdown spectroscopy”, Applied Physics Letters **89**, 163903 (2006).

[30] Mathieu Baudelet, Tanguy Amodeo and Emeric Frejafon, Patrick Laloi, “Femtosecond time-resolved laser-induced breakdown spectroscopy for detection and identification of bacteria: A comparison to the nanosecond regime”, Journal of Applied Physics **99**, 084701 (2006).

[31] Melles Griot, *The practical application of light* (Barloworld Scientific, 2006).

[32] http://www.andor.com/library

[33] H. C. Liu, X. L. Mao, J. H. Yoo, R. E. Russo, “Early phase laser-induced plasma diagnostic and mass removal during single-pulse laser ablation of silicon”, Spectrochim. Acta B **54**, 1607-1624 (1999).

[35] Pavel Yaroshchyk, Richard J. S. Morrison, Doug Body and Bruce L. Chadwick, “Theoretical modeling of optimal focusing conditions using laser-induced breakdown spectroscopy in liquid jets”, Applied Spectroscopy **58**, 1353-1359 (2004).

[36] Josef B. Simeonsson and Andrzej W. Miziolek, “Time-resolved emission studies of ArF-laser-produced microplasma”, Appl. Opt. **32**, 939 (1993).

[37] J. A. Aguilera and C. Aragon, “Characterization of a laser-induced plasma by spatially resolved spectroscopy of neutral atom and ion emissions. Comparison of local and spatially integrated measurements”, Spectrochim. Acta B B **59,** 1861-1876 (2004).

[38] Steven J. Rehse, Jonathan Diedrich and Sunil Palchaudhuri, “*Escherichia coli* identification and strain discrimination using nanosecond laser-induced breakdown spectroscopy”, Appl. Phys. **90**, 163901 (2007).

[39] Steven J. Rehse, Jonathan Diedrich and Sunil Palchaudhuri, “Identification and discrimination of *Pseudomonas aeruginosa* bacteria grown in blood and bile by laser-induced breakdown spectroscopy”, Spectrochim. Acta B **62**, 1169-1176 (2007).

[40] Vincent Detalle, Mohamed Sabsabi, Louis St-Onge, Andre Hamel and Rene He on, “Influence of Er:YAG and Nd:YAG wavelengths on laser-induced breakdown spectroscopy measurements under air or helium atmosphere”, Appl. Opt. **42**, 5971-5977 (2003).

[41] M. Adamson, A. Padmanabhan, G. J. Godfrey, and S. J. Rehse “Laser-Induced Breakdown Spectroscopy at a Water/Gas Interface: A Study of Bath Gas-Dependent Molecular Species”, accepted for publication, Spectrochim. Acta B, August 2007.

ABSTRACT

IDENTIFICATION AND DISCRIMINATION OF BACTERIA IN A NOBLE GAS ENVIRONMENT USING LASER-INDUCED BREAKDOWN SPECTROSCOPY (LIBS)

by

NARMATHA JEYASINGHAM

December 2007

Advisor: Dr. Steven J Rehse

Major: Physics

Degree: Master of Science

Biological hazards comprise primarily bacteria, viruses and low concentrations of whatever can create large-scale contamination. In the past few years, large efforts have been committed to identify a reliable, fast and standoff detection and identification technique for microbiological samples. Laser-induced breakdown spectroscopy (LIBS) fulfills all the criteria. We used a nanosecond laser-induced breakdown spectroscopy to identify and discriminate between two non-pathogenic strains of the *E. coli* bacteria called Nino C and HF4714 in the noble gas environment (helium and argon) as they were demonstrated to produce the higher emission intensity, compared to air, for the chosen monitored element under fixed experimental conditions. A discriminant function analysis (DFA) was used to analyze the LIBS spectra from bacteria colonies grown on TSA plates. Also we investigated the ability of discrimination when the argon and helium results are combined. In addition, the reproducibility of the experiment was studied.

Autobiographical statement

I am originally from Colombo, Sri Lanka. I graduated Methodist College, Colombo, Sri Lanka in 2000. I received my bachelor's degree in physics, with university honors from University of Peradeniya (UOP). While earning my bachelor’s, I tutored physics and mathematics for I am currently in the masters program in physics art the Department of Physics and Astronomy here at Wayne State University (WSU). I have been attending here since fall, 2006. I plan on concentrating in medical physics after completing my degree of Master of Science. During the fall term of 2006 and winter term of 2007, I was a graduate teaching assistant (GTA) for PHY 2131 (undergraduate physics lab). During the spring/summer and fall semester of 2007, I was working as research assistant with Dr Steven J. Rehse.